Energy, Material, and Telecommunication Center

# ENGINEERED NANOSTRUCTURED MATERIALS FOR SOLAR ENERGY CONVERSION APPLICATIONS

# MATÉRIAUX NANOSTRUCTURÉS CONÇUS POUR LES APPLICATIONS DE L'ÉNERGIE SOLAIRE

By

Omar Mohamed Yousri Elsayed Abdelkarim

Thesis presented for obtaining the degree of
Doctor of Philosophy, Ph.D.
Doctorate in Energy and Material Sciences

**Jury members**

| | |
|---|---|
| President of the jury and Internal Examiner | Prof. Sharif Sadaf<br>INRS-EMT |
| External Examiner | Prof. Nhat Truong Nguyen<br>Concordia University |
| External Examiner | Prof. Jérôme Claverie<br>Sherbrooke University |
| Research Director | Prof. Federico Rosei<br>INRS-EMT |
| Research Co-director | Prof. Aychan Yurtsever<br>INRS-EMT |

# ACKNOWLEDGMENTS

First and foremost, I would like to thank God and my family for their support to finish this study. I also would like to thank my supervisors, Prof. Federico Rosei and Prof. Aycan Yurtsever, for continual guidance and assistance throughout every stage of my Ph.D. study. Their enthusiasm and effort make my research work meaningful and made me grow in the scientific field. Their invaluable inspiration and professional advice make me find the right direction both in my academic and daily life. The experience under their supervision is one of the most important achievements in my life. Their professional attitude has greatly motivated me to explore my future career.

Furthermore, I would like to extend my gratitude to my group leader Dr. Gurpreet Singh Selopal for his kindly help in motivating me. He provides me with lots of invaluable suggestions, which helped me reach my research goals. He always initiates important discussions that help solve problems both in the experiment and theoretical parts.

I also extend my gratitude to all the group members from the Nano-Femto lab and other collaborators for their kind support and help throughout my Ph.D. work. I feel lucky to be part of such a hardworking, supportive, and inspiring group of graduate students and postdoctoral fellows. In addition, I would like to thank our collaborators Dr. Hadis Zarrin, Dr. Jasneet Kaur, Dr. Kulbir K. Ghuman, Dr. Fabiola Navarro-Pardo, Dr. Amir Mirzaei, Dr. Mohamed Chaker, and Dr. Ghada bassioni in their contribution in my thesis.

I would like to thank all staff and technicians in the INRS-EMT center, especially Mr. Christophe Chabanier, Mr. Patrick Soucy, and Dr. Catalin Harnagea, for helping to address problems I had when I worked on X-ray diffraction, X-ray photoelectron spectroscopy, scanning electron microscopy, and atomic force microscopy.

Finally, I wish to acknowledge the UNESCO Chair in Materials and Technologies for Energy Conversion, Saving and Storage (MATECSS) for the Ph. D. excellence scholarships and the Collaborative Research and Training Experience in Sustainable Electronics and Eco-Design (CREATE SEED) program for the financial support.

# ABSTRACT

Solar-driven Photoelectrochemical (PEC) water splitting is considered a promising approach to produce hydrogen from water. Hydrogen is a substantial clean energy source, and its combustion in the fuel cell only yields water vapor as a by-product. During the operation of the PEC device, two simultaneous processes occur; (i) the generation and collection of the photogenerated charge carriers that involve in the oxidation/reduction reaction of water; (ii) the undesirable non-radiative carrier recombination that opposes the reaction kinetics. Thus, different strategies were implemented to enhance the performance of the PEC devices by improving the carrier generation/collection and reducing the non-radiative carrier recombination.

First, two-dimensional functionalized hexagonal boron nitride (2D F-h-BN) was introduced at the interface between the photoanode and quantum dots (QDs) to passivate the photoanode surface and acts as an energy barrier to reduce the carrier recombination. The results show that the device with F-h-BN exhibits a 60% improvement in the photocurrent density as compared to the control device. In addition, muti-wall carbon nanotubes (MWCNT) were integrated into the electron transport layer (ETL) to enhance the charge transport properties. The highest achieved photocurrent density was 6.35 mA $cm^{-2}$ at 1.0 V vs. RHE.

Then, a hybrid structure of $TiO_2$ nanorods (NRs) and nanoparticles (NPs) was fabricated. The optimization process was conducted on the NRs by adjusting the hydrothermal growth time. While the NPs were optimized by varying the particle size. The final photoanode structure yields a 172% improvement in the photocurrent density as compared to the control device. Moreover, the surface of the hybrid photoanode was engineered with hydrazine treatment to minimize the influence of trap sites that reduce the PEC performance. This led to a further improvement of 28% in the photocurrent density to reach 5.43 mA $cm^{-2}$ with CdS QDs, and 8.12 mA $cm^{-2}$ with CdS/CdSe QDs at 0.8 V vs RHE.

Finally, self-organized $TiO_2$ nanotubes (NTs) were sensitized with QDs and then treated with a Cu-based solution to create a p-n heterojunction. The fabrication of the $TiO_2$ NTs was done through the anodization process, using a metallic titanium substrate. After the QDs deposition, the photoanode was immersed for a few seconds in the Cu-based solution to form CuSe. The p-n heterojunction shows a 13% improvement in the photogenerated current density, reaching 4.7 mA.$cm^{-2}$ at 0.5 V vs RHE.

This work provides different strategies applied to enhance the performance of PEC devices for hydrogen generation. The incorporation of certain materials and the use of specific procedures were emphasized for their influence on the optical and electronic properties of the photoanode.

**Keywords**: Photoelectrochemical cell, Water splitting, Two-dimensional materials, Functionalized hexagonal boron nitride, Quantum dots; Carrier recombination, Hydrazine treatment, p-n heterojunctions, Carrier dynamics.

# MATÉRIAUX NANOSTRUCTURÉS CONÇUS POUR LES APPLICATIONS DE L'ÉNERGIE SOLAIRE

## RÉSUMÉ

La fractionnement photoélectrochimique (PEC) de l'eau par l'énergie solaire est considérée comme une approche prometteuse pour produire de l'hydrogène à partir de l'eau. L'hydrogène est une source d'énergie propre importante et sa combustion dans la pile à combustible ne produit que de la vapeur d'eau comme sous-produit. Pendant le fonctionnement du dispositif PEC, deux processus simultanés se produisent; (i) la génération et la collecte des porteurs de charge photogénérés qui interviennent dans la réaction d'oxydation/réduction de l'eau ; (ii) la recombinaison indésirable des porteurs non radiatifs qui s'oppose à la cinétique de la réaction. Ainsi, différentes stratégies ont été mises en œuvre pour améliorer les performances des dispositifs PEC en améliorant la génération/collecte des porteurs et en réduisant la recombinaison des porteurs non radiatifs.

Tout d'abord, du nitrure de bore hexagonal fonctionnalisé bidimensionnel (2D F-h-BN) a été introduit à l'interface entre la photoanode et les quantum dots (QDs) pour passiver la surface de la photoanode, qui agit comme une barrière énergétique pour réduire la recombinaison des porteurs. Les résultats montrent que le dispositif avec F-h-BN présente une amélioration de 60 % de la densité de photocourant par rapport au dispositif de contrôle. De plus, des nanotubes de carbone multiparois (MWCNT) ont été intégrés dans la couche de transport d'électrons (ETL) pour améliorer les propriétés de transport de charge. La densité de photocourant la plus élevée obtenue est 6,35 mA cm$^{-2}$ à 1,0 V vs RHE.

Ensuite, une structure hybride de nanotiges (NRs) et de nanoparticules (NPs) de $TiO_2$ ont été fabriquées. Le processus d'optimisation a été mené sur les NRs en ajustant le temps de croissance hydrothermale. Tandis que les NPs ont été optimisées en faisant varier la taille des particules. La structure de la photoanode finale donne une amélioration de 172 % de la densité de photocourant par rapport au dispositif de contrôle. De plus, la surface de la photoanode hybride a été conçue avec un traitement à l'hydrazine pour minimiser l'influence des sites de pièges qui réduisent les performances du PEC. Cela a conduit à une nouvelle amélioration de 28 % de la densité de photocourant pour atteindre 5,43 mA cm$^{-2}$ avec les QDs CdS et 8,12 mA cm$^{-2}$ avec les QDs CdS/CdSe à 0,8 V vs RHE.

Enfin, des nanotubes de $TiO_2$ (NT) auto-organisés ont été sensibilisés avec des QDs puis traités avec une solution à base de Cu pour créer une hétérojonction p-n. La fabrication des NT de $TiO_2$ a été réalisée par le processus d'anodisation, en utilisant un substrat de titane métallique. Après le dépôt des QDs, la photoanode a été immergée pendant quelques secondes dans la solution à base de Cu pour former CuSe. L'hétérojonction p-n montre une amélioration de 13% de la densité de courant photogénérée, atteignant 4,7 mA.cm$^{-2}$ à 0,5 V vs RHE.

Ce travail propose différentes stratégies appliquées pour améliorer les performances des dispositifs PEC pour la génération d'hydrogène. L'incorporation de matériaux particuliers et l'utilisation de procédures spécifiques ont été soulignées pour leur influence sur les propriétés optiques et électroniques de la photoanode.

**Mots-clés** : Cellule photoélectrochimique, Fractionnement de l'eau, Matériaux bidimensionnels, Nitrure de bore hexagonal fonctionnalisé, quantum dots, recombinaison des porteurs, traitement à l'hydrazine, hétérojonctions p-n, dynamique des porteurs.

# SYNOPSIS

## Introduction

L’existence des civilisations humaines dépend principalement de la transformation énergétique. Tout au long de l’histoire, la quête principale a été de trouver une source d’énergie plus concentrée et plus abondante pouvant être convertie, de façon abordable et à haut rendement, en chaleur, en lumière et en mouvement. De plus, l’utilisation efficace de l’énergie peut donner lieu à une plus grande récolte de nourriture, produire divers biens, permettre une plus grande mobilité et créer un accès virtuellement illimité à une quantité remarquable d’informations. En conséquence, la conversion de l’énergie, d’une forme à une autre, est le moteur de toute activité économique [1].

La conservation de l’énergie est un fait important qui doit être discuté. La première loi de la thermodynamique définit la notion de conservation de l’énergie. Néanmoins, tout au long des chaînes de conversion, l’énergie utile disponible pour effectuer le travail diminue progressivement. Cette réalité inévitable est définie par la seconde loi de la thermodynamique. Concrètement, dans un système isolé, sans aucune source d’énergie extérieure, l’entropie tend à se maximiser. Cela signifie que l’énergie utile disponible pour la conversion tend à diminuer. L’efficacité de conversion d’énergie est définie comme le rapport de la production souhaitable à l’entrée initiale. Dans un processus à faible rendement de conversion, la perte d’énergie est considérablement élevée. Ainsi, une fraction de l’énergie d’origine a été transformée en un produit ou service utile. La quantité totale d’énergie n’est pas perdue (première loi de la thermodynamique). Cependant, la majeure partie de l’énergie est dispersée sous forme de chaleur (seconde loi de la thermodynamique) [2].

## Consommation d’énergie

La source principale de transformation de l’énergie est l’énergie solaire. Le monde moderne a utilisé cette énergie renouvelable de deux méthodes vitales: a) La consommation de réserves de combustibles fossiles (pétrole brut et gaz naturel), b) la production d’électricité par la combustion de combustibles fossiles [3].

L’origine des combustibles fossiles provient de la biomasse accumulée. Le processus de transformation se produit sous pression et chaleur, sur des centaines de millions d’années. L’origine des combustibles fossiles est affectée par leur forte teneur en carbone et leur faible teneur en eau. Ce mélange se traduit par une source à haute densité d’énergie [4]. De plus, ils nous ont donné accès à des sources d'énergie hautement concentrées et faciles à stocker. L'utilisation efficace de cette énergie a remodelé tous les secteurs de notre économie. À leur tour, d'autres avancées ont modifié la structure et la dynamique des sociétés existantes. Par conséquent, il y a une augmentation de l'espérance de vie moyenne, une urbanisation croissante, une mobilité personnelle accrue et la transformation du commerce international à une échelle de masse [1]. Ces activités entraînent une augmentation exponentielle de la consommation énergétique mondiale moyenne, comme le montre la figure 1 [5].

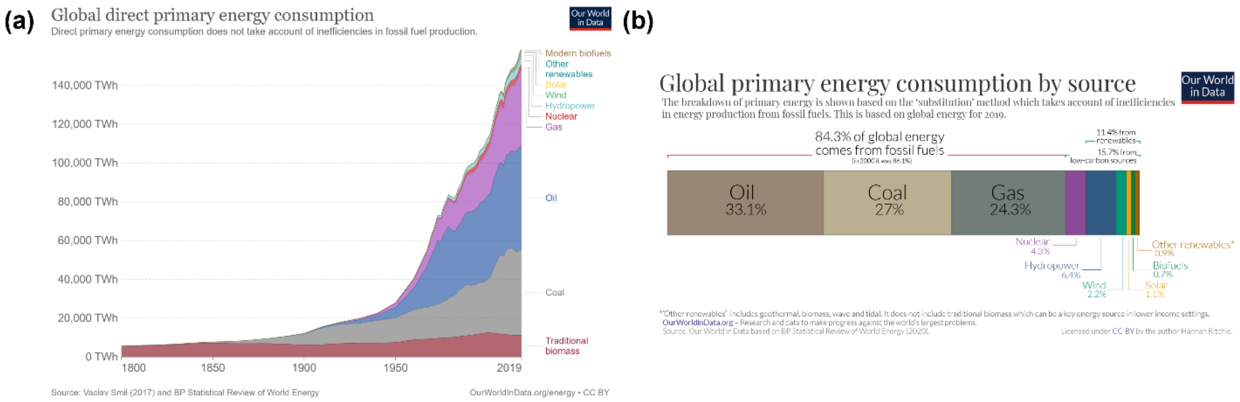

**Figure 1 (a) Consommation énergétique mondiale (b) Source du graphique de la consommation énergétique mondiale [6]**

Les futurs besoins énergétiques mondiaux sont différents d'une nation à l'autre. Cela peut être réalisé par les différences de consommation d'énergie existantes entre eux. Le développement de chaque pays peut se refléter dans la consommation moyenne d'énergie par habitant. Seul un cinquième des pays du monde ont atteint l'ajustement vers des sociétés développées affluentes. La consommation d'énergie par habitant de ces pays est supérieure à 120 GJ/habitant. [7]. Croissance économique et consommation d'énergie vont de pair pour assurer une meilleure qualité de vie. Ce concept inclut la satisfaction des besoins physiques de base (santé et nutrition) et le développement de l'intellect humain (allant de l'éducation de base aux libertés individuelles). L'Indice de développement humain (IDH), créé par le Programme des Nations Unies pour le développement (PNUD), est un indicateur fiable pour comparer différents pays [Figure 2] [8]. L'IDH combine l'espérance de vie à la naissance, la capacité de lecture des adultes, la scolarisation combinée et le produit intérieur brut (PIB) par habitant.

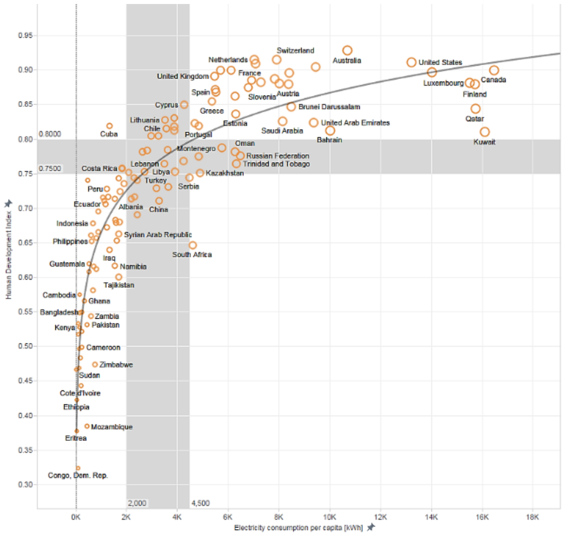

**Figure 2 IDH par rapport à la consommation d'électricité par habitant [9]**

D'après la figure de l'IDH, la consommation d'énergie est donc associée à une meilleure qualité de vie de façon linéaire uniquement pendant les premiers stades de développement. Pourtant, il n'y a pas d'amélioration évidente de la qualité de vie fondamentale au-dessus du niveau de 0,8-0,9 IDH. D'après la figure 2, il existe une immense différence dans la consommation d'énergie annuelle par habitant entre les différents pays. À titre d'exemple, la consommation aux États-Unis (É.-U.) et au Canada est environ plus de trente fois supérieure à celle des pays les plus pauvres d'Afrique subsaharienne [10]. Malgré des décennies de programmes d'électrification, 940 millions de personnes dans le monde n'ont toujours pas accès à l'électricité [11]. Ceci est particulièrement visible sur les images satellites nocturnes [12]. Il existe une différence de contraste frappante entre les pays riches et les vastes zones d'obscurité sur de grandes parties de l'Asie, de l'Afrique et de l'Amérique latine. En conséquence, les pays en développement ont encore besoin d'une augmentation absolue de la consommation d'énergie pour atteindre une meilleure qualité de vie. Néanmoins, le découplage entre la croissance économique et la consommation d'énergie au début de l'économie moderne est inévitable.

## Problèmes liés aux combustibles fossiles

Comme discuté précédemment, la civilisation moderne s'est établie sur la consommation massive et croissante de combustibles fossiles. Cette pratique est limitée par son abondance, ainsi que par les conséquences environnementales de la combustion du charbon et des hydrocarbures. La nature finie des combustibles fossiles en fait des ressources non durables sur lesquelles compter pour la future demande énergétique [13]. Cependant, le défi le plus critique de la consommation substantielle de combustibles fossiles est les problèmes environnementaux généralisés [14]. Le changement climatique rapide découle de l'extraction et de la combustion de combustibles fossiles. La situation s'aggrave avec la contribution de la production industrielle, de l'urbanisation rapide, de la mondialisation économique, de la déforestation et des mauvaises pratiques de culture et d'élevage [15]. L'effet cumulatif de ces activités a déjà atteint au-delà des problèmes locaux et régionaux des effets déstabilisateurs sur le changement climatique mondial. La conséquence la plus indésirable est le réchauffement climatique [16]. L'utilisation de combustibles fossiles et l'électricité générée par leur combustion constituent la pollution de l'atmosphère et les émissions de gaz à effet de serre le plus important d'origine humaine [17]. La combustion des combustibles fossiles implique une oxydation rapide de leur carbone, qui produit des quantités croissantes d'émissions de dioxyde de carbone (CO2). Parallèlement, du méthane (CH4), un gaz à effet de serre plus puissant, est libéré lors de la production et du transport du gaz naturel par les gazoducs. Pendant une longue période, les concentrations atmosphériques de $CO_2$ ont fluctué dans une fourchette de 250 parties' par million (ppm). Maintenant, le niveau de $CO_2$ de la planète montre une augmentation constante. La concentration dépasse 400 ppm pour la première fois, soit 40 % de plus que l'ère précédant les combustibles fossiles. Il devrait gagner encore 40 % d'ici la fin du siècle [Figure 3] [18]. L'effet de ce changement sur le réchauffement climatique reste très incertain. Pourtant, le panel intergouvernemental a proposé différents scénarios pour le changement climatique. Ils prédisent une augmentation moyenne de la température mondiale entre +2$^o$C et +4$^o$C d'ici 2100. Une situation très inquiétante, surtout lorsque la fourchette haute de ce scénario atteint +6$^o$C [19]. L'entente de Paris conseille que pour contrôler les conséquences désagréables du réchauffement climatique, la température moyenne ne doive pas augmenter de plus de 2$^o$C. Cela nécessiterait une substitution directe de la combustion des combustibles fossiles et une transition rapide vers des sources d'énergie renouvelable [20].

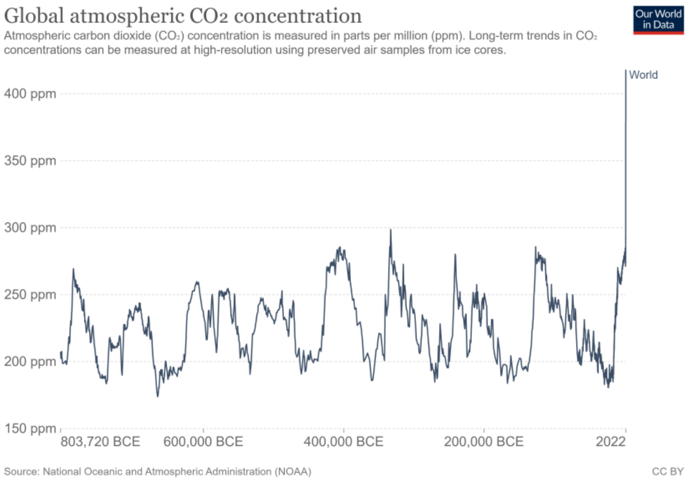

**Figure 3 Tendance de la concentration de $CO_2$ [21]**

## Énergie renouvelable

L'évolution des sources d'énergie renouvelables est cruciale pour un avenir durable. Les énergies renouvelables sont la source issue des ressources naturelles de la terre. Ces énergies ne sont ni finies ni épuisables et se présentent sous diverses formes, notamment l'hydroélectricité, l'éolien, le solaire, la biomasse et la géothermie [22].

L'énergie solaire est considérée comme la source d'énergie la plus propre. Les réactions thermonucléaires au cœur du soleil convertissent environ 4 mégatonnes (Mt) de matière en énergie chaque seconde. Selon le calcul masse-énergie d'Einstein, le soleil génère près de $3{,}8\text{x}10^{26}$ W d'énergie [23]. Nous bénéficions de 1367 $W.m^{-2}$ (constante solaire) de cette énergie lorsqu'elle atteint l'atmosphère terrestre [24]. L'atmosphère filtre plus de 70 % du rayonnement solaire; absorption ultraviolette (UV) par l'ozone et l'$O_2$, et absorption infrarouge (IR) par $H_2O$, $N_2O$, $CH_4$, poussière et $CO_2$. L'ensoleillement au repos de l'énergie solaire mondiale atteint un apport énergétique moyen de $1{,}3 \times 10^5$ TW, soit quatre ordres de grandeur de plus que la consommation énergétique mondiale totale [25]. L'utilisation d'une petite fraction de l'énergie solaire pourrait dynamiser les civilisations futures consommant plus d'énergie que la nôtre. Les technologies prometteuses d'énergie solaire propre présentent de nombreux avantages à long terme, tels que l'augmentation de la sécurité énergétique des pays, la réduction de la pollution et la promotion de la durabilité. Cependant, convertir ce flux abondant d'énergie solaire en une forme d'énergie abordable est un énorme défi [26].

Les technologies de conversion de l'énergie solaire ont reçu une attention considérable au cours de la dernière période [27]. L'expansion rapide est une caractéristique commune des premiers stades de développement. Le photovoltaïque (PV) est la technologie utilisée pour convertir l'énergie solaire en électricité. De nos jours, le PV est considéré comme un contributeur beaucoup plus faible par rapport aux autres technologies d'énergie renouvelable. Pourtant, les installations de nouveaux modules PV ont été le segment énergétique à la croissance la plus rapide ces derniers temps [28]. Trois raisons fondamentales qui font du PV l'une des technologies d'énergie renouvelable les plus attrayantes : (1) la disponibilité des ressources utilisées pour la production (2) sa haute densité de puissance, et (3) les avantages caractéristiques de la technique de conversion (pas de déplacement pièce détachée, fonctionnement silencieux et assemblage facile des unités) [29]. D'autre part, les inconvénients majeurs sont un rendement de conversion relativement faible et des facteurs de faible capacité dans les régions moins ensoleillées. De plus, leur intermittence inhérente pose des problèmes non triviaux pour les intégrer dans les grilles existantes [30]. C'est pourquoi la contribution de l'énergie solaire à la production d'électricité reste insignifiante à l'échelle mondiale.

La disponibilité de nouveaux moyens peu coûteux de stocker l'électricité solaire à grande échelle peut être une solution potentielle. Les capacités des grandes batteries de stockage ont augmenté de plusieurs dizaines de mégawatts (MW). Ce qui est nécessaire, en particulier pour les mégalopoles croissantes du monde, est stocké à l'échelle du gigawatt (GW). Une autre option pratique consiste à convertir l'énergie solaire en combustible chimique (combustible solaire) [31]. Les combustibles solaires utilisent des ressources abondantes (c'est-à-dire l'eau, le dioxyde de carbone ou l'azote) pour générer des produits chimiques riches en énergie (c'est-à-dire l'hydrogène, les hydrocarbures et l'ammoniac). Ce type de carburant peut être produit et stocké pour une utilisation ultérieure. Différentes technologies ont été développées pour effectuer ces réactions de manière durable [32].

### L'hydrogène comme carburant

L'hydrogène ($H_2$) peut être une importante source d'énergie propre. Contrairement au méthane, il n'est pas présent dans les réservoirs de la croûte terrestre et il est donc produit soit à partir de méthane, soit à partir d'eau. $H_2$ a plusieurs propriétés prometteuses qui en font une excellente source d'énergie. Par exemple, sa densité énergétique dépasse les sources d'énergie disponibles dans le commerce [Tableau 1], et sa combustion ne produit que de l'eau comme sous-produit. Le H2 est un carburant synthétique idéal, non toxique, léger, stockable et transportable [33].

**Tableau 1 Valeur de densité énergétique pour différents combustibles [34]**

| Fuel | Combustible Densité énergétique (MJ. Kg-1) |
|---|---|
| Hydrogène | 142 |
| Méthane | 55.5 |
| Essence | 47.5 |
| Gazole | 44.8 |

Trois technologies différentes peuvent être utilisées pour générer du $H_2$ à partir de l'eau en utilisant l'énergie solaire, comme le montre la figure 4. (a) Photocatalyse (PC); où des suspensions ou poudres de particules photo-actives sont dispersées dans le milieu et facilitent à la fois les réactions d'oxydation et de réduction (b) fractionnement photoélectrochimique (PEC) de l'eau; dans lequel une ou plusieurs électrodes photo-actives (anode et cathode) font des réactions d'oxydation et de réduction dans une cellule électrochimique (c) électrolyse PV (PV-EC) ; une puissance indépendante est générée par l'unité de cellule PV, qui est isolée de la cellule électrochimique et connectée à des électrodes non photoactives (anode et cathode) qui facilitent la fractionnement de l'eau [35].

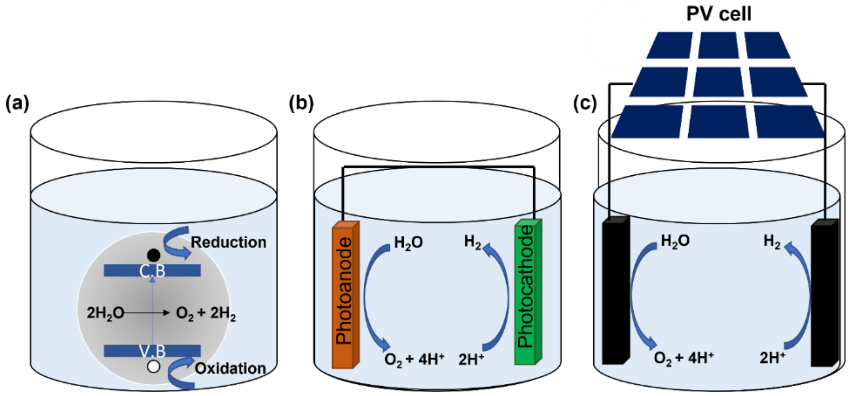

**Figure 4 Différents systèmes de fractionnement de l'eau alimentés par l'énergie solaire (a) Photocatalyser (b) Photoélectrochimique (c) Électrolyse PV**

Du point de vue de l'efficacité de conversion, l'efficacité la plus élevée du solaire à l'hydrogène (STH) est pour le système PV-EC, suivi du système PEC, et l'efficacité la plus faible est pour le système PC. Cependant, les panneaux photovoltaïques sont complexes et associés à un coût d'investissement élevé, une grande intensité de matériaux dans la production, et leur empreinte carbone de fabrication est supérieure à celle du PEC ou du PC. Ainsi, le système PEC est considéré comme une option alternative viable avec un coût inférieur, une durée de vie moyenne et une efficacité modérée avec une amélioration potentielle [36]. Les trois principaux paramètres de la production pratique de $H_2$ à l'aide de l'énergie solaire sont le coût, l'efficacité et la durée de vie. Une comparaison entre différents systèmes de fractionnement de l'eau et ces paramètres est présentée à la figure 5.

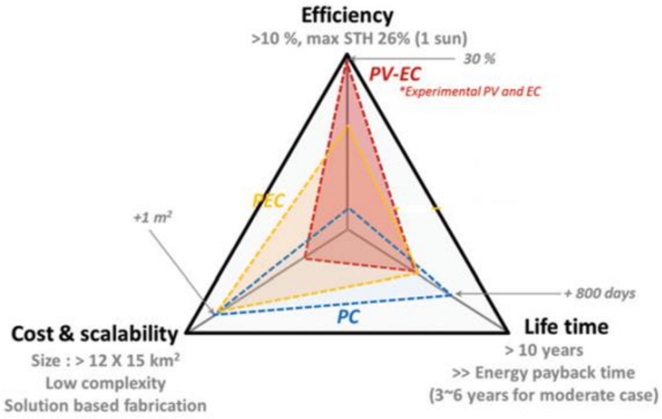

**Figure 5 Comparaisons entre PV-EC, PEC et PC pour des systèmes pratiques de production d'hydrogène solaire [36]**

## Principe de fonctionnement du PEC

Dans une procédure typique, le dispositif PEC est basé sur des matériaux semi-conducteurs utilisés comme photoanode et/ou photocathode. Lorsque les électrodes sont immergées dans une solution d'électrolyte et éclairées par la lumière du soleil, l'énergie des photons est convertie en énergie électrochimique, qui divise l'eau en hydrogène et en oxygène [37]. Le processus de fractionnement de l'eau est considéré comme une réaction ascendante, car il nécessite un changement d'énergie libre standard de 237 kJ mol$^{-1}$, ce qui équivaut à 1,23 eV par électron [38]. Pendant l'illumination, la photoanode semi-conductrice génère une paire électron/trou par excitation de bande interdite. Les porteurs photoexcités sont séparés à l'interface photoanode/électrolyte et transférés à la surface, puis consommés par les réactions redox de surface. La recombinaison des porteurs de charge a lieu parallèlement aux réactions ultérieures. Par conséquent, le processus de fractionnement de charge dans la photoanode et les réactions redox qui se produisent à la surface doivent se produire pendant la durée de vie des porteurs photoexcités pour obtenir un fractionnement réussi de l'eau. Les réactions d'oxydoréduction ne peuvent exister que si les porteurs photo-générés sont thermodynamiquement favorables [39].

Pour une photoanode semi-conductrice de type n, une fois immergés dans la solution d'électrolyte, les électrons sont consommés à partir de la surface semi-conductrice jusqu'à ce que l'équilibre soit atteint. Ce processus se produit lorsque le niveau de Fermi est positionné plus négativement que le potentiel redox de la solution d'électrolyte. Le transfert de charge se traduit par un champ électrique interfacial, où le potentiel électrostatique compense la différence initiale du niveau de Fermi. Il en résulte une couche d'appauvrissement entre la solution d'électrolyte et le semi-conducteur. À la suite de la condition d'équilibre, le niveau de Fermi du semi-conducteur est égal au potentiel redox de l'électrolyte. Sachant que la densité d'électrons à l'interface d'un semi-conducteur est finie et que les positions des bandes électroniques sont supposées fixes, le transfert d'électrons crée une courbure de bande [Figure 6] [40].

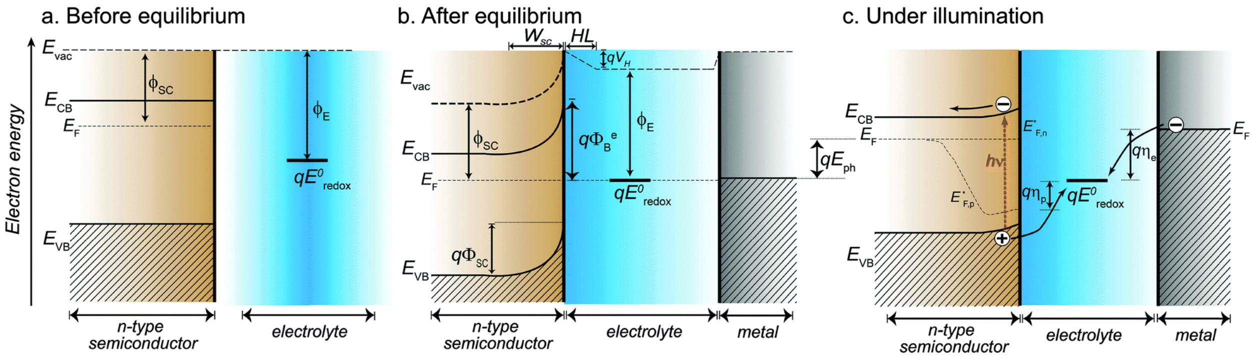

**Figure 6 La modification de surface se produit à l'interface semi-conducteur/électrolyte dans le PEC [41]**

Les réactions d'oxydation/réduction de l'eau, résultant du fractionnement de l'eau par les photons, sont décrites avec les équations suivantes :

- Absorption lumineuse : SC + hv → $e^-_{C.B.}$ + $h^+_{V.B.}$
- Oxydation de l'eau (OER) : $2H_2O + 4\ h^+_{V.B.} \rightarrow O_2 + 4H^+$
- Réduction de protons (HER) : $2H^+ + 2\ e^-_{C.B.} \rightarrow H_2$
- Décomposition globale de l'eau : $2H_2O \rightarrow 2H_2 + O_2$

**Quand SC est un matériau semi-conducteur, h s la constante de Planck - 6,62607015 × 10−34 $m^2kgs^{-1}$**

**v est la fréquence du photon, $e^-_{C.B}$ est les électrons dans la bande de conduction (C.B.)**

**$h^+_{V.B.}$ est les trous dans la bande de valence (V.B.)**

**OER est la réaction d'évolution de l'oxygène**

**HER est la réaction de dégagement d'hydrogène.**

De plus, pour obtenir un bon fractionnement de l'eau, divers critères clés doivent être atteints par les matériaux semi-conducteurs [42].

- Le semi-conducteur doit générer la tension nécessaire lors de l'irradiation pour séparer l'eau (> 1,23 eV).
- La bande interdite en vrac doit absorber une partie considérable du spectre solaire
- Les potentiels de bord de bande au niveau des surfaces doivent se situer dans la plage des potentiels redox d'hydrogène et d'oxygène (+0 V et +1,23 V par rapport à l'électrode à hydrogène normale, respectivement), où le V.B. la position doit être plus positive et la position C.B. plus négative que le potentiel redox.
- Le dispositif PEC doit présenter une stabilité à long terme contre la corrosion dans les électrolytes aqueux.
- Minimiser les pertes d'énergie du transfert de charge, dues à la surtension cinétique, à l'interface semi-conducteur/électrolyte, qui peuvent atteindre une plage de 1,6-2,4 eV.

Le fractionnement et le transport des porteurs de charge sont différents dans le cas des nanoparticules (NP). L'effet de la courbure de la bande pourrait être moins prononcé, où la largeur de la couche de charge d'espace (c'est-à-dire la couche d'appauvrissement) pourrait être plus grande que la taille des particules. En revanche, le champ électrique induit formé par la couche de charge d'espace est crucial, car il joue un rôle vital dans le processus de fractionnement des porteurs de charge. Le champ électrique favorise la dérive d'un porteur de charge donné (par exemple, les électrons) vers la surface et évite la présence de l'autre porteur (par exemple, les trous) sur cette même surface [43]. Dans le cas de la photoanode, les trous photoexcités s'accumulent sur la surface et sont consommés dans les réactions d'oxydation, tandis que les électrons sont transférés au contact arrière du substrat qui est connecté à la contre-électrode via un circuit externe où se produisent les réactions de réduction [Figure 7] [44].

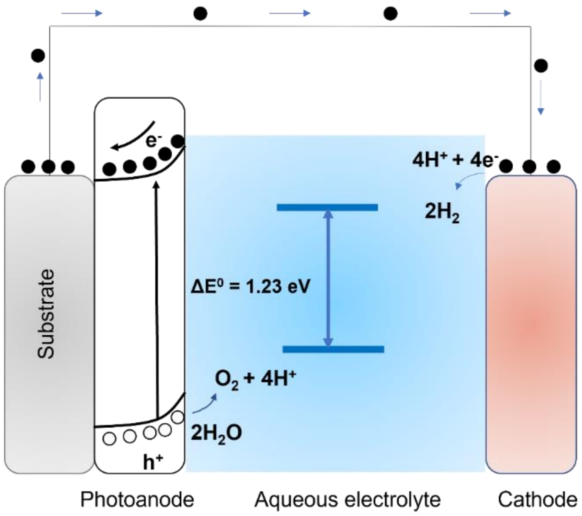

**Figure 7 Illustration d'un dispositif de fractionnement de l'eau à photoanode de type n.**

Les opérations fondamentales dans le principe des dispositifs PEC dépendent (a) de l'efficacité de collecte de la lumière (LHE), qui est associée au coefficient d'absorption des matériaux photoactifs. De plus, la probabilité de génération de porteurs de charge dépend de la bande interdite des matériaux photoactifs ; (b) l'efficacité de transfert de charge photo-injectée dans la couche de transport d'électrons (ETL), qui est affectée par la longueur de diffusion et la mobilité des porteurs de charge ; et (c) l'efficacité de transport de charge interfaciale à l'interface semi-conducteur/électrolyte, où le potentiel de charge de surface affecte la dynamique des porteurs et le processus de fractionnement du porteur de charge photogénéré [36] [44].

La sensibilisation des semi-conducteurs à large bande interdite avec des quantum dots (QDs) est une nouvelle approche pour améliorer l'efficacité du système de fractionnement de l'eau PEC pour la génération de $H_2$. Les QDs sont des semi-conducteurs de taille nanométrique avec une bande interdite étroite, adaptée pour absorber la lumière dans les régions visible et infrarouge. Ils sont facilement produits avec le procédé à faible coût. Les QDs présentent des propriétés électroniques uniques, telles que la possibilité de plusieurs porteurs de charge chaude de génération et d'extraction d'excitation avant la thermalisation, et une bande interdite réglable en fonction de sa taille. Ces propriétés étaient particulièrement intéressantes pour améliorer les performances des PEC et d'autres dispositifs optoélectroniques.

De même, dans les cellules solaires sensibilisées QDs (QDSC), le semi-conducteur à large bande interdite est sensibilisé avec un semi-conducteur à bande interdite étroite (i.e., QDs) pour récolter la lumière du soleil et générer des porteurs de charge (génération de charge). Ces porteurs de charge se sont séparés du semi-conducteur à large bande interdite, avec un alignement de bandes approprié (injection/fractionnement de charge). Ensuite, les porteurs de charge sont transportés (transport de charge) à travers le semi-conducteur jusqu'au contact arrière de la photoanode (collecte de charge), tandis que les trous sont transférés à l'interface semi-conducteur/électrolyte pour la réaction redox catalytique.

### Problème de recherche

Le principal problème est que les performances globales du système de fractionnement de l'eau PEC basé sur les QDs sont encore faibles, en raison de la recombinaison indésirable des porteurs dans (i) l'anode mésoporeuse semi-conductrice à large bande interdite (par exemple, $TiO_2$) et (ii) à l'interface $TiO_2$/QDs/électrolyte. [22]. Ces processus de recombinaison sont les facteurs les plus importants pour limiter les performances des dispositifs PEC. Il existe différents types de processus de recombinaison qui peuvent se produire à l'intérieur du semi-conducteur à large bande interdite.

Premièrement, il existe différents types de processus de recombinaison qui peuvent se produire à l'intérieur du semi-conducteur à large bande interdite :

a) Recombinaison radiative [Figure 8 (a)] : recombinaison spontanée d'une paire électron-trou de manière directe. Les porteurs de charge dans la C.B. sont recombinés avec le trou dans le V.B., et l'excès d'énergie est émis sous la forme d'un photon.
b) Recombinaison Auger [Figure 8 (b)] : ce processus est important dans un semi-conducteur à bande interdite indirecte. Dans ce processus, l'énergie et la quantité de mouvement sont transférées d'un électron à un autre. Cela dépend principalement de la densité de porteurs libres. Lorsque la densité de porteurs augmente, le processus de recombinaison augmente.
c) Recombinaison assistée par piège [Figure 8 (c)] : Il ne s'agit pas d'une recombinaison directe, mais plutôt à travers des impuretés et des défauts de réseau. Ils sont situés dans l' « état de piège » de l'intervalle interdit. Il s'agit d'un processus de recombinaison dominant dans le semi-conducteur dans la plupart des conditions de fonctionnement.

- Les pièges en masse sont la distribution de densité des états des pièges en masse dans la bande interdite du semi-conducteur nanostructure. Il limite le mouvement des électrons et des trous. Un piège consiste soit en une impureté chimique, soit en une imperfection dans l'espacement régulier des atomes. L'énergie de ces états de défaut va profondément jusqu'au niveau de Fermi. Ces défauts agissent comme des pièges et affectent les propriétés électriques des semi-conducteurs. Les porteurs de charge sont piégés n'importe où dans un système jusqu'à ce qu'il se recombine et ne participe plus au transport de charge.

d) Recombinaison de surface [Figure 8 (d)] : C'est un état piège trouvé à la surface des matériaux provenant de surfaces non construites.

- Les états de surface sont formés en raison de la transition nette d'un matériau solide qui se termine par une surface et se trouve uniquement au niveau des couches d'atomes les plus proches de la surface (liaisons pendantes à la surface). La terminaison matérielle conduit à un changement de la structure de la bande électronique du matériau en vrac au vide. Formation de nouveaux états électroniques, dits états de surface.

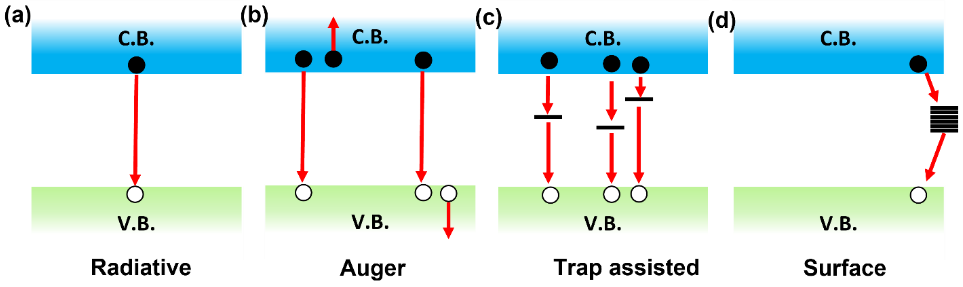

**Figure 8 Voies de recombinaison dans les semi-conducteurs (a) radiation directe (b) Auger (C) assistée par piège (d) recombinaison de surface**

Deuxièmement, les processus de recombinaison se produisent dans les dispositifs PEC TiO2/QD/électrolyte [Figure 9]

1) À l'intérieur du QDs (états de défaut).
2) Électron excité dans le QDs avec des espèces oxydées de l'électrolyte.
3) Rétro transfert d'électrons de la C.B. de $TiO_2$ vers V.B. de QDs.
4) Recombinaison d'électrons dans TiO2 avec des espèces oxydantes de l'électrolyte

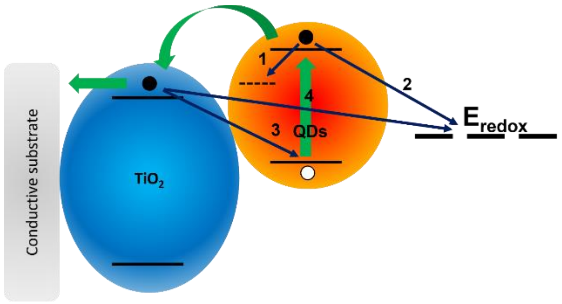

**Figure 9 Principales voies de recombinaison des porteurs de charge dans le dispositif PEC $TiO_2$/QDs/électrolyte**

## Objectifs de recherche

Mon projet de recherche vise à fabriquer des dispositifs de conversion d'énergie solaire à haute performance, en particulier le fractionnement de l'eau PEC par énergie solaire, en améliorant l'efficacité de la génération de charge, du transport et du transport de charge interfaciale à l'interface photoanode/électrolyte (Ƞtotal = Ƞ LHE/ absorption x Ƞ transport x Ƞ interface) et réduire l'effet du processus indésirable de recombinaison des porteurs. Cela peut être fait en stimulant la recherche sur la conception de matériaux à l'échelle nanométrique, la caractérisation de différents dispositifs PEC et l'adaptation de la nanostructure semi-conductrice pour maximiser l'excitation, le fractionnement, l'injection et le transport de charge. Les nanomatériaux ont été choisis en raison de leur rapport surface/volume élevé et de leurs propriétés physiques/chimiques uniques par rapport aux matériaux en vrac qui leur sont associés. Les nanomatériaux manufacturés sont considérés comme les éléments constitutifs des applications modernes de haute technologie. Les nanomatériaux peuvent être fabriqués et adaptés pour atteindre certains objectifs et remplir des rôles spécifiques. Cette flexibilité nous donne la possibilité de mettre en œuvre différentes stratégies pour améliorer les performances des dispositifs PEC.

1. La première stratégie consiste à réduire le processus de recombinaison des porteurs entre la photoanode et l'électrolyte en introduisant du h-BN 2D à l'interface. L'objectif est de passiver les pièges de surface et d'agir comme une barrière d'énergie pour les électrons photoinjectés. De plus, deux semi-conducteurs à large bande interdite différents ont été étudiés ($SnO_2$ et $TiO_2$) en termes de densité de photocourant et de stabilité. Dans les deux cas, les QDs sont utilisés comme matériau de récupération de la lumière et le MWCNT a été incorporé pour améliorer les propriétés de transport de charge.
2. La deuxième stratégie consiste à concevoir une structure de photoanode hybride composée de NR/NP pour améliorer l'efficacité du transport de charge ainsi que le chargement des QDs et la porosité de l'ETL. De plus, une ingénierie de surface par dopage à l'azote, utilisant un traitement à l'hydrazine, a été réalisée pour réduire la concentration de sites de pièges à l'intérieur du $TiO_2$ et réduire le processus de recombinaison des porteurs assistés par piège.
3. La troisième stratégie consiste à fabriquer des NT de $TiO_2$ auto-organisés grâce à un simple processus d'anodisation électrochimique rentable. Les NT peuvent être utilisés à la fois comme modèle pour le dépôt de QDs et comme voie directe pour les porteurs photo-générés. De plus, une jonction p-n à l'échelle nanométrique a été introduite à l'interface pour faciliter le processus de fractionnement de charge pour une meilleure

injection de charge et une plus grande stabilité grâce à un transfert plus rapide des trous vers l'électrolyte.

## Méthodologie

Pour la fabrication de la photoanode

Différentes méthodes ont été utilisées pour fabriquer différentes conceptions de photoanode.

- Les techniques de dépôt par bain chimique et de revêtement par centrifugation avaient été utilisées pour créer la couche de blocage, une petite couche compacte attachée à l'oxyde conducteur transparent (TCO) que nous utilisons, qui est dans notre cas de l'oxyde d'étain dopé au fluor (FTO).
- La couche active, semi-conductrice à large bande interdite ($SnO_2$ ou $TiO_2$) avait été préparée en utilisant la technique de moulage en bande. Ces couches sont responsables du dépôt des QDs et du transport des porteurs de charge photogénèses.
- Le procédé hydrothermal avait permis de développer des nanotiges 1D (NRs) $TiO_2$.
- La technique de revêtement par centrifugation avait été utilisée pour disperser les matériaux 2D sur la photoanode.
- Dépôt direct des QDs, sur la photoanode, par adsorption et réaction successives sur couche ionique (SILAR).

## Caractérisation

- L'efficacité de collecte de la lumière a été étudiée en mesurant la bande interdite optique de l'appareil par spectroscopie ultraviolette visible (UV-Vis).
- L'efficacité d'injection de charge a été étudiée par décroissance de photoluminescence transitoire (PL) et spectroscopie photoélectronique ultraviolette (UPS) pour comprendre la position des bandes de valence et de conduction qui affectent le processus d'injection et de régénération.
- La collecte et l'interface de charge ont été étudiées à l'aide de la spectroscopie d'impédance électrochimique (EIS), où le transport de charge à l'intérieur du semi-conducteur et le transfert de charge à l'interface semi-conducteur/électrolyte peuvent être obtenus.
- L'analyse structurelle de la photoanode est également importante et peut être caractérisée par

- Microscope électronique à balayage (SEM), microscopie électronique à transmission (TEM) et microscopie à force atomique (AFM) utilisés pour la caractérisation morphologique.
- Spectroscopie photoélectronique à rayons X (XPS) utilisée pour la caractérisation chimique et le type de liaison. Spectroscopie à dispersion d'énergie (EDS) pour la cartographie de l'élément à l'intérieur de la photoanode. Spectroscopie infrarouge à transformée de Fourier (FTIR) utilisée pour l'identification chimique.
- Diffraction des rayons (DRX) utilisée pour identifier la structure atomique des matériaux.
- La microscopie à force de sonde Kelvin (KPFM) a été utilisée pour les mesures de potentiel de surface.

Dans le 3-ème chapitre, une photoanode à hétérojonction en tant que composant d'une cellule PEC pour la génération d'hydrogène a été fabriquée. La photoanode composite $SnO_2$/F-h-BN présente des performances supérieures de 60 % à celles de la photoanode SnO2 de référence. Pour améliorer encore les performances de l'appareil, les QDs ont été optimisés de CdS à CdS/CdSe. Les performances augmentent de 2,54 mA $cm^{-2}$ à 5,4 mA $cm^{-2}$ pour l'échantillon nu et de 4,02 mA $cm^{-2}$ à 6,05 mA $cm^{-2}$ pour le F-h-BN avec une stabilité opérationnelle de 87% après quatre heures d'éclairage continu. L'effet de l'épaisseur sur les performances de l'appareil utilisant différentes couches de $SnO_2$ a été mis en évidence. Les performances optimales ont été obtenues avec deux couches, tandis que la meilleure stabilité a été obtenue avec trois couches qui conservent 98 % de la valeur initiale de la densité de photocourant après quatre heures d'éclairage solaire continu (AM 1,5 G, 100 mW $cm^{-2}$). Ensuite, une amélioration supplémentaire des performances de l'appareil a été réalisée en utilisant trois couches de film mésoporeux $SnO_2$ avec MWCNT, ce qui augmente les performances de 11,75 % pour atteindre 6,37 mA $cm^{-2}$. Enfin, l'effet des nanoflakes F-h-BN 2D est étudié en utilisant la désintégration PL, l'EIS et l'UPS pour mieux comprendre la dynamique de leurs porteurs. L'utilisation de nanoflakes F-h-BN montre moins de recombinaison, agissant comme une barrière énergétique entre la photoanode et l'électrolyte. De plus, montrant plus d'injection de charge, en filtrant les sites de pièges et en déplaçant négativement le CB de $SnO_2$, ce qui favorise le processus d'injection de charge. Les résultats de ce projet sont présentés à la figure 10.

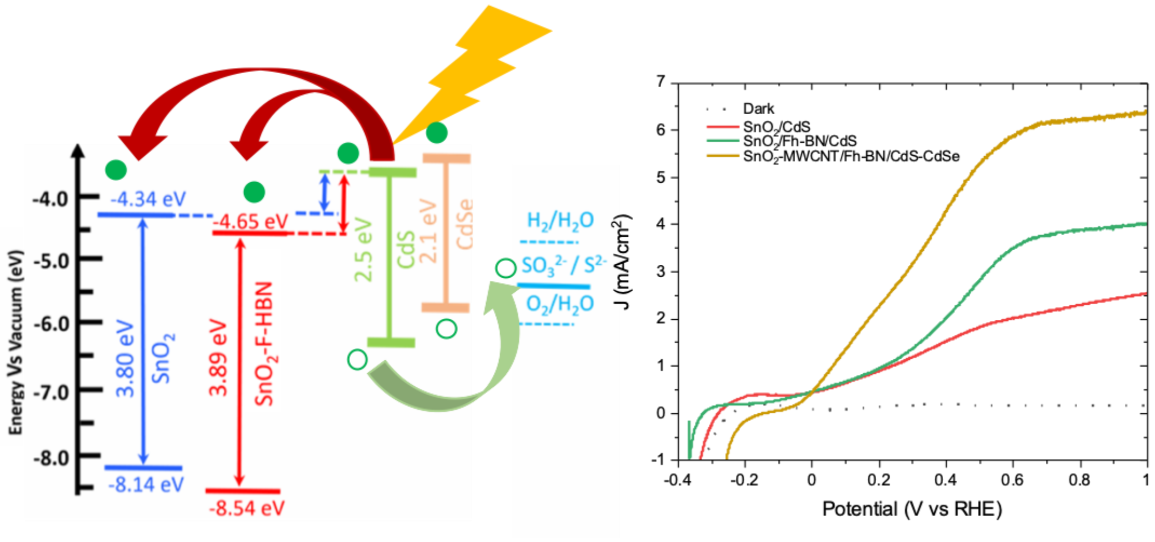

**Figure 10 La structure de bande électronique de la photoanode conçue et la densité de photocourant des dispositifs PEC**

Dans le chapitre 4, des photoanodes structurées hybrides $TiO_2$ NRs/NPs ont été fabriquées et optimisées, puis utilisées dans un dispositif de fractionnement de l'eau PEC à énergie solaire pour la génération de $H_2$. Une série de matrices de $TiO_2$ NRs a été directement cultivée sur les substrats FTO recouverts d'une couche de blocage de $TiO_2$ par synthèse hydrothermale à température constante (150 °C) et concentration de réactif, tout en utilisant un temps de croissance différent (3-5 h). Le processus d'optimisation des NR $TiO_2$ et NP $TiO_2$ conduit à une amélioration des performances de l'appareil, en utilisant des NP avec une épaisseur de 10 µm de 20 nm et des NR avec une épaisseur de 1 µm et un diamètre d'environ 71 nm, pour atteindre une densité de photocourant saturée de 4,25 mA $cm^{-2}$ (à 0,8 V vs RHE), ce qui représente une amélioration de 172 % des performances par rapport au dispositif de contrôle. L'effet du traitement à l'hydrazine sur les performances du dispositif a été mis en évidence, avec une concentration molaire optimale de 0,25 M entraînant une amélioration supplémentaire de 28 % par rapport à la structure hybride $TiO_2$ NRs/NPs de référence. Cette amélioration des performances a été étudiée à l'aide de mesures EIS pour mettre en évidence l'effet de l'azote sur le transport de charge, à l'intérieur du matériau, et le transfert de charge, entre la photoanode et l'électrolyte. Les échantillons traités à l'hydrazine présentent un $R_{ct}$ plus élevé avec l'électrolyte et un $R_{ox}$ interne plus faible des électrons en raison de l'effet d'écran du piège. Des QDs CdS/CdSe ont été utilisés à la place des QDs CdS, pour améliorer encore les performances et la stabilité de l'appareil. La densité et la stabilité du photocourant saturé ont été améliorées de 50 % à 0,8 V et de 13 % après 2 h d'éclairage continu, respectivement. Cette amélioration significative est attribuée à la recombinaison réduite des porteurs non radiatifs et à l'amélioration des taux de photogénération/injection des porteurs de charge. Enfin, une étude informatique détaillée a été menée via DFT + U pour comprendre l'effet de l'hydrazine sur la photoanode. Il a été constaté que la concentration d'hydrazine affecte la configuration de dopage dans $TiO_2$. À une concentration d'hydrazine de 0,25 M, la surface adsorbée au $N_2$ crée des états de bande bien en dessous du CBM, ayant ainsi une faible probabilité d'agir comme un centre de recombinaison tout en agissant comme un écran pour les sites de piège. Cependant, à une concentration d'hydrazine plus élevée (c'est-à-dire 0,5 M), la surface ou le $TiO_2$ dopé au N interstitiel crée des états de bande interdite assez proches du CBM, qui peuvent facilement agir comme centres de recombinaison pour les électrons photoinjectés des QDs au $TiO_2$. Ce travail fournit une nouvelle compréhension du rôle du dopage $N_2$, via un traitement à l'hydrazine, sur les performances des photoanodes structurées hybrides optimisées $TiO_2$ NRs/NPs, fournissant ainsi une stratégie prometteuse pour concevoir la structure de la photoanode pour améliorer les performances des dispositifs PEC. Les résultats de ce projet sont présentés à la figure 11.

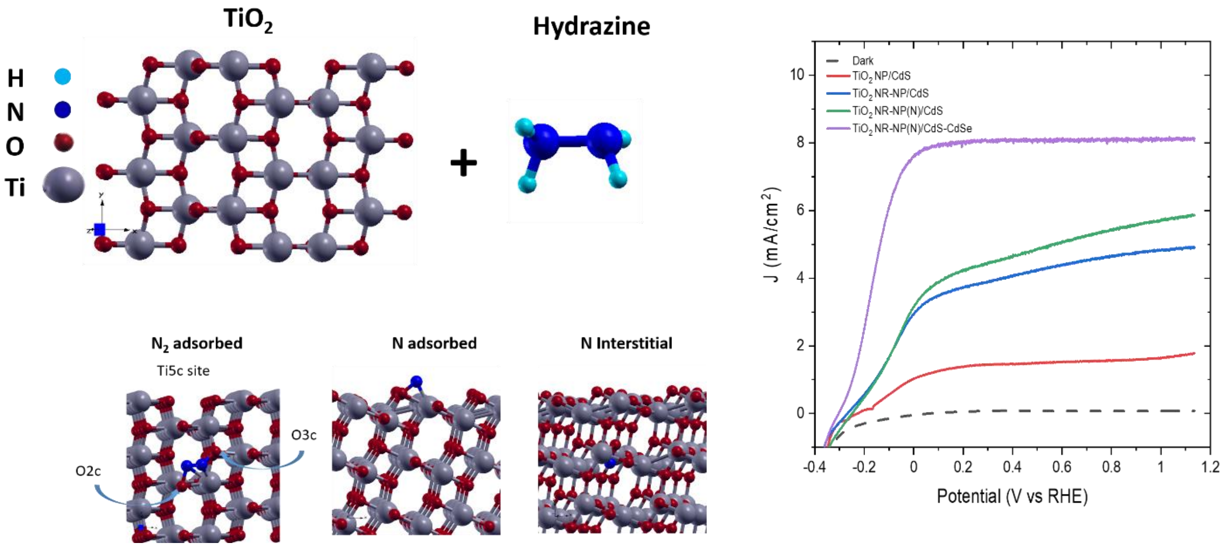

**Figure 11 Différents mécanismes de dopage pour le traitement à l'hydrazine et la densité de photocourant des dispositifs PEC**

Dans le chapitre 5, différentes stratégies pour améliorer les performances des photoanodes de $TiO_2$ ont été étudiées dans le PEC pour la génération de $H_2$. Les méthodes de fabrication utilisées sont réalisées grâce à des processus simples basés sur des solutions à faible coût dans des conditions ambiantes qui facilitent la commercialisation. Le substrat Ti est utilisé pour développer des NT $TiO_2$ autoorganisés qui sont utilisés comme matrice pour le processus de sensibilisation des QDs CdS/CdSe via la méthode SILAR. La sensibilisation entraîne une augmentation de la densité de photocourant qui atteint 4,18 $mA.cm^{-2}$ (à un éclairement solaire, filtre 1,5 AM, 100 $mW.cm^{-2}$), soit 51 fois plus que le dispositif de contrôle. Alors que le changement dans la structure de la photoanode, entre les NP de $TiO_2$ et les NT, avec la même épaisseur et la même sensibilisation QD, entraîne une amélioration de la densité de photocourant d'un facteur 7 lors de l'utilisation de NT de $TiO_2$ par rapport aux NP de $TiO_2$. Ces résultats mettent en évidence l'effet de l'amélioration de l'efficacité du LHE et du transport des porteurs sur les performances globales du dispositif PEC. De plus, le déploiement de l'hétérojonction p-n à l'échelle nanométrique à la surface de la photoanode a été réalisée avec une approche simple et rapide. Le processus ne nécessite que de plonger la photoanode dans une solution à base de Cu pendant 15 s après le dépôt des QDs CdS/CdSe. Le dépôt de CuSe (semi-conducteur de type p) améliore la densité de photocourant de 13 %, atteignant 4,72 mA $cm^{-2}$. Le potentiel de surface pour le dispositif de référence et celui basé sur l'hétérojonction p-n a été étudié par des mesures KPFM dans des conditions d'obscurité et de lumière. Ce travail démontre le potentiel de l'utilisation de NT unidimensionnels comme couche de transport d'électrons et modèle pour le dépôt de QDs pouvant être utilisé dans d'autres dispositifs de conversion d'énergie solaire. L'emploi de NT unidimensionnels et d'hétérojonction p-n à la surface de la photoanode offre une meilleure dynamique des porteurs. Dans l'ensemble, ce travail fournit une voie pour optimiser la structure de la photoanode afin d'améliorer encore les performances de la génération de PEC $H_2$ et d'autres dispositifs optoélectroniques émergents d'une manière rentable qui peut être facilement évolutive dans le secteur industriel. Les résultats de ce projet sont présentés à la figure 12.

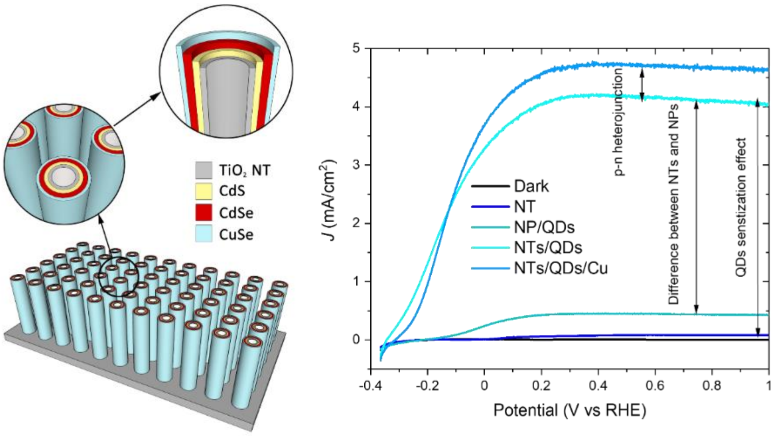

**Figure 12 Représentation schématique de la photoanode conçue et de la densité de photocourant des dispositifs PEC**

# TABLE OF CONTENT

# LIST OF FIGURES

# LIST OF TABLES

# ABBREVIATIONS

| | |
|---|---|
| HDI | Human Development Index |
| UNDP | United Nations Development Program |
| GDP | Gross Domestic Product |
| U.S. | United States |
| CO2 | Carbon dioxide |
| CH4 | Methane |
| Ppm | Part per million |
| Mt | Mega tons |
| UV | Ultraviolet |
| IR | Infrared |
| $H_2O$ | Water |
| $N_2O$ | Nitrous oxide |
| W | Watt |
| $W.m^2$ | Watt per meter square |
| TW | Terawatt |
| PV | Photovoltaics |
| MW | Megawatt |
| H2 | Hydrogen |
| $MJ.kg^{-1}$ | Megajoule per kilogram |
| PC | Photocatalysis |
| PEC | Photoelectrochemical |
| PV-EC | Photovoltaics Electrolysis |
| STH | Solar To Hydrogen |
| $KJ.mol^{-1}$ | Kilojoule per mole |
| eV | Electron volt |
| SC | Semiconductor |
| h | planck’s constant |
| v | Frequency |
| $e^-_{C.B.}$ | Electrons in the conduction band |
| $h^+_{V.B.}$ | Holes in the valency band |
| OER | Oxygen Evolution Reaction |
| HER | Hydrogen Evolution Reaction |
| C.B. | Conduction Band |
| V.B. | Valency Band |
| NPs | Nanoparticles |
| LHE | Light Harvesting Efficiency |
| ETL | Electron Transport layer |
| $TiO_2$ | Titanium dioxide |
| ZnO | Zinc oxide |
| $SnO_2$ | Tin dioxide |
| SQ | Shockley-Queisser |
| AM | Air Mass |
| CIGS | Copper Indium Gallium Sulfide |
| CIS | Copper Indium Sulfide |
| CdTe | Cadmium Telluride |
| N2 | Nitrogen |
| CVD | Chemical vapor deposition |
| PVD | Physical Vapor deposition |
| Co | Cobalt |
| Mn | Manganese |
| Cr | Chromium |
| Ni | Nickel |
| Fe | Iron |
| MEG | Multiple Excitation generation |
| QDs | Quantum dots |
| NIR | Near Infrared |
| 1D | One dimension |
| NRs | Nanorods |
| NTs | Nanotubes |
| NWs | Nanowires |
| MWCNT | Multiwall carbon nanotubes |
| GNR | Graphene nanoribbons |
| 3D | Three dimensional |
| $Fe_2O_3$ | Ferric oxide |
| $BiVO_4$ | Bismuth vanadate |
| nm | Nanometer |
| MgO | Magnesium oxide |
| $SiO_2$ | Silicon dioxide |
| CBD | Chemical Bath Deposition |
| $Ga_2O_3$ | Gallium oxide |
| $In_2O_3$ | Indium oxide |
| $TiCl_4$ | Titanium Chloride |
| ALD | Atomic Layer Deposition |
| $Al_2O_3$ | Aluminum Oxide |
| 2D | Two dimensional |
| h-BN | Hexagonal Boron Nitride |
| pH | power of hydrogen |
| CdS | Cadmium Sulfide |
| CdSe | Cadmium Selenide |
| CuSe | Copper Selenide |
| DFT | Density Functional Theory |
| ITO | Indium tin oxide |
| FTO | Fluorine-doped Tin Oxide |
| Ti | Titanium |
| HCl | Hydrochloric acid |
| NH4F | Ammonium fluoride |
| IPA | Isopropanol alcohol |
| MSA | Methanesulfonic acid |
| Se | Selenium |
| DI | Di-ionized |
| min | minute |
| GC | Gas chromatography |

| | |
|---|---|
| h | hour |
| µl | Microliter |
| mM | Millimolar |
| M-S | Mott–Schottky |
| $^{o}$C | Degree Celsius |
| ml | Milliliter |
| Vol.% | Volume percentage |
| Wt.% | Weight percentage |
| mg/ml | Milligram per milliliter |
| M | Molar |
| SILAR | Successive ion layer adsorption and reaction |
| XRD | X-ray diffractometer |
| XPS | X-ray photoelectron spectroscopy |
| UPS | Ultraviolet photoelectron spectroscopy |
| VBM | Valency band maximum |
| CBM | Conduction band minimum |
| SEM | Scanning electron microscopy |
| TEM | Transmission electron microscopy |
| EDS | Energy-dispersive X-ray spectroscopy |
| AFM | Atomic force microscopy |
| Co/Cr | Cobalt chromium |
| KPFM | Kelvin probe force microscopy |
| UV-Vis | Ultraviolet visible |
| FTIR | Fourier Transform Infrared spectroscopy |
| TRPL | Transient photoluminescence spectroscopy |
| TCSPC | Time-correlated single-photon counting |
| $\tau$ | Electron lifetime |
| $K_{et}$ | Electron transfer rates |
| Pt | Platinum |
| Ag/AgCl | Silver/Silver Chloride |
| RHE | Reversible hydrogen electrode |
| OCP | Open circuit potential |
| LSV | Linear sweep voltammetry |
| IPCE | Incident photon to current efficiency |
| EIS | Electrochemical impedance spectroscopy |
| AC | Alternative current |
| DC | Direct current |
| mV | Millivolt |
| kHz | Kilohertz |
| mHz | Millihertz |
| R | Resistance |
| C | Capacitance |
| CPE | Constant phase element |
| M-S | Mott–Schottky |
| s | seconds |

# CHAPTER 1: INTRODUCTION AND BACKGROUND

The existence of human civilizations depends mainly on energy transformation. Throughout history, the foremost quest has been to find a more concentrated and abundant source of energy that can be converted, in an affordable way and with high efficiency, into heat, light, and motion. Moreover, the efficient use of energy can give rise to more food harvesting, producing various goods, enabling higher mobility, and creating virtually unlimited access to a huge amount of information. Accordingly, the energy conversion, from one form to another, drives every economic activity [1].

The conservation of energy is an important theory that needs to be discussed. The first law of thermodynamics defines the notion of energy conservation. Nevertheless, throughout conversion chains, the useful available energy to perform work diminishes progressively. This inevitable reality is defined by the second law of thermodynamics. In practical terms, in an isolated system, one without any external energy supply, the entropy tends to maximize. This means that the available useful energy for conversion tends to decline. The energy conversion efficiency is defined as the ratio of desirable output to initial input. In a low conversion efficiency process, the energy loss is considerably high. Thus, a fraction of the original energy was transformed into a useful product or service. The total amount of energy is not lost (first law of thermodynamics). However, most of the energy is dispersed as heat (second law of thermodynamics) [2].

## 1.1 Energy consumption

The primary source of energy transformation is the solar energy. The modern world has utilized this renewable energy in two fundamental ways: a) The consumption of fossil fuel stores (crude oil and natural gases), and b) electricity generation through the burning of fossil fuels [3].

The origin of fossil fuels comes from accumulated biomass. The transformation process occurs under pressure and heat over hundreds of millions of years. Fossil fuels' origin is characterized by their high carbon and low water content. This mixture translates into a high energy density source [4]. Moreover, they have given us access to highly concentrated and easy-to-store energy sources. The efficient use of this energy has reshaped every sector of our economy. In turn, more advances have changed the structure and dynamics of existing societies. As a result, there is an increase in average life expectancy, enlarging urbanization, enhancing personal mobility, and transforming international trade into a mass scale [1]. Those activities lead to an exponential increase in the average global energy consumption, as shown in Figure 1.1 [5].

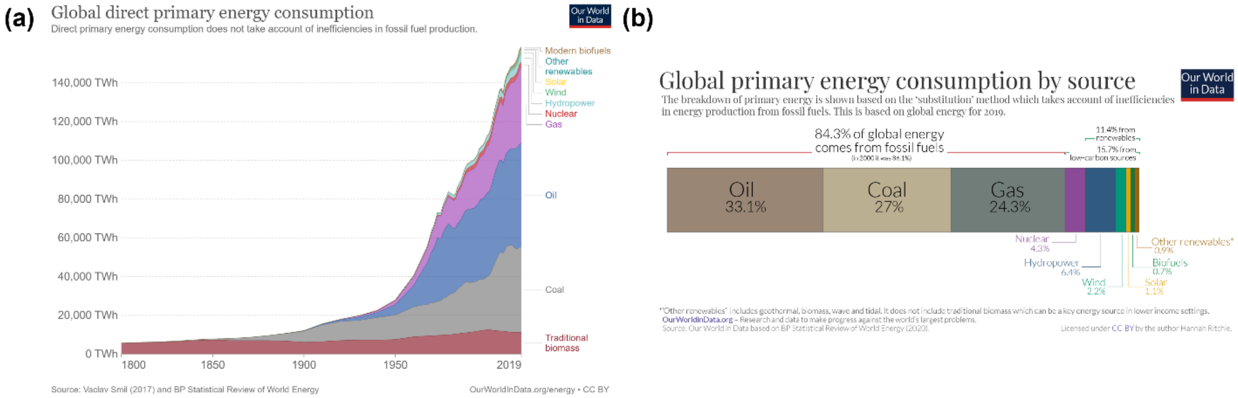

**Figure 1.1 (a) Global energy consumption (b) Source of the global energy consumption [6]**

The future global energy needs are different from one nation to another. This can be realized by the existing energy consumption differences between them. The development of each country can be reflected in the average per capita energy consumption. Only one-fifth of the world's countries have reached the transition to affluent developed societies. The per capita energy consumption of these countries is higher than 120 GJ/capita. [7]. Economic growth and energy consumption go alongside each other to secure a better quality of life. This concept includes the satisfaction of basic physical needs (health and nutrition) and the development of human intellect (ranging from basic education to individual freedoms). The Human Development Index (HDI), created by the United Nations Development Program (UNDP), is a reliable indicator to evaluate different countries [Figure 1.2] [8]. The HDI combines life expectancy at birth, adult reading ability, combined educational enrolment, and per capita gross domestic product (GDP).

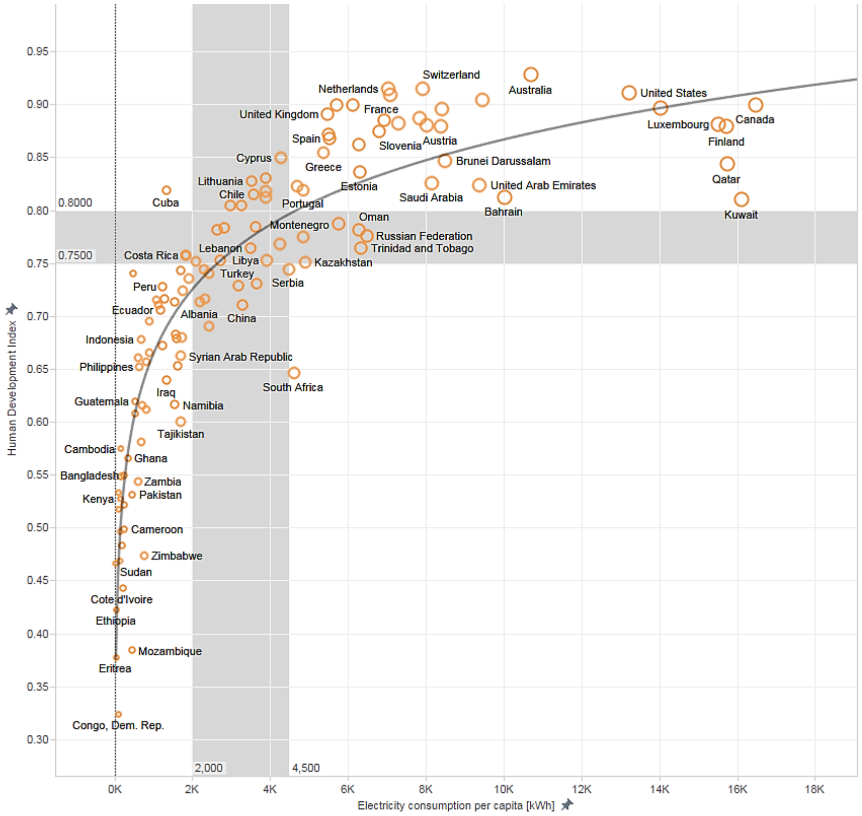

**Figure 1.2 HDI in relation to electricity consumption per capita [9]**

From the HDI figure, energy consumption is thus associated with a better quality of life, only during the early stages of development. Yet, there is no obvious improvement in the fundamental quality of life above 0.8-0.9 HDI level. From Figure 1.2, there is a huge difference in the per capita annual energy consumption between different countries. As an example, consumption in the United States (U.S.) and Canada is roughly thirty times higher than in the poorest countries of sub-Saharan Africa [10]. Despite decades of electrification programs, still 940 million people worldwide do not have access to electricity [11]. This is most noticeable in nighttime satellite images [12]. There is a bright contrast difference between affluent countries and vast areas of darkness over large parts of Asia, Africa, and Latin America. Accordingly, the developing countries need an absolute rising in energy consumption to reach a better quality of life. Nonetheless, the decoupling between economic growth and energy consumption during the early stage of the modern economy is inevitable.

## 1.2 Fossil fuels issues

As discussed earlier, modern civilization has been established on the massive and increasing consumption of fossil fuels. This practice is limited by its abundance, as well as the environmental consequences of burning coals and hydrocarbons. The finite nature of fossil fuels made them unsustainable resources to rely on for future energy demand [13]. However, the most critical challenge of the substantial consumption of fossil fuels is the widespread environmental problems [14]. Rapid climate change arises from the extraction and combustion of fossil fuels. The situation becomes worse with the contribution of industrial production, rapid urbanization, economic globalization, deforestation, and improper practices in crop cultivation and animal husbandry [15]. The accumulative effect of these activities has already reached beyond local and regional crises into destabilizing effects on global climate change. The most undesirable consequence is global warming [16]. The use of fossil fuels and the electricity generated through burning them is the most significant human-caused pollution of the atmosphere and greenhouse gas emissions [17]. The combustion of fossil fuels involves rapid oxidation of their carbon, which produces large amounts of carbon dioxide emissions ($CO_2$). At the same time, methane ($CH_4$), a more powerful greenhouse gas, is released during the production and transportation of natural gas through pipelines. For a long period of time, the atmospheric $CO_2$ concentrations were fluctuating within the range of 250 parts per million (ppm). Now, the $CO_2$ level of the planet shows a steady rising. The concentration surpasses 400 ppm for the first time, which is 40% higher than the era preceding fossil fuels. It is projected to gain another 40% by the century's end [Figure 1.3] [18]. The global warming effect of this change remains highly uncertain. Still, the intergovernmental panel proposed different scenarios for climate change. They predict an average global temperature increase between $+2^{o}C$ and $+4^{o}C$ by 2100. A very worrisome situation, especially when the upper range of that scenario is as high as $+6^{o}C$ [19]. The Paris agreement advises that to control the unpleasant outcomes of global warming, the average temperature should not increase more than $2^{o}C$. This would call for direct substitution of fossil fuels combustion and a prompt transition to renewable energy sources [20].

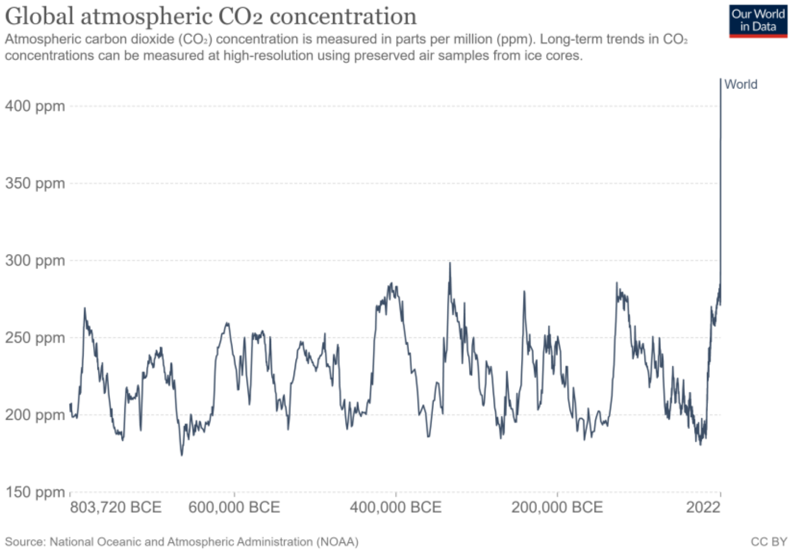

**Figure 1.3 $CO_2$ concentration trend [21]**

## 1.3 Renewable energy

The evolution of renewable energy sources is crucial for a sustainable future. Renewable energies are the source that has originated from the earth's natural resources. Those energies are not finite or exhaustible and have various forms including hydro, wind, solar, biomass, and geothermal [22].

Solar energy is considered the cleanest source of energy. The thermonuclear reactions in the core of the sun convert around 4 megatons (Mt) of matter into energy every second. According to Einstein's mass-energy calculation, the sun generates nearly $3.8x10^{26}$ W of energy [23]. We benefit from 1367 $W/m^2$ (solar constant) of this energy when it reaches the earth's atmosphere [24]. The atmosphere filters out over 70% of solar radiation; Ultraviolet (UV) absorption by ozone & $O_2$, and Infrared (IR) absorption by $H_2O$, $N_2O$, $CH_4$, dust, and $CO_2$. The rest insolation of solar energy reaches an average input of $1.3\times10^5$ TW, which is four orders of magnitude higher than the total worldwide energy consumption [25]. Utilizing a small fraction of solar energy could energize future civilizations consuming energy more than ours. The promising clean solar energy technologies have many long-term benefits such as increasing countries' energy security, reducing pollution, and promoting sustainability. However, converting this abundant flow of solar energy into an affordable energy form is a huge challenge [26].

Solar energy conversion technologies have received significant attention during the last period [27]. Rapid expansion is a common feature of the early stages of development. Photovoltaics (PV) is the technology used to convert solar energy into electricity. Nowadays, PV have a small contributor as compared to other renewable energy technologies. Yet, the installations of new PV modules have been the fastest-growing energy segment lately [28]. Three fundamental reasons makes the PV one of the most appealing renewable energy technology: (1) the availability of the resources used for production, (2) its high power density, and (3) the characteristic advantages of the conversion technique (no moving parts, silent operation, and easy assembly of units) [29]. On the other hand, the major drawbacks are relatively low conversion efficiency and low-capacity factors in less sunny regions. Also, their inherent intermittency poses nontrivial problems in integrating them into existing grids [30]. That is why the contribution of solar energy to electricity generation remains insignificant on the global scale.

The availability of new and inexpensive ways to store solar electricity on massive scales can be a potential solution. Capacities of large storage batteries have gone up by tens of megawatt (MW). What is needed, particularly for the world's growing megacities, is stored on the gigawatt (GW) scale. An alternative practical option is converting solar energy into chemical energy fuel (solar fuel) [31]. Solar fuels utilize abundant resources (i.e., water, carbon dioxide, or nitrogen) to generate energy-rich chemicals (i.e., hydrogen, hydrocarbons, and ammonia). This kind of fuel can be produced and stored for later use. Different technologies were evolved to perform these reactions in a sustainable way [32].

## 1.4 Hydrogen as a fuel

Hydrogen ($H_2$) can be a substantial clean source of energy. Unlike methane, it is not present in the Earth's crust reservoirs, and thus it is produced either from methane or water. $H_2$ has several promising properties that make it an excellent energy source. For instance, its energy density exceeds commercially available energy sources [Table 1.1], and its combustion yields only water as a byproduct. $H_2$ is an ideal synthetic fuel that is non-toxic, lightweight, storable, and transportable [33].

**Table 1.1 Energy density value for different fuels [34]**

| Fuel | Energy density (MJ. $Kg^{-1}$) |
|---|---|
| Hydrogen | 142 |
| Methane | 55.5 |
| Gasoline | 47.5 |
| Diesel | 44.8 |

Three different technologies can be utilized to generate $H_2$ from water using solar energy, as shown in Figure 1.4. (a) Photocatalysis (PC); where photo-active particle suspensions or powder are dispersed in the medium and facilitate both the oxidation and reduction reactions, (b) photoelectrochemical (PEC) water splitting; in which one or more photo-active electrodes (anode and cathode) perform oxidation and reduction reactions in an electrochemical cell, (c) PV electrolysis (PV-EC); independent power is generated by the PV cell unit, which is isolated from the electrochemical cell, and connected to non-photo-active electrodes (anode and cathode) that facilitate water splitting [35].

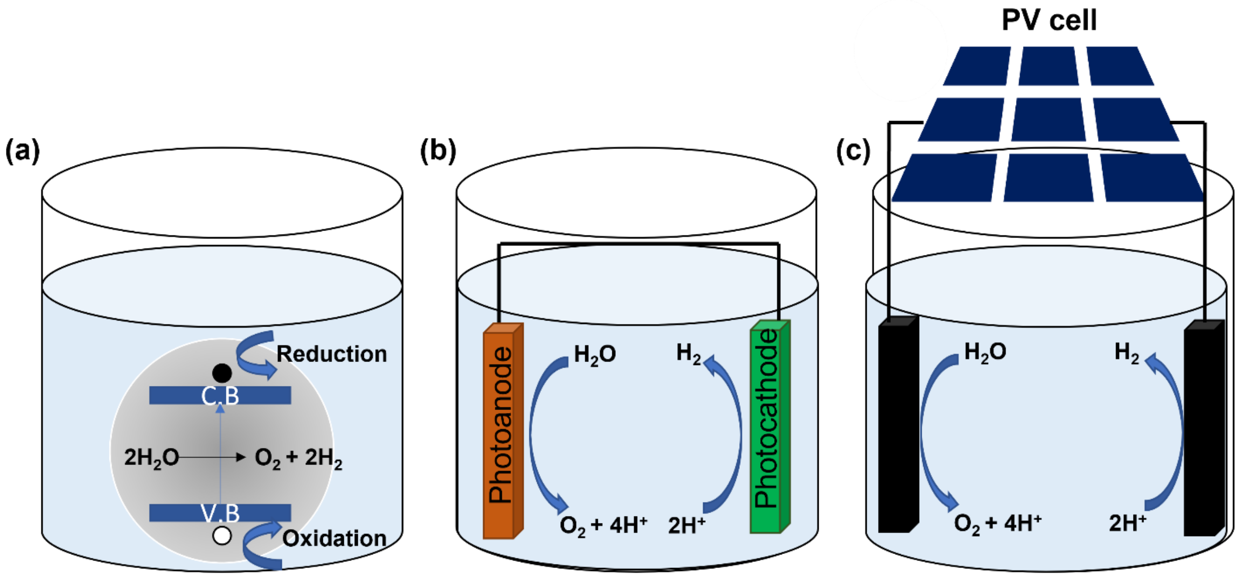

**Figure 1.4 Various solar energy-driven water-splitting systems (a) Photocatalyst (b) Photoelectrochemical (c) PV electrolysis**

From the conversion efficiency point of view, the highest solar to hydrogen (STH) efficiency is obtained through the PV-EC system, followed by the PEC system, and the lowest efficiency is for the PC system. However, the PV panels are complex and associated with a high capital cost, large material intensity in the production, and their manufacturing carbon footprint is higher than PEC or PC. Thus, The PEC system is considered a viable alternative option with lower cost, average lifetime, and has moderate efficiency with a potential improvement [36]. The three main parameters for practical $H_2$ production using solar energy are cost, efficiency, and lifetime. A comparison between different water-splitting systems and those parameters is presented in Figure 1.5.

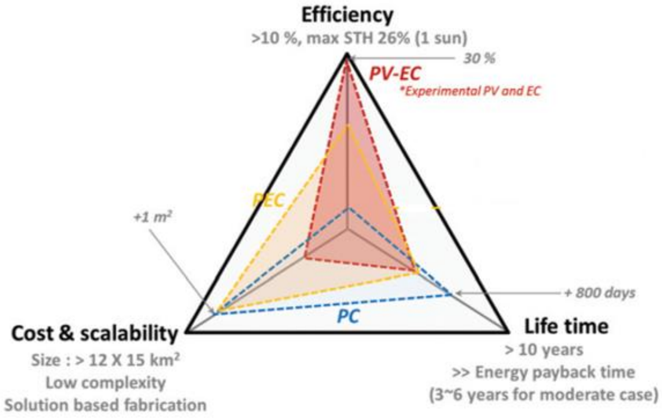

**Figure 1.5 A comparison between PV-EC, PEC, and PC for practical solar-driven hydrogen production systems [36]**

STH efficiency is considered the most important and acceptable benchmark efficiency to characterize the PEC device. It is defined as chemical energy of the hydrogen produced divided by solar energy input. STH is the only metric that can be used to describes the overall efficiency of a PEC water splitting device under zero-bias conditions. In the STH efficiency measurement, the working and counter electrode operate in a two-electrode cell under short-circuited conditions. The existence of sacrificial donors or acceptors should not be included in the electrolyte, as the redox reactions would no longer reflect the true water splitting. On the other hand, other measures are valuable scientifically, providing insight into the functionality and limitations of a material or device, but do not represent device STH performance as it relates to PEC targets. Such measurement can be obtained through three-electrode cell with a reference electrode. It is considered as the most common form of experimentation utilized by PEC researchers. Such measurements bring important insights into material and interface properties [36].

The selectivity of the materials is also a crucial parameter in designing the PEC devices. There is a difference in the material selection criteria in large scall systems as compared to the laboratory devices. The design complexity of the device considered a major factor that can distinguish between the PEC and the PV-EC systems. Lower complexity of the PEC system as compared to the PV-EC one makes it easier for scale up process and from the capital cost point of view. Complexity of the design is represented by the number of layers used in the device fabrication. The direction of the photoelectrode design should goes into reducing the number of layers, which saves the capital cost and simplify the transition into the prototype phase. Usually, the photoelectrode consists of three layers; (1) a substrate for charge collection, (2) electron transport layer (ETL), and (3) the electrocatalyst layer. The PV grade light harvesting material (e.g., c-Si, a-Si, GaAs, InP, etc.) typically exhibit good charge mobility and light harvesting capabilities. However, they are expensive materials and unstable in water. On the other hand, the non-PV grade materials (e.g., $TiO_2$, $SnO_2$, $Fe_2O_3$, $BiVO_4$, etc.) are cheap and stable under water. Nevertheless, they are not good light harvesting materials. So, in the design phase, proper materials selection is important to have an efficient and stable PEC device system. Another important parameter needs to be considered is the elemental abundance of the chosen material [36].

Finally, the stability of the PEC device is considered a crucial parameter. It is important to design a device that can be stable in aqueous solution under solar irradiation. During operation, the photoanode material is oxidized by the photogenerated holes. The chemical stability of material used in the PEC device can be determined by its own oxidation/reduction potential with respect to the redox potential. If the photogenerated charge carriers can move to the oxidation/reduction potential of the material, then it become unstable. From this perspective, the metal oxide semiconductors are stable. However, the non-metal oxide materials require an extra protection layer for its stability. The importance of the stability is directly associated with the life span of the device. The lifetime of the PEC device should at least reach 10 years to be practical [36].

## 1.5 PEC working principle

In a typical procedure, the PEC device is based on semiconductor materials used as a photoanode and/or photocathode. When the electrodes are immersed in an electrolyte solution and illuminated by sunlight, the photon energy is converted to electrochemical energy, which splits water into hydrogen and oxygen [37]. The water-splitting process is considered an uphill reaction, since it requires a standard free-energy change of 237 kJ $mol^{-1}$, which is equivalent to 1.23 eV per electron [38]. During illumination, the semiconductor photoanode generates electron/hole pair through bandgap excitation. Photoexcited carriers are separated at the photoanode/electrolyte interface and transferred to the surface, and then consumed by surface redox reactions. Recombination of the charge carriers takes place alongside the later reactions. Therefore, the charge separation process in the photoanode and the redox reactions that occur at the surface must occur within the lifetimes of photogenerated carriers to achieve a successful water splitting. The oxidation/reduction reactions can exist only if the photogenerated carriers are thermodynamically favorable [39].

For an n-type semiconductor photoanode, once it is immersed in the electrolyte solution, the electrons are consumed from the semiconductor surface until equilibrium is reached. This process happens when the Fermi level is positioned more negatively than the redox potential of the electrolyte solution. The charge transfer results in an interfacial electric field, where the electrostatic potential compensates for the initial difference in the Fermi level. This results in a depletion layer between the electrolyte solution and the semiconductor. Following the equilibrium condition, the Fermi level of the semiconductor is equal to the redox potential of the electrolyte. Knowing that the electrons density at the interface of a semiconductor is finite and the electronic band positions are presumed to be fixed, the electron transfer process creates band bending [Figure 1.6] [40].

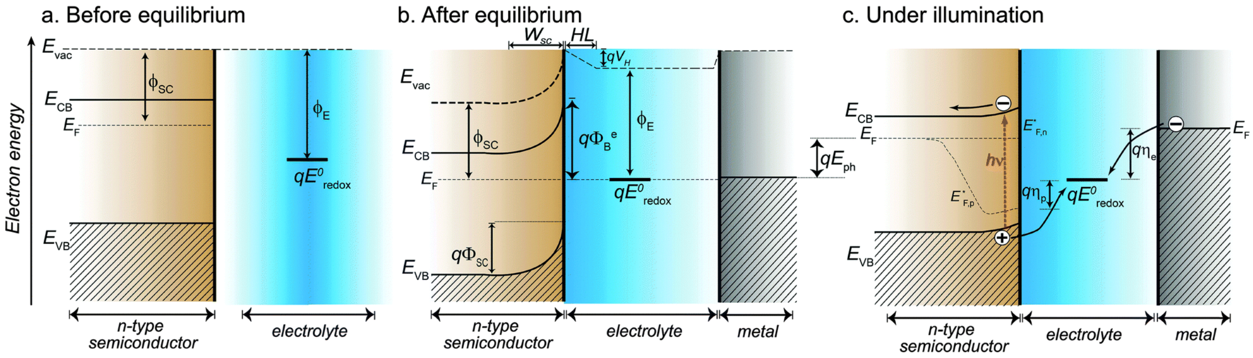

**Figure 1.6 Surface modification occurs at the semiconductor/electrolyte interface in PEC [41]**

The oxidation/reduction reactions of water, as a result of photons-driven water splitting, are described with the following equations:

- Light absorption: SC + hv → $e^-_{C.B.}$ + $h^+_{V.B.}$
- Water oxidation (OER): $2H_2O + 4\ h^+_{V.B.} \rightarrow O_2 + 4H^+$
- Proton reduction (HER): $2H^+ + 2\ e^-_{C.B.} \rightarrow H_2$
- Overall water splitting: $2H_2O \rightarrow 2H_2 + O_2$

**Where SC is semiconductor material**
**h s the Planck constant - 6.62607015 × $10^{-34}$ $m^2kgs^{-1}$**
**v is the photon's frequency**
**$e^-_{C.B}$ is the electrons in the conduction band (C.B.)**
**$h^+_{V.B.}$ is the holes in the valency band (V.B.)**
**OER is Oxygen evolution reaction**
**HER is the hydrogen evolution reaction.**

Additionally, to achieve proper water splitting, various key criteria must be attained by the semiconductor materials [42].

- The semiconductor must generate the necessary voltage upon irradiation to split water (> 1.23 eV).
- The bulk bandgap must absorb a considerable portion of the solar spectrum
- The band edge potentials at the surfaces must be in the range of the hydrogen and oxygen redox potentials (+0 V and +1.23 V vs normal hydrogen electrode, respectively), where the V.B. position is required to be more positive and the C.B. position more negative than the redox potential.
- The PEC device must present long-term stability against corrosion in aqueous electrolytes.
- Minimizing energy losses of the charge transfer, due to kinetic overpotential, at the semiconductor/electrolyte interface, which can reach a range of 1.6-2.4 eV.

The charge carrier's separation and transport are different in the case of nanoparticles (NPs). The effect of band bending might be less pronounced, where the width of the space charge layer (i.e., depletion layer) could be larger than the particle sizes. In contrast, the induced electric field formed by the space charge layer is crucial as it performs a vital role in the charge carrier separation process. The electric field favors the drift of a given charge carrier (e.g., electrons) to the surface and avoids the presence of the other carrier (e.g., holes) on that same surface [43]. In the case of photoanode, the photoexcited holes are accumulated on the surface and are consumed in oxidation reactions, while electrons are transferred to the back contact of the substrate that is connected to the counter electrode via an external circuit where reduction reactions occur [Figure 1.7] [44].

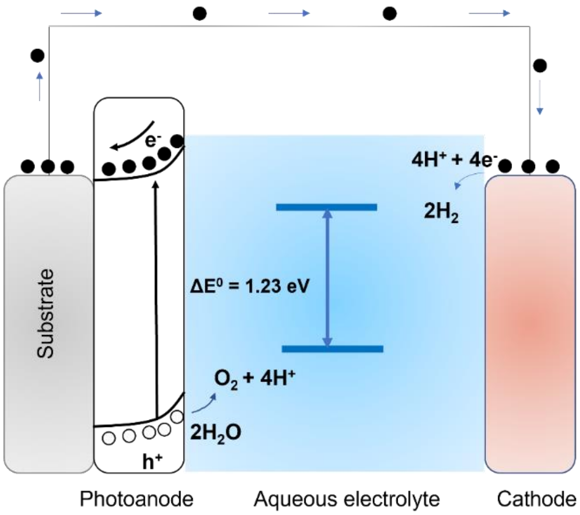

**Figure 1.7 An n-type photoanode water splitting device illustration.**

The fundamental operations in the PEC devices principle depend on (a) the light-harvesting efficiency (LHE), which is associated with the absorption coefficient of the photoactive materials and the probability of charge carrier generation that depends on the bandgap of the photoactive materials; (b) the photoinjected charge transfer efficiency in the ETL, which is affected by the diffusion length and mobility of the charge carriers; and (c) the interfacial charge transport efficiency at the semiconductor/electrolyte interface, where the surface charge potential affects the carrier dynamics and the separation process of the photogenerated charge carrier [36] [44].

## 1.6 Light-harvesting efficiency

The first attempt for solar-driven PEC water splitting was carried out by Honda & Fujishima employing a wide bandgap semiconductor (e.g., $TiO_2$) [45]. However, the conversion efficiency was low because the bandgap of $TiO_2$ is 3.2 eV. It only absorbs photons in the UV region, which contributes to a small portion of the solar spectrum (5%), making them inefficient photoabsorbers [Figure 1.8]. This is the same problem associated with ZnO and $SnO_2$ wide bandgap semiconductors.

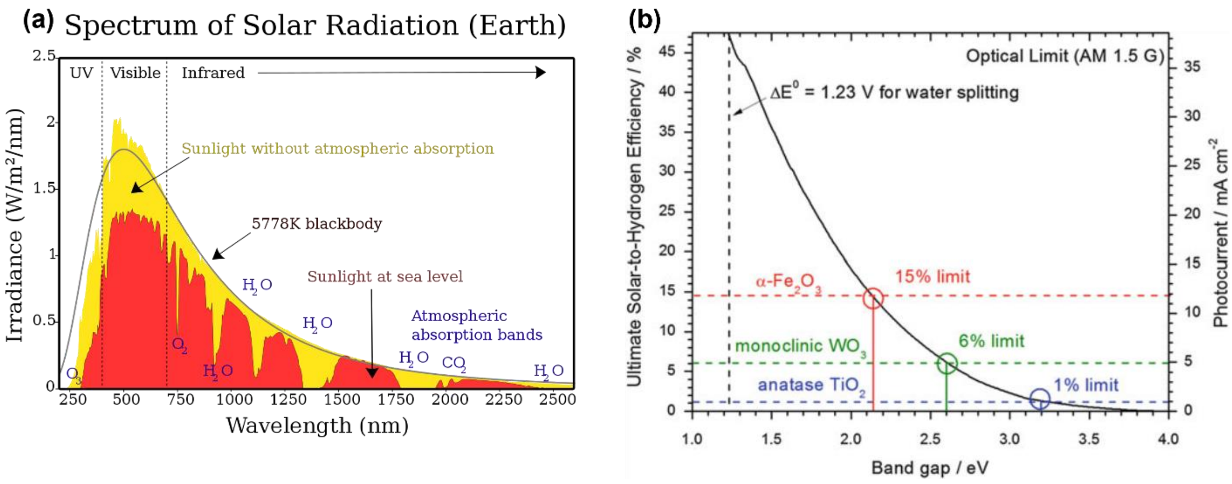

**Figure 1.8 (a) Solar spectrum radiation classification (b) Theoretical maximum STH conversion efficiency as a function of material bandgap [44, 46]**

The third-generation concept of light absorbers considers all innovative attempts to overcome the Shockley-Queisser (SQ) limit at a considerable low-cost [47, 48]. The SQ limit shows the spectral difference between the photons spectrum energy distribution and the semiconductor's bandgap energy [49]. These differences determine two main losses: (a) Inability to convert photons (less energy than the bandgap of the semiconductor), (b) Thermalisation of photons (more energy than the bandgap of the semiconductor). The thermalization process exists as electrons can move easily in different electronic states by emitting phonons, lattice vibration, or heat at a very high speed. From these losses, the theoretical maximum solar energy conversion efficiency is 33.1% at air mass (AM) 1.5 for materials with a 1.34 eV bandgap, as shown in Figure 1.9.

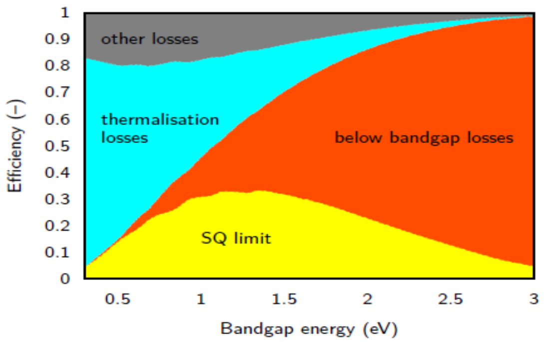

**Figure 1.9 Shockley-Queisser limit and the associated losses as a function of the bandgap of the material [50]**

In crystalline Silicon (first-generation solar cells) or thin-film (second generation solar cells: e.g. amorphous silicon, Copper Indium Gallium Selenide “CIGS”, Copper Indium Selenide “CIS”, and Cadmium Telluride “CdTe”) the charge generation and charge transport processes take place in the same material. Therefore, high-quality materials are essential to prevent the defects and trap sites to be a source of recombination to the photogenerated carrier [51]. Additionally, other drawbacks of crystalline silicon solar cells are the high initial capital cost, high processing temperature, toxic etching chemicals, and expensive clean rooms in the manufacturing processes [52]. While for the thin-film solar cells, they are produced using complex methods, including chemical vapor deposition (CVD) and physical vapor deposition (PVD), which hinder them from scaling up to the industrial sector easily [53]. Therefore, the main objectives of the third generation solar cells are to improve efficiency and reduce cost, as shown in Figure 1.10.

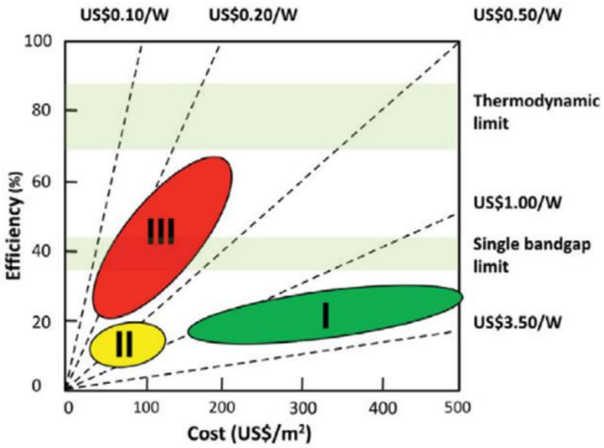

**Figure 1.10 Classification of the first, second, and third-generation solar cells in terms of efficiency vs cost [54]**

To overcome the SQ limit, the third generation solar cells exhibit the following characteristics:

- Intermediate band solar cells [Figure 1.11 (a)]: An artificial energy band is created in the bandgap of the material. The concept is to overcome the problem of the photon energies less than the bandgap energy. The attempt to enhance the light absorption is through tuning the electronic band structure of the wide bandgap semiconductors through doping with transition metal (e.g. Co, Mn, Cr, Ni, Fe) and other co-doping heteroatoms [55-58]. However, the increase in charge carrier recombination centers has reduced the PEC performance of the transition metal-doped $TiO_2$ [59].
- Multi-exciton generation (MEG) [60] [Figure 1.11 (b)]: Light-harvesting materials absorbs photons with high-energy. The photoexcitation process then occurs. In the case of bulk semiconductors, the excess energy is lost as a phonon. However, with specially designed materials (e.g., quantum dots “QDs”), the excess energy can be transferred as a quantized energy package to a neighboring QD. At this point, another photoexcitation process takes

place in the second QD. Accordingly, two electron-hole pairs have been generated out of one large energy photon.

- Hot carrier injection [61] [Figure 1.11 (c)]: The concept here is to avoid the thermalization process. The aim is to collect the photogenerated electrons of high-energy photons before relaxing back to the electronic band edge. Such concept would require selective contacts. Currently, the main challenge is to increase the lifetime of the hot charge carriers, such that enough time exists for electron transfer from the absorber material to the selective contacts.
- Tunable bandgap [62] [Figure 1.11 (d)]: The physical dimensions of a semiconductor have major effects on the electronic properties, especially when these dimensions are reduced to the order of the Bohr radius. The confinement of carriers can be further extended to zero-dimension, resulting in what is known as QDs, which leads to size-dependent optoelectronic properties. So that when the size is reduced, the bandgap energy increases.

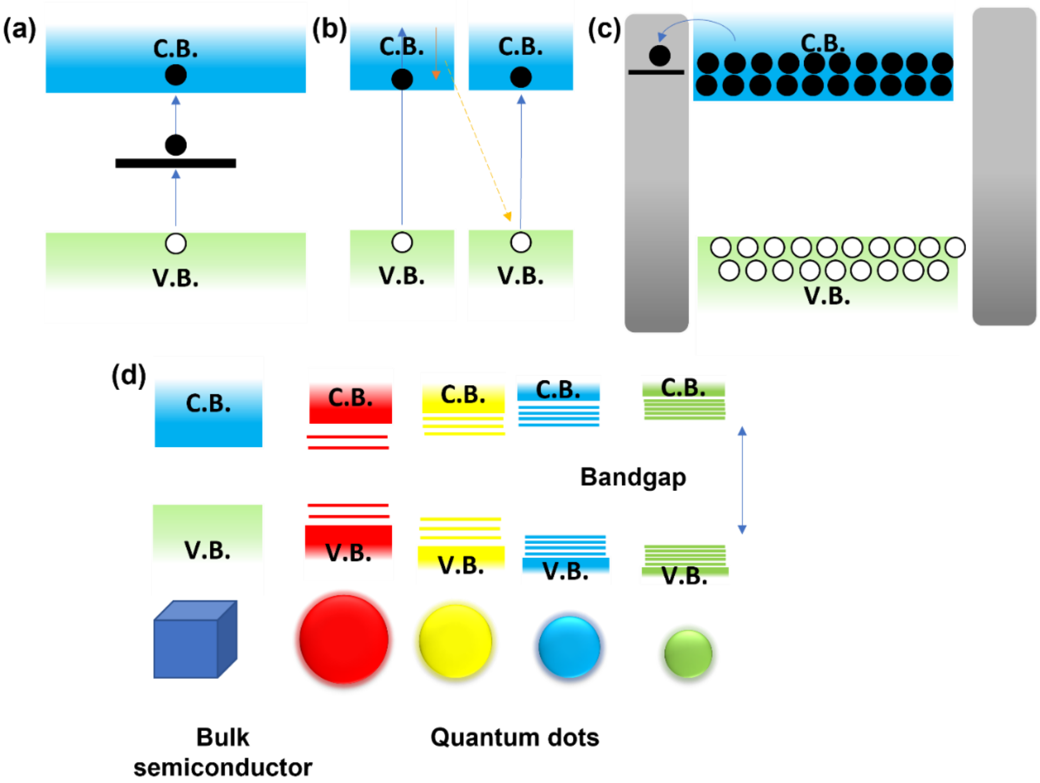

**Figure 1.11 Third generation characteristics (a) intermediate bandgap, (b) MEG, (C) Hot carrier injection, and (d) Tunable bandgaps**

### 1.6.1 Sensitization

Since the pioneering work of O'Regan and Grätzel in $TiO_2$ Dye-Sensitized Solar Cells [63], the idea of sensitization has been widely used. In the mentioned work, the device was based on $TiO_2$ mesoporous film, formed by NPs, and sensitized with dye molecules for light harvesting. The as-synthesized device achieves 7.1% conversion efficiency and exceptional stability. These results made the idea of sensitization wide bandgap semiconductors a practical and feasible approach for solar energy conversion applications. The process includes a wide bandgap semiconductor that is sensitized with third-generation materials, to harvest a wider range of solar spectrum and generate charge carriers. The idea is to synthesize a PV device that has a material with moderate purity, fabricated through a simple technique and low processing cost that can be commercially feasible.

QDs can also be an interesting sensitizer for wide bandgap semiconductors. They are a strong candidate to be employed as the light-harvesting material in the PEC system [64]. QDs are nanosized (2-20 nm) semiconductors with a narrow bandgap, capable of absorbing light in the visible and near-infrared (NIR) regions [65-67]. They exhibit dramatic quantization effects, characterized by an increase in the bandgap with the quantization of the energy levels in discrete values [68]. In most semiconductors, once the size is reduced to a few nanometers, quantum confinement occurs, leading to size-dependent optoelectronic properties of QDs [69]. They can be produced easily with low processing cost (i.e. solution-based synthetic methods are low-cost and simple) [70-72]. As mentioned later, it demonstrates remarkable properties such as tunable bandgap and MEG. In addition, QDs reveal unique electronic properties, due to the unusually high surface-to-volume ratios for these particles. Finally, QDs are durable with higher light, thermal, and moisture stability than dye molecules and lead halide perovskites [73].

## 1.7 Charge transport efficiency

The charge transport efficiency in semiconductors represents the probability of the photogenerated carriers being transported inside the semiconductor bulk and successfully collected by the conductive substrate. The diffusion length is an important parameter that affects the average lifetime of the photoexcited electrons [74]. It is defined as the average distance that the carrier can diffuse before being recombined. The diffusion length depends on two main parameters; electron mobility and electron lifetime. The lifetime is inverse proportional to the number of defects and trap sites and hence the recombination rate. Typically, in QDs sensitized semiconductors applied for PEC water splitting, the charge generation occurs in the QDs then injected into the ETL (e.g. $TiO_2$), if a proper band alignment exists [75]. This injection process was attributed to an interparticle electron transfer process, in which the photogenerated electrons in the C.B. of the QDs are transferred to the C.B. of $TiO_2$. In contrast, the holes in the V.B. of $TiO_2$ are transferred to the V.B. of QDs. This spatial separation of the photogenerated carriers decreases the possibility of charge carrier recombination within the photoanode. Therefore, the role of the ETL is used as a template to deposite the QDs, and transport the photoinjected electrons to the conductive substrate before being recombined [76-78]. The ETL should exhibit the following characteristics to achieve high-performance PEC devices:

- Appropriate C.B. edge as compared to the QDs
- High electron mobility with longer diffusion length
- High surface area to provide a sufficient QD-loading for efficient light harvesting
- Chemical stability, low toxicity, and simple preparation.

### 1.7.1 Morphologies adjustment

To date, several studies and attempts have been reported to enhance the charge transport efficiency in PEC devices. Morphological change of the ETL into one dimension (1D) is considered an interesting strategy. A few morphological examples of this approach are nanorods (NRs) [79, 80], nanotubes (NTs) [81, 82], and nanowires (NWs) [83, 84]. The idea is to provide a directional pathway for the photogenerated electrons. This will result in enhancing the charge transport properties of the material and suppressing carrier recombination. However, the 1D nanomaterials are characterize by a small active surface area as compared to NPs, which consequently offer a lower QDs loading [85]. In addition, 1D structures do not exhibit the ideal porosity, where the electrolyte have to be in contact with a sufficient area of the ETL surface in order to have good carrier dynamics in the PEC device [86]. Hence, it is necessary to consider the photoanode design architecture. The optimum structure must combine both a high transfer rate of the photoinjected carrier, as well as a porous structure for a sufficient QDs loading and proper electrolyte penetration.

An alternative method, to enhance the charge transport efficiency, is by incorporating different carbon-based materials (i.e. multiwall carbon nanotubes (MWCNT) [87], Graphene [88], Graphene nanoribbons (GNR) [89]) that work as efficient electron transport pathways, with low resistance, for the photoinjected electrons to reach the conducting substrate. Deploying a fast track for the electrons to be transported reduces the recombination of the photogenerated carriers, and consequently improves the charge transfer efficiency. The concept is to change the pathway of the photoinjected electrons from a random to a more directional one. NPs film tends to have a high probability of photoinjected carrier recombination due to intrinsic defects within the semiconductor [90]. Therefore, with the addition of a little quantity of carbon materials, a unidirectional flow of electrons is formed and enhance the charge transport efficiency.

Some examples of the strategies mentioned above are Hao-Lin Feng et al. designed a 3D hyperbranched $TiO_2$/ZnO heterostructure for higher QDs deposition and faster charge transfer efficiency [86], while Rusoma et al. incorporate GNR to $TiO_2$ nanoparticles photoanode to enhance the PEC performance [89], and Mahyar et al. incorporated MWCNT to $TiO_2$ to improve the device performance and stability [87].

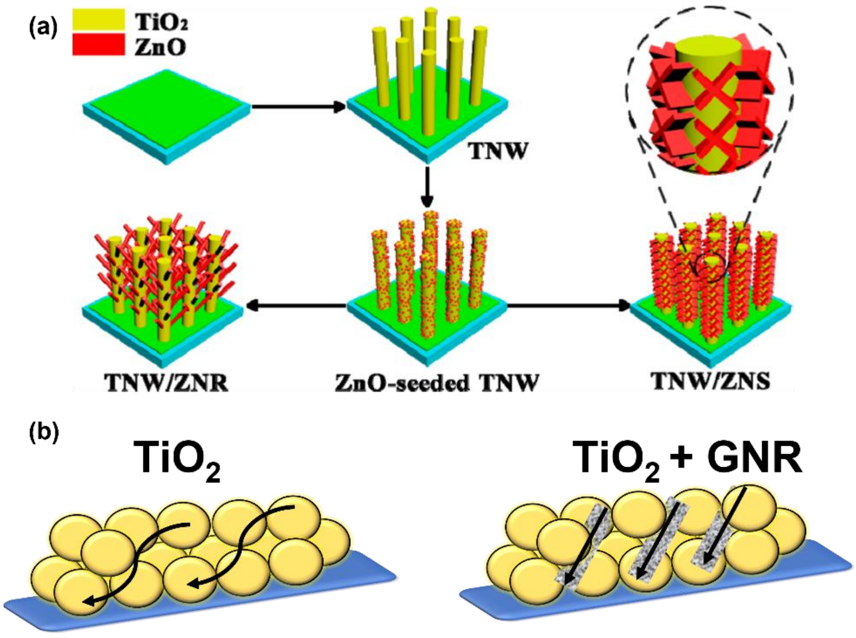

**Figure 1.12 (a) 3D Hybrid structure $TiO_2$/ZnO [86] (b) incorporation of GNR in $TiO_2$ photoanodes**

### 1.7.2 Heteroatom doping

Doping strategies enhance the optical and electrical properties of wide-bandgap ($TiO_2$ [91] and ZnO [92]) and small-bandgap semiconductors ($Fe_2O_3$ [93] and $BiVO_4$ [94]). On the contrary, trap sites can be formed depending on the concentration of the doping material in the crystal lattice. These trap sites act as recombination centers and reduce the PEC device performance [95]. Besides, the doping concentration in the semiconductor could form an intermediate band inside the electronic bandgap structure. This could be undesirable consequences in case of QDs sensitized wide bandgap semiconductor is designed, as it will compete with the QDs in light-harvesting of the solar spectrum.

### 1.7.3 Thickness and particle size control of the ETL

The effect of the photoanode thickness and the choice of particle size can affect different aspects including (1) the QDs loading, (2) the light scattering tendency, and (3) the diffusion length of the charge carriers [96].

1) The QDs loading varies depending on the available active surface area. As the active surface area increases, the QDs loading increases, and consequently, the light-harvesting efficiency increases. For the same amount (i.e., weight) of particles, small-sized particles (e.g., 20 nm) possess a higher surface area than large-sized particles (e.g., 400 nm), which enhances the QDs loading and as a result a higher light-harvesting efficiency.
2) The light scattering tendency inside the photoanode depends on the particle size used. As the particle size increases, the light scattering increases. The advantage of scattering the light is to increase the average path length of the light inside the photoanode, which will enhance the possibility of more light absorption by the QDs. Therefore, the use of large particle size enhances the light scattering process and generates more excitons.
3) The overall thickness of the ETL affects the PEC device performance as it affects the carrier diffusion length of the photoinjected carriers. When the thickness increases, the distance for the photoinjected carriers increases to reach the back contact, and hence the probability for carrier recombination increases. Therefore, the electron lifetime reduces due to the increase of the photoanode thickness, which can be related to several aspects, including (a) the increase of trap assisted recombination process, due to the existence of lattice defects and impurities; and (b) the increase in surface recombination processes, as more unconstructed surface trap sites exist.

## 1.8 Interfacial charge transport efficiency

The surface interface between the photoanode/electrolyte has a significant influence on the carrier dynamics. Since the redox reactions occur at the interface, then the nature of the photoanode surface is an important factor to be considered. The surface characteristics can significantly impact the charge carrier transport efficiency. There is no question that the surface modifications are considered key factors impacting the photocatalyst activity in the PEC water-splitting [97]. The influence of the surface potential, chemisorption properties, and electronic band alignment of the photoanode can impact different parameters including; the redox reactions, the interfacial electron transfer, and resistance to photocorrosion.

### 1.8.1 Passivation of surface states

Different strategies were implemented to enhance the charge separation at the photoanode/electrolyte interface. Surface passivation is crucial to reducing the number of traps in the semiconductor. Different techniques were used in surface passivation, including dip coating in wide bandgap metal oxide (i.e. MgO, $ZrO_2$, $SiO_2$) [98-100], chemical bath deposition (CBD) ($Ga_2O_3$, $In_2O_3$, $TiCl_4$ treatment) [101-103], and atomic layer deposition (ALD) (i.e. thin film of $Al_2O_3$) [104], aiming to reduce the surface traps on the surface.

Another strategy is by applying Two-dimensional (2D) nanomaterials at the interface of the photoanode/electrolyte. Due to the unique structural feature of 2D hexagonal boron nitride (h-BN), such as a strong in-plane sp2 hybridization of the monolayer, it exhibits excellent properties. Some of the key features of 2D h-BN are high transmittance in the visible to NIR region, behaves as an electrical thin insulator layer with a bandgap of 5.9 eV, extremely high strength, chemically stable, and inert under a wide range of temperature and humidity conditions [105, 106]. From this perspective, 2D h-BN can be utilized as both a passivation layer and an energy barrier at the photoanode/electrolyte interface [107]. The passivation layer will suppress the surface traps that occur on the photoanode surface. At the same time, the energy barrier avoids electron recombination, with the oxidized species in the electrolyte, during the PEC device operation. It is worth mentioning that the energy barrier can decrease the rate of photoelectron injection from the QDs to ETL. Thus, the PEC device performance depends on the nature and the thickness of the 2D h-BN layers. Achieving mono-to-few layer can be modified through the functionalization process, which improves its production yield, and more importantly, enhances the exfoliation process. It is crucial to obtain mono-to-few layers of h-BN to reach a proper tunneling current of the photoinjected electrons and overcome the barrier effect. [108].

### 1.8.2 Improving band alignemnt

The PEC device stability and performance depend on the band alignment between the QDs and ETL [109]. The driving force for the photogenerated injection process depends on the difference between the C.B. of the QDs and the C.B. of the ETL [110]. A large difference will accomplish a better rate of injection. On the other hand, the rate of photocorrsion is directly related to the electronic band position of the ETL, QDs, and the redox potential of the electrolyte [111].

Photocorrsion occurs due to the oxidation of the QDs with the photogenerated holes being accumulated at the surface of the photoanode. The accumulation of these holes is caused by insufficient consumption by the oxidizing species in the electrolyte (hole scavengers). Hence, proper band alignment for both the C.B. and V.B. of the photoanode (QDs and ETL) with the redox potential of the electrolyte improve the injection rate of the photogenerated electrons as well as the consumption rate of the photogenerated holes. The alignment favors the transport of the photogenerated holes to the electrolyte and consequently increases the process of the hole scavenger. Therefore, the proper band alignment offers enhanced light-harvesting efficiency and improves the long-term stability of the PEC device.

### 1.8.3 Depositing catalytic overlayers

The surface potential is considered an important parameter in the charge separation process. The formation of a p–n junction at the surface is a suitable strategy to enhance the electron lifetime, which results in an efficient charge carrier separation, and overcoming the recombination processes in the PEC device [42]. The formation of the p–n junction creates a space–charge region at the electrode junction [112]. The diffusion of charges into opposite directions generates an internal electric field in the heterojunction region. Throughout the illumination process and applying bias potential, the internal electric field from the p–n junction supports the charge separation process. Hence, the performance of the PEC water-splitting efficiency is enhanced through the formation of a nanostructured p-n junction.

### 1.8.4 Electrolyte

The carrier dynamics are significantly affected by the interaction between the photoanode and the electrolyte. More interaction is achieved through suitable porosity that can increase the penetration tendency of the electrolyte and the choice of a proper electrolyte. The electrolyte condition, such as pH, could contribute to the stability of the PEC devices [113]. Therefore, tuning the electrolyte composition affect the PEC device performance. In principle, the semiconductor potential at the electrolyte interface can be tuned by adjusting the pH of the solution.

$E°(O_2/H_2O) = 1.23\ V - 0.059\ V \times pH$ (vs NHE) [114]

Besides the pH, the electrolyte must exhibit the following characteristics for stable and high-performance PEC devices:

- Low corrosivity to the QDs
- Appropriate redox potential to regenerate QDs effectively
- High ion conductivity to assist the hole transfer
- Excellent stability (high boiling point) and high transparency in the visible-light range
- Fully regenerative

## 1.9 Recombination pathways in PEC devices

The PEC performance can be summarized by the difference between the charge carrier generation and recombination. In sections 1.6, 1.7, and 1.8 the strategies discussed different ways to improve the generation process. On the other hand, charge carrier recombination is considered one of the most significant factors that limit the performance of the PEC devices. The undesirable carrier recombination can exist in two main ways: (1) inside the wide bandgap semiconductor (e.g. $TiO_2$) [115] and (2) at $TiO_2$/QDs/electrolyte interface [116].

First, there are different types of recombination processes that can occur inside the wide bandgap semiconductor:

a) Radiative recombination [Figure 1.13 (a)]: spontaneous recombination of an electron-hole pair in a direct way. The charge carriers in the C.B. are recombined with the hole in the V.B., and the excess energy is emitted in the form of a photon.
b) Auger recombination [Figure 1.13 (b)]: This process is important in an indirect bandgap semiconductor. In this process both the energy and momentum transfer from one electron to another. It mainly depends on free carrier density. When the carrier density increase, the recombination process increases.
c) Trap-assisted recombination [Figure 1.13 (c)]: It is not direct recombination but rather through impurities and lattice defects. They are located in the forbidden gap “trap state”. It is a dominant recombination process in the semiconductor under most operational conditions.
    - Bulk traps are the density distribution of the bulk trap states within the bandgap of the nanostructured semiconductor. It restricts the movement of electrons and holes. A trap consists of either a chemical impurity or an imperfection in the regular spacing of the atoms. The energy of these defect states goes deep up to the Fermi level. These defects act as traps and affect the electrical properties of the semiconductors. The charge carriers are trapped anywhere in a system until it recombines and does not participate in the charge transport anymore.

d) Surface recombination [Figure 1.13 (d)]: It is a trap state found at the surface of materials originating from unconstructed surfaces.

  - Surface states are formed due to the sharp transition from a solid material that ends with a surface and is found only at the atom layers closest to the surface (dangling bonds on the surface). The material termination leads to a change of the electronic band structure from the bulk material to the vacuum. Forming new electronic states, so-called surface states.

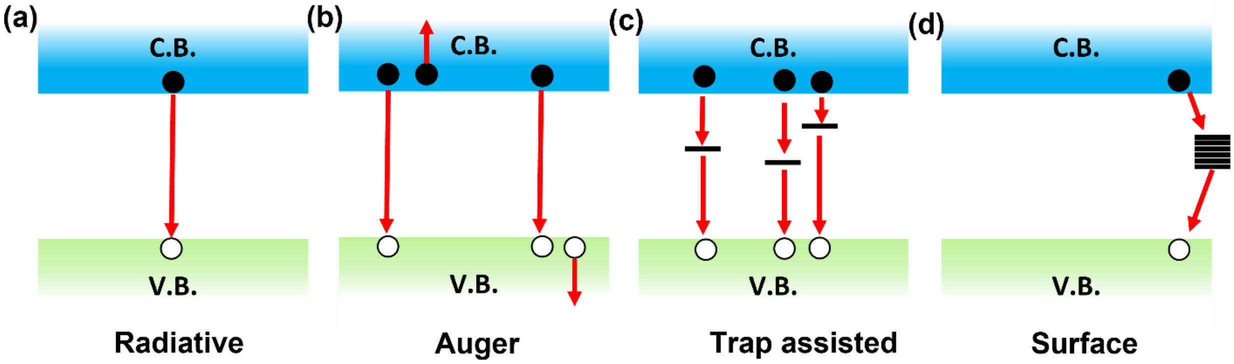

**Figure 1.13 Recombination routes in semiconductors (a) Direct radiate (b) Auger (C) Trap-assisted (d) Surface recombination**

Second, the recombination processes occur in $TiO_2$/QDs/electrolyte PEC devices [Figure 1.14]

1) Inside the QDs (defect states).
2) Excited electron in the QDs with Oxidized species from the electrolyte.
3) Back electron transfer from the C.B. of $TiO_2$ to V.B. of QD.
4) Recombination of electrons in $TiO_2$ with oxidizing species from the electrolyte

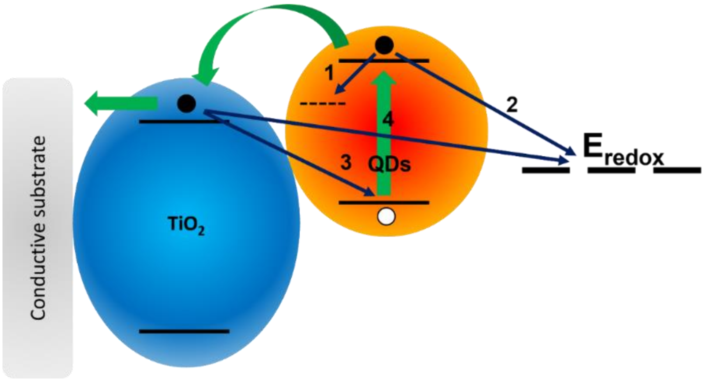

**Figure 1.14 Main charge carrier recombination routes in $TiO_2$/QDs/electrolyte PEC device**

## 1.10 Research Objectives

My research project aims to fabricate high-performance solar energy conversion devices, especially solar-driven PEC water splitting, by enhancing the efficiency of the charge generation, transportation, and the interfacial charge transport at the photoanode/electrolyte interface ($\eta_{total} = \eta_{LHE/absorption} \times \eta_{transportation} \times \eta_{Interface}$) and reducing the effect of the undesirable carrier recombination process. This can be done through stimulating research on nanoscale material design, characterization for different PEC devices, and tailoring the semiconductor nanostructure to maximize charge excitation, separation, injection, and transportation. Nanomaterials were chosen due to their high surface-to-volume ratio and their unique physical/chemical properties as compared to their related bulk materials. The engineered nanomaterials are considered the building blocks in modern high-technology applications. These nanomaterials can be fabricated and tailored to achieve certain objectives and perform specific roles. This flexibility gives us the opportunity to implement different strategies to improve the performance of the PEC devices.

1. The first strategy is to reduce the carrier recombination process between the photoanode and electrolyte by introducing 2D h-BN at the interface. The objective is to passivate the surface traps and act as an energy barrier for the photoinjected electrons. In addition, two different wide bandgap semiconductors were investigated ($SnO_2$ and $TiO_2$) in terms of photocurrent density and stability. In both cases, QDs are used as a light-harvesting material and MWCNT was incorporated to enhance the charge transport properties.

2. The second strategy is to design a hybrid photoanode structure consisting of NRs/NPs to enhance the charge transport efficiency as well as the QDs loading and porosity of the ETL. Moreover, surface engineering through Nitrogen doping, using hydrazine treatment, was performed to reduce the concentration of trap sites inside the $TiO_2$ and reduce the trap-assisted carrier recombination process.

3. The third strategy is to fabricate self-organized $TiO_2$ NTs through a simple cost-effective electrochemical anodization process. The NTs can be used as both a template for QDs deposition and a direct pathway for the photogenerated carriers. Furthermore, a nanoscale p-n heterojunction was introduced at the interface to facilitate the charge separation process for better charge injection and higher stability through faster hole transfer to the electrolyte.

## 1.11 Thesis organization

This thesis is divided into six parts and organized as follows:

**Chapter 1** includes the introduction and background about the Ph.D. research work that presents the research problem, motivation, and the main goals of each project.

**Chapter 2** describes the materials, experimental method in detail, and characterization techniques used throughout different projects.

**Chapter 3** discuss the design and fabrication of a heterojunction photoanode consisting of 2D functionalized hexagonal boron nitride (F-h-BN) nanoflakes. The chapter highlights the effect of the 2D materials on device performance and carrier dynamics. In addition, tailoring the $SnO_2$ film thickness and incorporating MWCNTs were investigated for their effect on carrier dynamics and overall device performance.

**Chapter 4** considers a novel surface engineered hybrid photoanode architecture that combines 1D NRs and NPs to reduce non-radiative recombination. As proof of concept, a PEC device based on the optimized $TiO_2$ NRs/NPs hybrid structured photoanode sensitized with CdS QDs was synthesized and compared to the reference device (with only NPs). The enhancement in charge transport efficiency and prolonged electron lifetime were discussed. Afterward, the optimized $TiO_2$ NRs/NPs hybrid structured photoanode was then treated with hydrazine to engineer the surface traps to further enhance the performance of PEC devices. The role of surface engineering via nitrogen doping is to suppress non-radiative carrier recombination inside $TiO_2$ by screening the trap sites in the electronic band structure.

**Chapter 5** provides the design concept of an engineered photoanode that covers all factors to enhance the performance of the PEC device. The photoanode consists of 1D NTs used as a template to deposit CdS/CdSe QDs, which improve the charge transfer efficiency compared to NPs. A comparison between the device based on NTs and NPs with the same thickness and QDs deposition was discussed. The p-n heterojunction was formed by depositing a p-type CuSe coating over the QDs/$TiO_2$ NTs photoanodes, in which the p-n heterojunction improves the separation/injection rate of the photogenerated charge carrier.

**Chapter 6** summarizes the most significant contributions of my Ph.D. research work and discusses future challenges and perspectives in this field.

Most of the work in this thesis was done by me. However, some parts were conducted through collaboration. More specifically, the synthesization of the 2D F-h-BN was made by Dr. Jasneet

Kaur. Steady and transit Photo Luminescent measurements were conducted by Mr. Jiabin Liu in our group. The Density Functional Theory with Hubbard energy correction (DFT+U) calculations in the second project was performed by Prof. Dr. Kulbir K. Ghuman. Finally, the $TiO_2$ NTs anodization process was made by Dr. Amir Mirzaei.

# CHAPTER 2: MATERIALS, METHODOLOGY, AND CHARACTERIZATION TECHNIQUES

To achieve the research objectives, the photoanodes are fabricated with a proper design architecture. The building blocks of the designed photoanodes are almost the same for each project. However, the novelty of the research exists in the choice of material, doping methods, and incorporation of additional material to execute a specific strategy and enhance the performance of photoelectrochemical (PEC) devices. Moreover, different characterization techniques were conducted to investigate the designed photoanodes in each project. The characterization focuses on morphological, structural, and compositional analysis. Furthermore, the photoanodes were examined with respect to the main PEC operational parameters including light absorption, charge injection and transportation, and Interfacial charge transport efficiencies. Finally, the PEC performance and stability were evaluated using different electrochemical measurements that can reveal the value of the design concept and the state of the art of the PEC device. All the characterization techniques discussed in this chapter were used in this thesis.

In this thesis, the basic structure of the photoanode consists of (1) conductive substrate; (2) blocking layer; (3) electron transport layer (ETL) (4) QDs sensitization.

## 2.1 Materials

The materials used in this thesis are classified as follows:

*The conductive substrates:* The role of the conductive substrate is to build up the photoanode on top of it. It is a passive component that is stable at high temperatures, and it must be conducive to be able to extract the photogenerated electrons. In addition, the substrate surface contributes to determining the efficiency of the photoanode, where the interface is a crucial parameter for the charge transfer properties. There are different types of conductive substrates; (a) polymer, (b) metal, and (c) glass. The problem with polymer substrates is that it is limited to high-temperature processes. While the metal substrates can be corroded by the electrolyte at different pH. Hence, not all metals can be utilized in PEC applications. On the other hand, glass substrate that can be doped to be conductive is the most utilized one. It can be employed in high-temperature synthesis, in addition, it is a passive substrate that doesn’t react with the electrolyte. The most known types are Indium-doped tin oxide (ITO) and Fluorine-doped tin oxide (FTO) coated on a glass substrate.

In this thesis, the FTO was used with sheet resistance ~ 15 ohms $(\text{square})^{-1}$ and was purchased from Pilkington glasses. In addition, a metallic substrate Titanium (Ti) foil with 99.7% purity and 0.9 mm thickness was used and purchased from Alfa Aesar, USA.

*The blocking layer:* The compact thin layer of crystalline material deposited on top of the FTO is called the blocking layer. The objective of this layer is to prevent the photogenerated electrons to recombine back with the oxidized species in the electrolyte after reaching the conductive substrate. In addition, this layer act as a seed layer for the build-up process of the photoanode film. Thus, it reduces the lattice mismatch between the conductive substrate and the ETL film and eventually reduces the number of traps that can act as recombination sites for the photogenerated electrons. Tin (II) chloride dihydrate ($SnCl_2 \cdot 2H_2O$) and titanium (IV) chloride ($TiCl_4 \geq 99.0\%$ (AT)) were used for the growth of the blocking layer and bought from Sigma-Aldrich Inc.

*ETL:* The ETL represents the designed photoanode film and has two main functions. First, it transports the photogenerated electrons from the QDs to the conductive substrate. Second, it works as a template for the deposition of the QDs. This layer can be synthesized using different materials and techniques depending on the desired properties and morphology of the film. The materials used in this thesis are: $SnO_2$ nanopowder (99.9% tin (IV) oxide) was bought from American Elements. Titanium (IV) n-butoxide 99+% was obtained from Alfa Aesar. Concentrated hydrochloric acid (HCl, 36% - 38%) was purchased from VWR chemicals. $TiO_2$ anatase paste 20 nm-NPs sized (transparent, code 18 NR-T) and mixed $TiO_2$ mixed paste 20-450 nm-NPs sized (active opaque, code 18 NR-AO) were bought from GreatCell Solar. Ammonium fluoride ($NH_4F \geq 98\%$) was obtained from Acros Organic, USA. Ethylene glycol ($C_2H_6O_2 \geq 99\%$) was obtained from Fisher Scientific, Canada. Alpha-terpineol, ethylcellulose, titanium (IV) chloride ($TiCl_4$, 0.09 M in 20% HCl), hydrazine solution 35 wt.% in $H_2O$, $ZrO_2$ nano-powder (particle size $<$100 nm), bulk h-BN (powder ~1 µm), Isopropanol (IPA, 70%), and methane sulfonic acid (MSA) were bought from Sigma-Aldrich Inc

*QDs sensitization:* The QDs are the main harvesting material in this design concept. It is deposited on the ETL and injects the photogenerated electrons into the ETL. In this study, simple CdS and CdSe QDs have been utilized. Cadmium acetate dihydrate (Cd $(CH_2COO) \cdot 2H_2O$, 98%), disodium sulfide nonahydrate ($Na_2S \cdot 9H_2O \geq 98\%$), sodium borohydride ($NaBH_4$), selenium powder (Se 99.5+ %), zinc acetate dihydrate (Zn $(CH_3COO)_2 \cdot 2H_2O$, ≥ 98%), and Copper (II) nitrate trihydrate (Cu $(NO_3)_2.3H_2O$, 98.0%), were bought from Sigma-Aldrich Inc. Methanol and ethanol were purchased from VWR chemicals

*Electrolyte:* a mixture between $Na_2S·9H_2O$ and sodium sulfite anhydrate ($Na_2SO_3$, ≥ 98%), which was obtained from VWR chemicals

All chemicals were used as received without any further purification.

## 2.2 Photoanode preparations

### 2.2.1 Substrate cleaning

The cleaning procedure of the conductive substrate is important. All the nanostructured materials are built on top of the substrate surface. Unclean samples can cause a resistance between the substrate and the semiconductor. In addition, the presence of dust or impurities can act as recombination sites and reduce the overall performance of the PEC device. The glass substrates coated with FTO were cleaned with soap and water. Afterward, further cleaning of the FTOs was made through an ultrasonication bath using acetone and deionized (DI) water for 20 and 10 min, respectively. Then dried under nitrogen ($N_2$) stream. Finally, to remove organic contamination, the substrates were treated in an ozone chamber for 20 min. Similarly, Ti foils were cleaned with acetone, IPA, and DI water in an ultrasonication bath for 10 min each, and then dried with $N_2$ gas.

### 2.2.2 Deposition of blocking layer

The blocking layer can enhance the PEC device performance by preventing the recombination of the back electron (i.e., collected electrons) with the oxidized species in the electrolyte [117]. The spin coating technique was used for $SnO_2$ blocking layer deposition. Briefly, 75 µL of 0.4 M $SnCl_2·2H_2O$ in methanol was poured on the FTO and spin-coated for 1 min at 6000 rpm. The samples were then annealed at $500^oC$ for 30 min. For $TiO_2$ blocking layer, a chemical bath deposition process is employed, in which the FTOs were dipped in 40 mM $TiCl_4$ solution for 30 min at $70^oC$. The samples were then washed with DI water, ethanol, and dry air, and subsequently annealed at $500^oC$ for 30 min.

### 2.2.3 ETL Deposition

<u>The deposition of $TiO_2$ and $SnO_2$ nanoparticles (NPs) paste:</u> Different layers of NPs paste were deposited using the tape casting method, also known as the doctor blade approach [Figure 2.1]. This technique is used to deposit the photoanode film on top of the blocking layer. The coating material (i.e., paste) was placed on a glass tube that is spread on the top of the surface, which creates a wet film. After the deposition of each layer, the samples were left to dry at room

temperature for 15 min, then heated at 120$^{o}$C for 6 min. Finally, the film was annealed at 500$^{o}$C for 30 min. The sintering at 500$^{o}$C is important as it brings individual colloidal particles in close contact so that the charge transport and collection properties are improved. In addition, the oxidation at high temperature removes all organic materials (i.e., Terpineol-based paste with ethyl cellulose as blinder) that can be potential trap sites from the metal oxide film [118].

The $TiO_2$ transparent (20 nm) and mixed (20-450 nm) paste were used as purchased. While the $SnO_2$ NPs paste was prepared as follows [119]: 1 g of $SnO_2$ NPs powder was mixed with 0.5 g of ethyl cellulose and stirred with a magnetic stirrer for a few minutes. Afterward, 1 ml of DI water, 1 ml of alpha-terpineol, and 5 ml of ethanol were added to the mixture while stirring. The mixture was stirred for four h to make the homogenous paste.

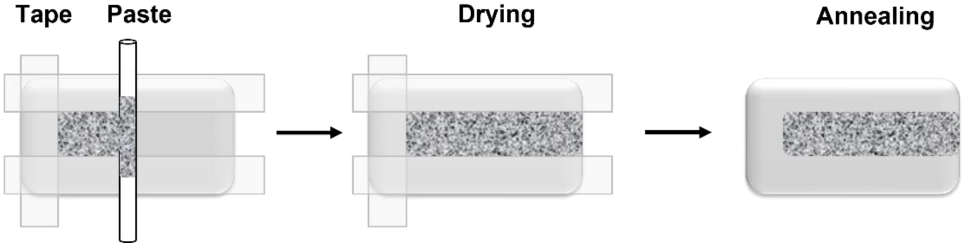

**Figure 2.1 Schematic illustrations of the tape casting method**

The growth of $TiO_2$ nanorods (NRs): A hydrothermal synthesis was used to grow the $TiO_2$ NRs over the $TiO_2$ blocking layer [Figure 2.2] [120]. This process can synthesize crystalline material through a chemical reaction under high temperatures and pressure. A sealed vessel of stainless steel is used to apply pressure that is placed in an electric oven to adjust the reaction temperature. The solution was made with 30 ml of DI water and 30 ml of concentrated HCl. The mixture was sonicated for 10 min in an ultrasonication bath. Afterward, 1 ml of titanium (IV) butoxide was added. After vigorously sonication for another 10 min, the samples were placed against the wall of the Teflon-liner stainless steel autoclave. The conducting side of the FTO substrates was facing downwards. Then, the solution was transferred into the autoclave. The annealing temperature was at 150°C for (3, 4, and 5 h) to obtain different NRs growth. Eventually, all samples with NRs were washed with DI water and dried in ambient conditions, and then annealed at 500°C for 30 min.

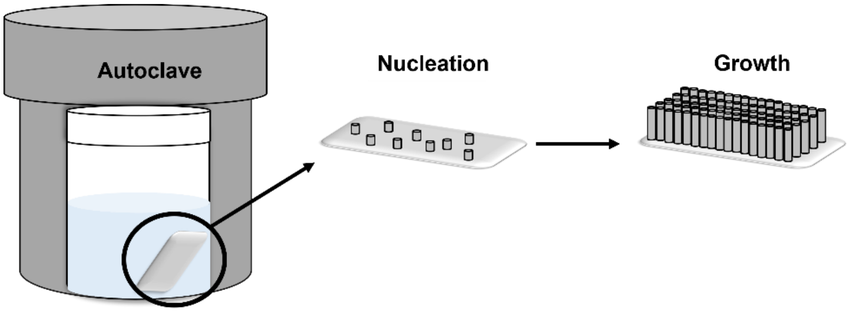

**Figure 2.2 Schematic illustration of the hydrothermal process for NRs growth**

<u>The growth of $TiO_2$ nanotubes (NTs):</u> The anodization process was used to grow the $TiO_2$ NTs from Ti foil [Figure 2.3] [121]. It is an electrochemical process that involves an anode, cathode, and electrolyte. The voltage is applied between the two electrodes and the surface of the anode is manipulated to grow $TiO_2$ NTs. The working and counter electrodes were Ti foil and Pt, respectively. The electrolyte used was made of 97 vol. % ethylene glycol, 3 vol. % DI water with 0.5 wt. % ammonium fluoride. A constant potential of 50 V was applied for 30 and 60 min. The difference in anodization time is to change the NTs length and investigate its effect on PEC performance and stability. After the anodization process, IPA was used for washing in an ultrasonication bath, and a nitrogen stream was used for drying. Finally, the as-prepared $TiO_2$ NTs were annealed at 500$^{o}$C for 1 h.

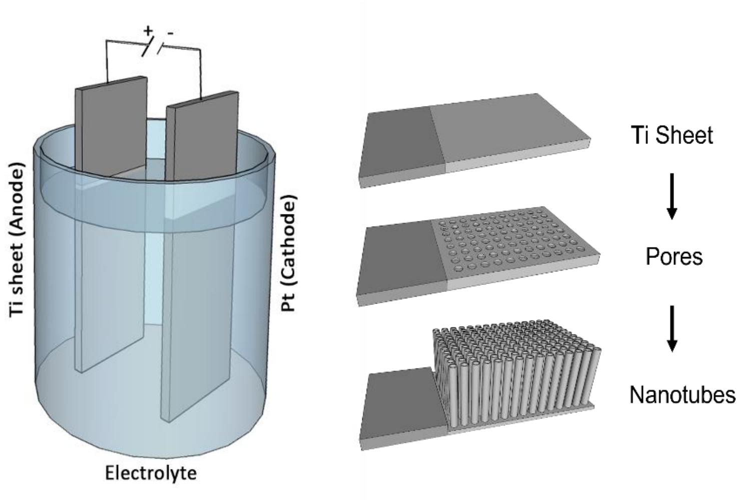

**Figure 2.3 Schematic illustration of the anodization process for NTs growth**

<u>Synthetization and deposition of the functionalized h-BN (F-h-BN):</u> our collaborators (Prof. Jasneet Kaur and Prof. Hadis Zarrin) from Ryerson university prepared the F-h-BN in their lab through the liquid-phase exfoliation technique [122]. The advantage of this process is that it can synthesize few-layered stacking and high-quality F-h-BN nanoflakes from the bulk crystals. The

procedure requires the use of ultrasonication and centrifugation. Precisely, BN bulk powder was dissolved in a mixture of IPA and MSA solutions. A tip sonicator was used for sonicating the mixed solution. Afterward, stepwise centrifugation, of 30 min cycles, was used to centrifuge the F-h-BN solution. After each step, the pellet and supernatant were separated. The final product obtained was a few-layered F-h-BN nanoflake highly dispersed in the solvent. The final concentration of F-h-BN was 0.5 mg/ml. The pellet from the final supernatant was washed several times with IPA to remove the unreacted MSA. Finally, the pellet was dried in an oven at 80°C for 2 h. The yield of the dispersed F-h-BN was about 60% with respect to the initial BN amount.

The spin coating method was used for applying F-h-BN on the surface of the photoanode. Before that, the solution was sonicated for 30 min to obtain a homogenous mixture. Then 50, 100, and 200 µL of F-h-BN were deposited and spin-coated at 6000 rpm for 1 min. Finally, the samples were annealed at 130°C for 3 hrs for complete removal of the IPA solution.

$TiO_2$ passivation layer: The passivation of $SnO_2$ photoanode with a thin layer of $TiO_2$ is important for the removal of the surface traps. It is performed with the same procedure as the $TiO_2$ blocking layer through chemical bath deposition. The $SnO_2$ samples were dipped in $TiCl_4$ solution with 50 mM concentration for 1 hr at 70°C. After that, the samples were washed with DI water, and ethanol, and dried with air. Finally, the samples were annealed at 500°C for 30 min.

Hydrazine treatment: The hydrazine treatment was used for surface engineering and screening the bulk traps of the photoanodes samples. In a typical procedure, the photoanodes were dipped in a hydrazine solution with different concentrations (i.e., 0.25M, 0.5M, and 1M). The solution was preheated at 70°C, then the samples were dipped for 30 min. Afterward, the samples were dried in ambient conditions and finally annealed at 500°C for 30 min.

Thin layer of $TiO_2$ NPs: 1 µm film thickness of $TiO_2$ 20 nm-NPs was prepared using the spin coating method. A mixture of 200 mg of the $TiO_2$ transparent paste and 1.2 ml of ethanol was prepared and sonicated for 30 min. For the spin coating, 100 µl of the mixture was poured on the Ti sheet and spin-coated for 1 min at 6000 rpm. The samples were annealed first at 120°C for 6 min, and then at 500°C for 30 min.

### 2.2.4 QDs sensitization

The QDs were sensitized using a low-cost simple solution process via successive ionic layer adsorption and reaction (SILAR) [Figure 2.4]. The CdS, CdSe, and ZnS QDs were directly grown on the photoanodes using the SILAR method. The process is made by dipping the photoanode in cationic and anionic precursors successively for 1 min. After each dipping, the photoanode was washed using the same solvent as the corresponding precursor and subsequently dried with nitrogen.

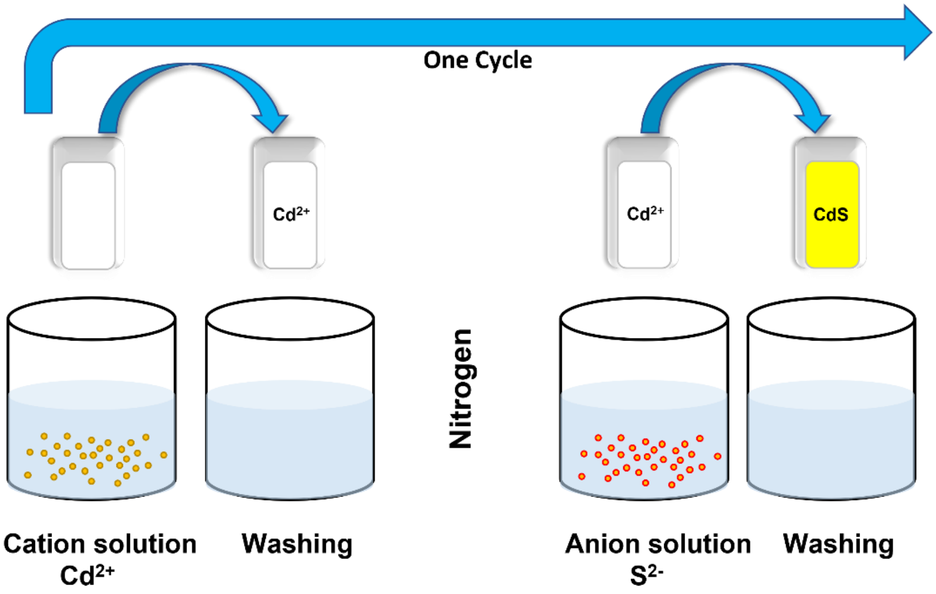

**Figure 2.4 Schematic illustration of CdS SILAR cycle**

The precursors for cationic solutions used to deposit $Cd^{2+}$ and $Zn^{2+}$ are (0.05 M and 0.03 M $Cd(CH_2COO)\cdot 2H_2O$ in 20 ml of methanol) for CdS and CdSe, respectively, and (0.1 M $Zn(CH_2COO)\cdot 2H_2O$ in 20 ml of methanol) for ZnS.

The precursors for anionic solutions used to deposit $S^{2-}$ and $Se^{2-}$ are (0.05 M and 0.1 M of $Na_2S\cdot 9H_2O$ in 20 ml of DI water/methanol (1:1)) for CdS and ZnS, respectively, and a mixture of (0.06 M of $NaBH_4$ and 0.03 M of Se powder in 40 ml of ethanol) for CdSe.

p-n heterojunction formation: A p-n heterojunction was formed by depositing a p-type semiconductor (CuSe) after the deposition of an n-type semiconductor (CdS/CdSe QDs). In a typical procedure, a 2.5 mM $Cu(NO_3)_2.3H_2O$ solution was used to deposit the Cu, after the third SILAR cycle of the CdSe QDs. The photoanodes were immersed in the as-prepared Cu solution for 5, 10, 15, and 20 s. The Se deposited on the photoanode reacts with Cu to form CuSe. Different immersion times represent different CuSe thicknesses. The variation in CuSe thickness was investigated in the performance of the PEC device.

The final photoanode design architecture was as follows in each chapter:

- In the third chapter, the conductive substrate used was FTO. A $SnO_2$ blocking layer was deposited into the FTO substrate. Then several layers (i.e., 1, 2, and 3 layers) of $SnO_2$ paste were deposited on top of the blocking layer. Afterward, a thin passivation layer of $TiO_2$ was applied to the $SnO_2$ photoanode. Finally, the F-h-BN was placed on the top of the $SnO_2/TiO_2$ photoanode. Likewise, the same procedures were made for $TiO_2$ instead of $SnO_2$ for comparison. The photoanodes were sensitized with 7 cycles of CdS and 2 cycles of ZnS QDs and another with different cycles of 5 CdS, 3 CdSe, and 2 ZnS QDs.
- In the fourth chapter, the conductive substrate used was FTO. A $TiO_2$ blocking layer was deposited on the FTO surface. Then $TiO_2$ NRs were grown over the blocking layer with different growth times through the hydrothermal process. After that, two layers of $TiO_2$ paste were deposited on top of the photoanode to create the hybrid $TiO_2$ NRs/NPs structure. Finally, the photoanodes were treated with hydrazine for screening the trap sites. The QDs sensitization was with 5 cycles of CdS and 2 cycles ZnS and another with 5 cycles CdS, 3 cycles CdSe, and 2 cycles of ZnS.
- In the fifth chapter, the conductive substrate used was Ti foil. Then the $TiO_2$ NTs were directly grown over the Ti foil through the anodization process. The $TiO_2$ NTs photoanodes were sensitized with 5 cycles CdS, 3 cycles CdSe and 2 cycles of ZnS. In addition, the p-n heterojunction was made by depositing the CuSe layer. For comparison between the $TiO_2$ NTs and NPs based PEC devices, a thin layer of $TiO_2$ NPs with the same thickness as NTs was deposited on the Ti foil and sensitized with the same QDs.

## 2.3 Characterization techniques

Different characterization techniques were used to examine and understand the designed structure of the photoanode. The crystallinity, chemical composition, morphology, optical properties, electronic band structure, and electrochemical performance were investigated to shed more light on the design concept and justify the choice of material and synthesizing process. In addition, characterization techniques were used to justify the main objectives of each project.

### 2.3.1 X-ray diffraction (XRD)

To examine the crustal structure and phase transformation of the designed photoanodes, XRD scan was employed. The working principle of XRD is illustrated in Figure 2.5, based on Bragg's law:

$$n\lambda = 2dSin\theta \text{ (Equation 2.1)}$$

**where d is the distance between two parallel planes periodically arranged**
**$\lambda$ is the wavelength of a monochromatic X-ray source**
**$\theta$ is the diffraction angle.**

XRD patterns were acquired using a Philips X'pert diffractometer with Cu $K_\alpha$ (α = 0.15406 nm) radiation source.

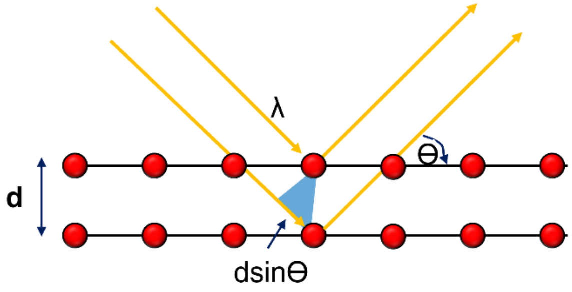

**Figure 2.5 XRD working principle**

### 2.3.2 X-ray photoelectron spectroscopy (XPS)

XPS is a technique for analyzing the surface chemical composition of a material. The XPS spectra are obtained by irradiating the photoanode surface with a beam of X-rays. A photoelectron spectrum is recorded by counting the ejected electrons over a range of electron kinetic energies on the surface of the material being analyzed.

$$E_k = hv - E_b - \emptyset \quad (Equation\ 2.2)$$

**Where $E_k$ is the Kinetic energy of the photoelectron**
**$hv$ is the incident photon energy**
**$E_b$ is the electron binding energy**
**$\emptyset$ is the work function (the difference between fermi level and vacuum level).**

XPS VG Scientific Escalab 220i-XL system was used with a monochromatic aluminum energy source of 1486.6 eV. The results were analyzed using Casa XPS software for obtaining the elemental composition, bonding type, and the position of the valence band maximum (VBM) of the photoanodes [123].

### 2.3.3 Ultraviolet photoelectron spectroscopy (UPS)

UPS uses the same concept as XPS. But instead of applying an x-ray source, ultraviolet photons are utilized. UPS with He I radiation energy source of 21.22 eV was used to estimate the Fermi level and VBM energy level of the photoanodes.

The ionization potential ($I_P$) can locate the position of the VBM with respect to the vacuum level ($E_{vac}$). It is calculated by adding the work function ($E_{He}$ “21.22” – Binding energy of the secondary edge) to the valency band offset ($E_f$ – $E_{VBM}$) as shown in Figure 2.6.

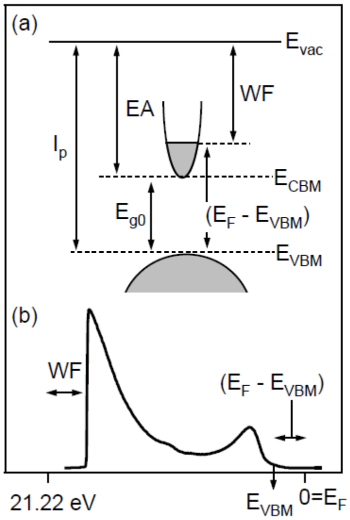

**Figure 2.6 (a) electronic band structure of a semiconductor (b) the results from the UPS measurement [124]**

### 2.3.4 Scanning electron microscopy (SEM)

The morphology of different ETL structures was studied by using SEM. A beam of electrons scans the sample’s surface under vacuum to obtain structural and chemical information. When the electron beam hit the sample, the secondary electrons were collected to recognize the morphology, while the characteristic elemental x-ray was analyzed with energy-dispersive X-ray spectroscopy (EDS) for elemental identification and mapping. The SEM images and EDS data were acquired with Tescan LYRA 3 equipment.

### 2.3.5 Transmission electron microscopy (TEM)

TEM is an alternative electron microscope technique used for morphological study. It applies the same principles as SEM. However, instead of scanning the surface and collecting the secondary electrons in the SEM, the electron beam passes through the sample and the transmitted electrons were collected. TEM was utilized to identify the detailed structure of different nanomaterials at high magnification. The TEM images were captured using a JEOL 2100F TEM.

### 2.3.6 Atomic force microscopy (AFM)

AFM is also high-resolution microscopy. The scanning probe can identify precisely the surface using different operating modes (e.g., contact, non-contact, and tapping). In a typical procedure, an extremely sharp tip is used to scan the surface for topography imaging. While scanning, the attraction or repulsive forces between the tip and surface identify the sample topography. In this work, the AFM used was an Enviroscope AFM system (Veeco Instruments, now Bruker) operating in tapping mode at room temperature, equipped with a magnetic Co/Cr-coated tip (MF-M01, NT-MDT) with a radius at the apex ~40 nm).

Kelvin probe force microscopy (KPFM) was employed for the surface potential analysis of different photoanodes. To stimulate light and dark conditions, the LED light was turned on and off inside the KPFM while operating.

### 2.3.7 Ultraviolet-visible spectroscopy (UV-Vis)

In the UV-Vis spectroscopic measurement, the extent of light absorption as a function of wavelength is obtained. It provides information about optical properties and the optical bandgap for the material employed. The optical bandgap is the difference between the VBM and CBM. Two modes were used in this study: (1) transmission mode; used for the photoanodes based on FTO substrate and (2) Diffuse reflectance mode; used for photoanode with Ti substrate. The fraction of light absorbance is described by the Beer law.

$$\boldsymbol{A = log_{10}(\frac{I_0}{I})} \ (\textbf{Equation 2.3})$$

**where A is the absorbance**
**I is the measured transmittance or reflectance**
**$I_0$ is the incident intensity**

The absorption coefficient of the material $\alpha$ (cm$^{-1}$) can be calculated from the absorbance A divided by the thickness of a film $l$.

$$\boldsymbol{\alpha = \frac{Ln\ (10)\ x\ A}{l}} \ (\textbf{Equation 2.4})$$

To determine the bandgap energies from the UV-Vis results, the data was plotted and fitted to the expected trendlines for direct and indirect bandgap ($E_g$) semiconductors using the following equation.

$$\boldsymbol{\alpha h\nu \ \alpha \ (h\nu - E_g)^{\frac{1}{n}}} \ (\textbf{Equation 2.5})$$

Where n takes different values depending on the bandgap; 3 indirect (forbidden), 2 indirect (allowed), 3/2 direct (forbidden), or 1/2 direct (allowed) transitions. Since most of the semiconductors used in this thesis are direct allowed bandgap transition, then n was used with 1/2.

The extrapolation of the baseline determines the optical bandgap from Tauc plots ($\alpha h\nu$ vs $h\nu$).

$$\boldsymbol{h\nu = \frac{1240}{\lambda}} \ (\textbf{Equation 2.6})$$

### 2.3.8 Fourier-transform infrared spectroscopy (FTIR)

FTIR is used to determine the molecular composition of the photoanodes by analyzing the absorption of the materials over a range of wavelengths in the IR region. When the sample is illuminated with IR radiation, some of these energies are absorbed while the others are transmitted. The signal that reaches the detector is a fingerprint spectrum of a certain molecular composition of the sample. The importance of FTIR is that it can identify different chemical structures simultaneously, which produce different spectral fingerprints for each component. The final signal that reaches the detector is decoded using Fourier transformation mathematical technique. The results are shown as a spectrum graph and a reference library is used for the identification.

### 2.3.9 Transient photoluminescence spectroscopy (TRPL)

TRPL was used to measure the electron transfer rate and the lifetime decay of the photogenerated electrons in different photoanodes sensitized by QDs. Time-correlated single-photon counting (TCSPC) mode was applied with a 444 nm laser. Exponential decay was used for fitting the recorded results. The average lifetime ($\tau$) was calculated using the following equation:

$$\boldsymbol{\tau = \frac{\alpha_1 t_1^2 + \alpha_2 t_2^2 + \alpha_3 t_3^2}{\alpha_1 t_1 + \alpha_2 t_2 + \alpha_3 t_3}} \ (\textbf{Equation 2.7})$$

**Where $\alpha_i$ is the fitting coefficient**
**$t_i$ is the characteristic lifetime of the TRPL decay.**

While the electron transfer rates ($K_{et}$) were calculated from the difference between the electron lifetime value of the photoanodes and the reference sample:

$$\boldsymbol{k_{et} = \frac{1}{t_{Photoandoe}} - \frac{1}{t_{Reference}}} \ (\textbf{Equation 2.8})$$

## 2.4 PEC measurements

For all PEC measurements, a three-electrode configuration cell was used as shown in Figure 2.7. The working electrode is the photoanode, the counter electrode is platinum (Pt), and the reference electrode is saturated Ag/AgCl. A sulfide aqueous media was used as the electrolyte solution with pH 13. The electrolyte function as a hole scavenger. It consists of a mixture between 0.25 M $Na_2S \cdot 9H_2O$ and 0.35 M $Na_2SO_3$. Before each PEC measurement, $N_2$ was purged on the solution for 30 min to remove any dissolved oxygen. The active surface area of the photoanodes is 0.15 ~ 0.2 $cm^2$, while the rest was covered with epoxy. The sun simulator used was Class AAA (model SLB-300A by Sciencetech Inc.) with a light source of 300 W xenon arc lamp, and the light was filtered with AM 1.5G filter. A calibration step of the light intensity was made before each measurement by using a reference silicon cell. The light intensity was adjusted to 100 mW $cm^{-2}$ (one sun). A Gamary potentiostat was used for all the electrochemical measurements (interface 1010 E).

In the three-electrode configuration, the measurement of a working electrode is with respect to the reference electrode. It is the most common form of experimentation used for PEC measurements. The benefit of this configuration is that it provides valuable insight into the material and interface properties. It is essential to understand the properties of the photoanode rather than the assembly of a full device. However, the drawback is that this type of cell cannot provide valid device efficiency (i.e., STH). The reported potential was converted from Ag/AgCl to the reversible hydrogen electrode (RHE) using the following equation.

$$\boldsymbol{E_{RHE} = E_{Ag/AgCl} + 0.059\ x\ pH + E^{0}_{Ag/AgCl}\ (Equation\ 2.9)}$$

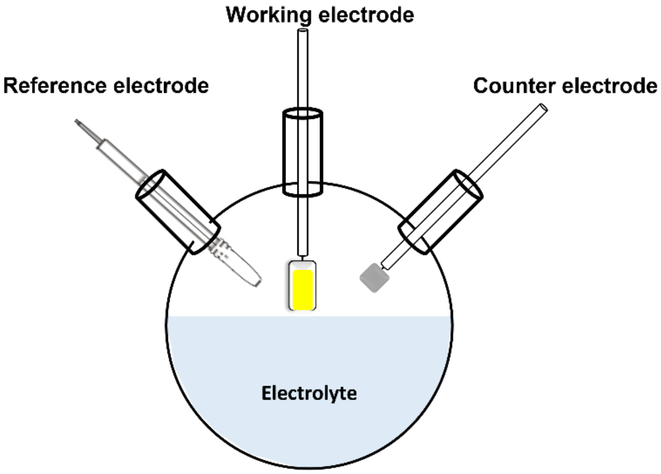

**Figure 2.7 Schematic illustration of the three-electrode configuration cell**

### 2.4.1 Open circuit potential (OCP)

OCP measurement provides valuable information about the designed photoanode that can indicate the onset potential, photovoltage, recombination rate, and electron lifetime. In a typical procedure, the photoanode is illuminated and the electron/hole pair is generated under open-circuit conditions. With continuous illumination over time, the electrons are accumulated in the bulk, while the holes are transferred and consumed with the hole-scavenger species in the electrolyte. The accumulation of electrons generates an induced electron field, which is opposite to the space charge region field. This results in a changing of the measured field-free potential (i.e., OCP) into a more cathodic potential. The measured OCP reflects the Fermi level position of the PEC device. As the OCP potential becomes stable under light, this value is considered the onset light potential of the PEC device. When the light is off, the potential starts to decline as the photogenerated electrons recombine with the oxidized species in the electrolyte. The difference between the potential under light and dark is the photovoltage, which is the amount of voltage the PEC device can produce. The expected result from this measurement is shown in Figure 2.8. Moreover, the potential decay represents the recombination rate, and the electron lifetime can be calculated using the following equation:

$$\tau = \frac{-k_b T}{e}\ x\ \left(\frac{dv_{oc}}{dt}\right)^{-1}\ (Equation\ 2.10)$$

**where** **$\tau$ is the photoelectron lifetime**
**$k_B$ is Boltzmann's constant = $1.381 \times 10^{-23}$ J K$^{-1}$**
**T is the temperature in K, $e = -1.602 \times 10^{-19}$ C**
**$\frac{dv_{oc}}{dt}$ is the first derivative of the open-circuit voltage with respect to time.**

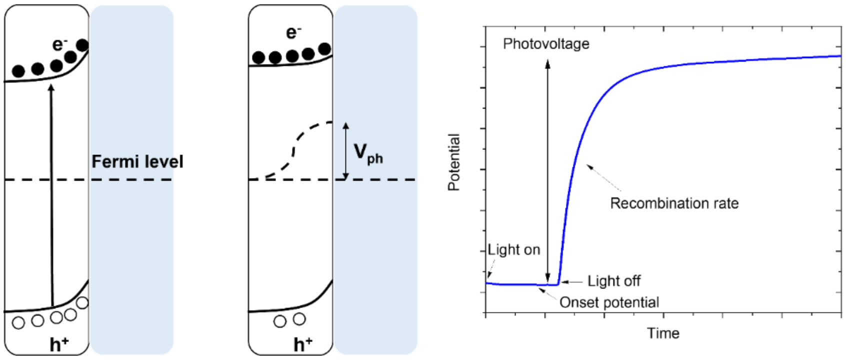

**Figure 2.8 OPC measurement results and the obtained characteristics**

### 2.4.2 Linear sweep voltammetry (LSV)

LSV (j-V analysis) is used to evaluate the photoanode properties and measure the generated photocurrent density with respect to the potential of the reference electrode. From this measurement, the onset potential used for the generation of photocurrent and the maximum photocurrent density produced are obtained. The experiment is carried out from a slight forward bias to a reverse bias potential. As the reverse bias increases, the electric field in the space charge region is increased, which leads to more charge separation and transportation that results in enhancing the photocurrent. To determine the scanning range, the start and end potential were identified first. The starting potential value is slightly higher than the onset potential obtained from the OCP measurement. While the final potential is the dark onset potential, which generates a current with high reverse bias that is capable of water splitting under dark conditions. The experiment is carried out under several conditions (i.e., light, dark, and chopped) as shown in Figure 2.9.

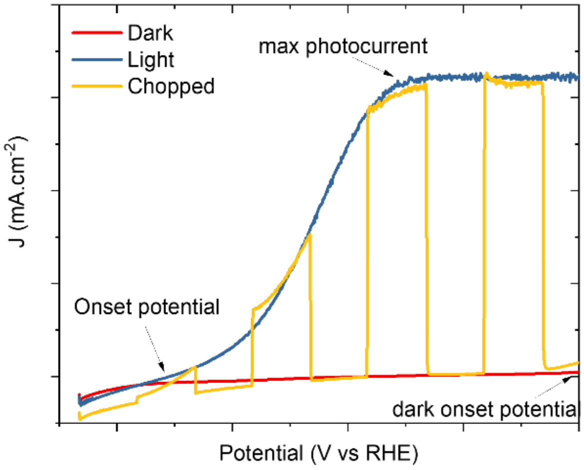

**Figure 2.9 LSV results from light, dark, and chopped conditions**

### 2.4.3 Stability test

The stability of the photocurrent generation is examined over both short and long periods. A constant potential is applied, usually the one with the highest obtained photocurrent density. Then the photocurrent was measured with respect to time under continuous or chopped illumination.

### 2.4.4 The incident photon-to-current efficiency (IPCE)

The wavelength-dependent IPCE values were calculated from the j-V measurement of PEC devices based on different photoanodes. The measurement was carried out by using optical filters of different wavelengths placed in front of the sun simulator to obtain monochromatic light. The light intensity was measured for each optical filter using a power meter. Then the LSV experiment was performed, under light conditions, to determine the photocurrent density. The equation used for the IPCE calculations is as follows:

$$\boldsymbol{IPCE = \frac{1240\ x\ j}{\lambda\ x\ I}}\ (\boldsymbol{Equation\ 2.11})$$

**Where *j* represents the photocurrent density (mA cm$^{-2}$)**
**λ is the wavelength of the incident light (nm)**
**I is the incident light intensity (mW cm$^{-2}$).**

### 2.4.5 Electrochemical impedance spectroscopy (EIS)

EIS is a powerful tool to investigate carrier dynamics due to its sensitivity to electron diffusion and recombination at the interfaces. The charge transport, represent the trapping inside the photoanode, and the charge transfer at the photoanode/electrolyte interface can be extracted from EIS measurements. The experiment was performed by applying an AC bias potential (10 mV) over a range of frequencies (300 kHz to 10 mHz) and measuring the response of the photoanode [125]. The DC potential used is that with the maximum photocurrent density obtained from the LSV measurement. All measurements are carried out in dark condition. For further analysis of the results, an equivalent electronic circuit model used to stimulate the photoanode response and for data fitting [126, 127].

The equivalent circuit of the photoanode is represented in Figure 2.10. The key parameters of the equivalent circuit are:

- $R_s$ is the FTO sheet resistance
- $R_{sc}$ is the charge transport resistance inside the photoanode
- $CPE_{sc}$ is the space charge constant phase element
- $R_{ct}$ is the charge transport resistance at the photoanode/electrolyte interface
- $CPE_H$ is the Helmholtz constant phase element
- Warburg diffusion ($W_s$) might be used at the photoanode/electrolyte interface to detect the diffusion behavior at the interface [128, 129].

The constant phase element (CPE) is used to represent the non-ideal behavior of the space charge and Helmholtz capacitance ($C_{sc}$ and $C_H$). This occurs due to the high surface area feature of the nanostructured material used in each chapter [130]. The CPE can be converted into C by the following equation.

$$\boldsymbol{C_i = \frac{(R_i Q_i)^{\frac{1}{n}}}{R_i}} \ (\boldsymbol{Equation\ 2.12})$$

**Where R is the resistance of charge transport or transfer**
**Q is the CPE of each capacitor**
**n is the similarity index between the CPE and C.**

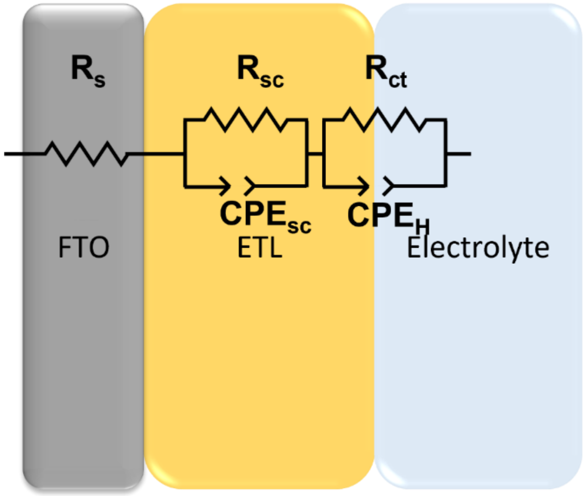

**Figure 2.10 Electronic circuit model for the EIS measurements**

The Nyquist plot is used to represent the data. Two semicircles are obtained; the one at high frequency determines the charge transport inside the photoanode, while the one at low frequency characterizes the charge transfer at the photoanode/electrolyte interface.

Mott–Schottky (M-S) plot is another EIS technique used to identify the flat band potential, which is nearly equivalent to the C.B. of the photoanode. The $C_{sc}$ is measured as a function of applied potential (-1 to 1 V vs Ag/AgCl) using a single frequency (10 kHz) under dark condition. The obtained results are plotted as $\frac{1}{C_{sc}^2}$ vs the potential in a straight line. The extrapolation of this line and its intersection with the x-axis is equal to the flat band potential. This method is used to identify the difference in the electronic band structure of different photoanodes.

### 2.4.6 Gas chromatography (GC) measurements

The actual $H_2$ generation that occurs during the PEC measurement can be analyzed by using the GC measurement. In a typical procedure, the electrochemical setup is identical to the one used for all PEC measurements. The test was conducted under one sun continuous illumination using the same sun simulator with AM 1.5 filter. In addition to that, a sealant was applied to isolate the system from the surrounding atmosphere. Then high purity $N_2$ (Praxair, 99.999%) was bubbled through the electrolyte with a flow rate of 20 standard cubic centimeters per minute (SCCM).

For the practical quantification of $H_2$, the gas outlet was introduced into a gas-sampling loop of the GC 9790 II. The GC was equipped with a packed HaySep A column and a packed MolSieve 5 A column with argon (Praxair, 99.999%) as the carrier gas. A thermal conductivity detector (TCD) was used to quantify $H_2$.

For the theoretical calculations, the number of moles was calculated according to Faraday's law based on the measured photocurrent.

$$\mathbf{n} = \frac{\mathbf{1}}{\mathbf{n}}\frac{\boldsymbol{Q}}{\boldsymbol{F}} = \frac{\mathbf{1}}{\mathbf{2}}\frac{\boldsymbol{I} \times \boldsymbol{t}}{\boldsymbol{F}} = \frac{\mathbf{1}}{\mathbf{2}\boldsymbol{F}}\int_{\mathbf{0}}^{\boldsymbol{t}} \boldsymbol{Idt}\ \ (\boldsymbol{Equation}\ \mathbf{2.13})$$

**Where n is the number of electrons involved in hydrogen generation (n=2).**
**Q is the quantity of charge in coulomb (C) and equals to I (Current in Amp) × t (time in S).**
**F is the Faraday constant (96484.34 C/mole)**

The Faradic efficiency (FE) represents the practical efficiency of the photogenerated charge carriers contributing to the water splitting (i.e., $H_2$ generation) and can be calculated using the following equation.

$$\mathbf{FE} = \frac{\boldsymbol{nFC_ivP}}{\boldsymbol{IRT}}\ \ (\boldsymbol{Equation}\ \mathbf{2.14})$$

**Where $C_i$: The volume fraction of $H_2$ determined by the GC**
**v: flow rate 20 SCCM ($3.3*10^{-7}$ $m^3$ $s^{-1}$)**
**P: pressure 101300 Pa**
**R: The gas constant 8.314 J $mol^{-1}$ $K^{-1}$**
**T: Temperature 293 K**

# CHAPTER 3: TWO-DIMENSIONAL (2D) FUNCTIONALIZED HEXAGONAL BORON NITRIDE (F-h-BN) FOR QUANTUM DOTS (QDs) PHOTOELECECTROCHEMICAL (PEC) DEVICES

## 3.1 Project plan

$TiO_2$ is considered one of the most common electron transport layer (ETL) used in PEC hydrogen generation [131]. However, in this project, $SnO_2$ was used as the ETL due to its promising characteristics, such as (a) high electron mobility [132], (b) more negative conduction band (C.B.) edge [133], and (c) wider bandgap as compared to $TiO_2$ [134, 135]. The high electron mobility (e.g., 100-200 $cm^2 V^{-1} S^{-1}$) allows for a faster diffusion of the photogenerated charge carriers. Thus, a high probability of these carriers being involved in the redox reaction. While the negative C.B. edge enhance the injection rate from the QDs to the ETL, as the driving force of the injection process depends on the difference between the C.B edge of QDs and ETL. Finally, the wider bandgap (e.g., 3.8 eV) enhances the stability of the PEC device. Where a fewer number of holes is generated upon illumination for a long time. To confirm these assumptions, a comparative study between the $TiO_2$ and $SnO_2$ was performed at the end of this project on the device's performance. This work was published in the Journal of Materials Chemistry A, 8 (39), 20698-20713, 2020.

Furthermore, several strategies were implemented to investigate and enhance the performance of the PEC device and reduce the carrier recombination that occurs inside the designed photoanode. These strategies include:

1. The deposition of 2D F-h-BN nanoflakes at the interface between the $SnO_2$ and QDs to prevent the carrier recombination between the photoinjected electrons in the $SnO_2$ and the oxidized species in the electrolyte (Figure 3.1)
2. Extending the absorption range of the photoanode by changing the QDs sensitization from CdS to CdS/CdSe.
3. The influence of $SnO_2$ photoanode thickness on the PEC device performance.
4. Incorporation of multiwall carbon nanotubes (MWCNT) on the highest stable device to enhance the PEC performance.

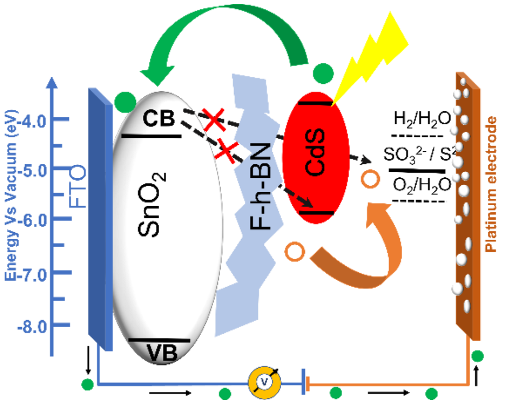

**Figure 3.1** Schematic illustration for the purpose of depositing F-h-BN

## 3.2 Morphological characterization of $SnO_2$

The $SnO_2$ blocking layer was deposited on the FTO by using the spin coating technique. Subsequently, the samples were annealed to produce a compact layer that acts as a barrier for the photogenerated electrons to recombine with the oxidized species in the electrolyte. The SEM was used to investigate the morphology of this layer as shown in Figure 3.2 (a) and (b). The average thickness of this layer was in the range of 500-600 nm, as measured in Figure 3.2 (c). Then a $SnO_2$ film was deposited over the $SnO_2$ blocking layer through the tape-casting method. Different layers (i.e., 1, 2, and 3 layers) were deposited to examine the effect of thickness on the PEC device performance. Likewise, SEM was used to investigate the morphology of the $SnO_2$ film. Figure 3.2 (d) shows that the $SnO_2$ film consists of ~ 60 nm particle size. While Figure 3.2 (e) and (f) indicate that at lower magnification, the film consists of a porous structure that is considered a good template for the QDs deposition to increase the light absorption efficiency. In addition, the proper porosity attains better electrolyte penetration, for faster hole transport and carrier dynamics.

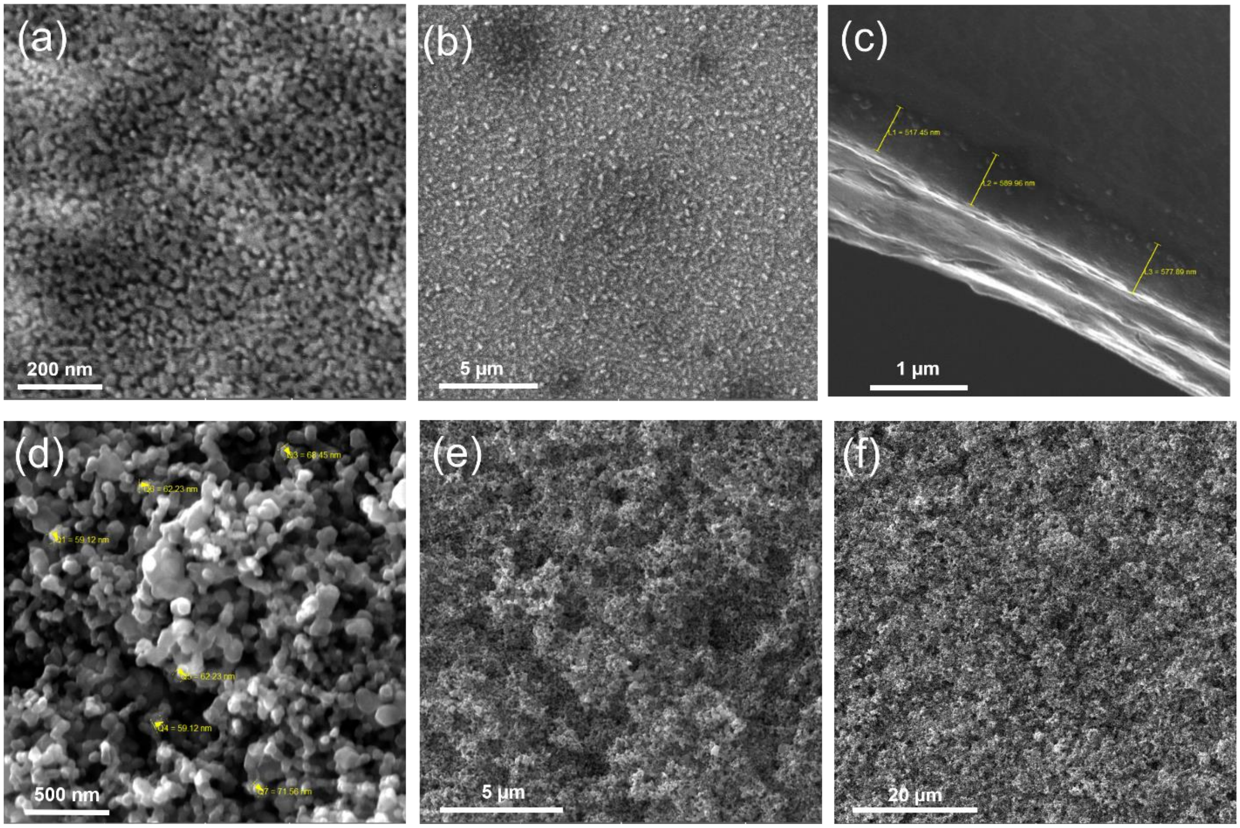

**Figure 3.2 SEM images for the $SnO_2$ blocking layer over the FTO (a) at high magnification, (b) at low magnification, and (c) side view to measure the film thickness. The $SnO_2$ film (d) at lower magnification to measure particle size, (e) and (f) at low magnification to confirm the presence of a porous structure.**

## 3.3 structural and morphological characterization of F-h-BN

The synthesized F-h-BN was characterized by several techniques including TEM, EDS, XRD, FTIR, and AFM. TEM was used to display the structure with high-resolution images. Figure 3.3 (a) and (b) show the stacking of F-h-BN with a deformed hexagonal structure that have an average lateral dimension of 128 and 167 nm. Figure 3.3 (c) shows the elemental analysis conducted by EDS on the F-h-BN nanoflakes, which confirm the presence of B and N, in addition to the S peak from the MSA used for functionalization and Cu from the sample holder. From the atomic resolution image [Figure 3.3 (d)], the lattice spacing was ~ 3.3 Å, which is associated with the (002) hexagonal phase plane of BN (JCPDS file no. 00-034-0421). Two main diffraction peaks were observed in the XRD analysis as shown in figure 3.3 (e). The $26.5^o$ and $55.2^o$ peaks represent the (002) and (004) planes of BN [136], respectively. Finally, the IR peaks at 767, 900, 1730, 2848, and 2920 $cm^{-1}$ were assigned to B-N stretching in-plane, C-H bonding, stretching vibration of C=N and C=O bending of MSA, and O-H groups, respectively [137].

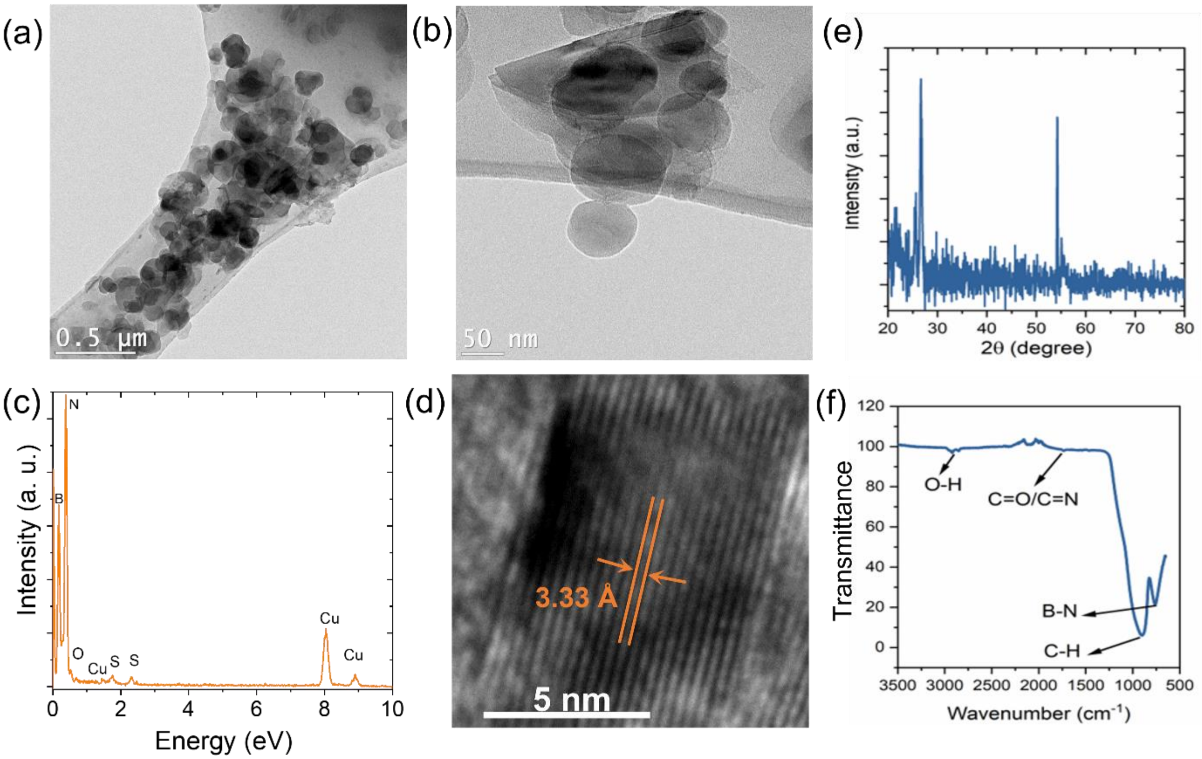

**Figure 3.3 Structural characterization of the F-h-BN nanoflakes: (a) and (b) TEM images showing the stacking density of the 2D F-h-BN nanoflakes; (c) Elemental analysis by EDS and (d) high-resolution TEM showing the atomic resolution and interplanar spacing. (e) XRD patterns. (f) FTIR spectrum**

Additionally, AFM topography images were used to investigate the stacking density of the F-h-BN nanoflakes. In Figures 3.4 (a) to (c), the optical contrast difference is attributed to different stacking layers of F-h-BN. Two profile scans were made [Figure 3.4 (a) and (b)] to provide a 3D model scan and calculate the average thickness of the nanoflakes [Figure 3.4 (c)]. The results show a few-layer stacking of F-h-BN with large molecules of MSA observed on the surface that was used for the functionalization. The detailed calculation of the thickness was obtained from the profile scans in Figure 3.4 (d) and presented in Table 3.1.

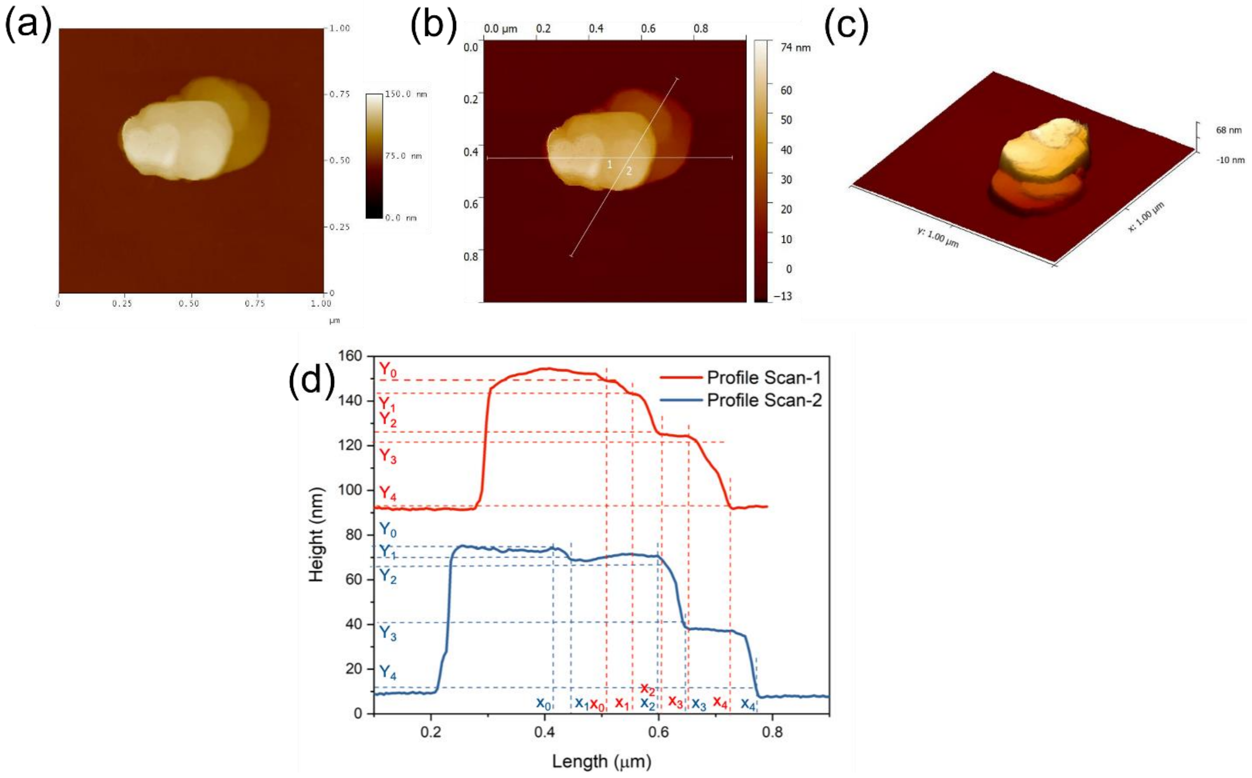

**Figure 3.4 AFM scan of F-h-BN nanoflakes; (a) and (b) topography images (c) 3D scan of the F-h-BN nanoflake (d) Thickness analysis**

**Table 3.1 Calculated thickness of F-h-BN nanoflakes from the AFM scan**

| Profile | Point $X_i$ (μm) (i = 0 - 4) | $Y_j$ (nm) (j = 0 - 4) | Length (nm) | Thickness (nm) |
|---|---|---|---|---|
| Profile-1 | 0.419 | 57.2 | | |
| | 0.465 | 52.3 | 45 | 4.9 |
| | 0.594 | 54.1 | 130 | 1.8 |
| | 0.657 | 21.6 | 63 | 32.6 (3-4 layers) |
| | 0.788 | -8.8 | 131 | 30.3 (3-4 layers) |
| Profile-2 | 0.484 | 53.5 | | |
| | 0.514 | 50.2 | 29 | 3.3 |
| | 0.554 | 44.6 | 41 | 5.6 |
| | 0.606 | 26.6 | 52 | 18.1 (2-3 layers) |
| | 0.739 | -6.3 | 133 | 32.9 (3-4 layers) |

### 3.4 F-h-BN deposition on $SnO_2$ photoanode

To achieve one of the research objectives and reduce the carrier recombination, F-h-BN nanoflakes were spin-coated on the surface of $SnO_2$. To confirm the successful deposition, several characterization techniques were applied. Figure 3.5 (a) shows the FTIR spectrum of the $SnO_2$ film before and after the deposition of F-h-BN. The lattice vibration occurs due to the presence of $SnO_2$ being detected at 770 and 730 $cm^{-1}$ for $SnO_2$ and $SnO_2$/F-h-BN [138]. The IR peaks from the F-h-BN were discussed previously in Figure 3.3 (f). The additional observed peak in the $SnO_2$/F-h-BN spectrum around 2500 $cm^{-1}$ represents the S–H stretching, while the peaks at 1170 and 1045 $cm^{-1}$ correspond to the stretching vibration of S=O groups of MSA. Finally, the wide peak at about 3100-3450 $cm^{-1}$ is related to the vibrations of hydroxide groups or water molecules absorbed at the surface of the samples [139]. From these results, the additional IR peaks in the spectrum of $SnO_2$/F-h-BN verify the existence of F-h-BN on the surface of $SnO_2$ film. Figure 3.5 (b) presents the XRD pattern peaks of $SnO_2$ and $SnO_2$ with F-h-BN. The crystalline structure of $SnO_2$ was confirmed to be tetragonal from the 2Θ angels (26.6°, 33.8°, 37.9°, 51.8°, 54.7°,57.7°, 61.9°, 65.9°, 71.3°, and 78.7°). Those peaks are associated with the planes provided in Figure 3.5 (b) (JCPDS card no. 41-1445). The deposition of F-h-BN led to a slight shift in the 26.6° and 78.7° peaks associated with the (110) and (321) planes, respectively. This shift occurs due to overlapping with the h-BN peak at 26.6° and 76° related to the (002) and (110) planes, respectively [140]. SEM images cannot be used to confirm the presence of F-h-BN nanoflakes in the $SnO_2$ porous film. This is due to the small thickness of F-h-BN and the deposition of a small quantity. However, EDS elemental mapping can be used to detect the B and N distribution inside the sample. Figure 3.5 (c) shows the cross-sectional image of the $SnO_2$/F-h-BN photoanode. While Figure 3.5 (d-f) confirms the presence of the following elements: Sn and O (from $SnO_2$), Si (from FTO), B and N (from F-h-BN). These results confirm the successful deposition of the F-h-BN over the $SnO_2$ film.

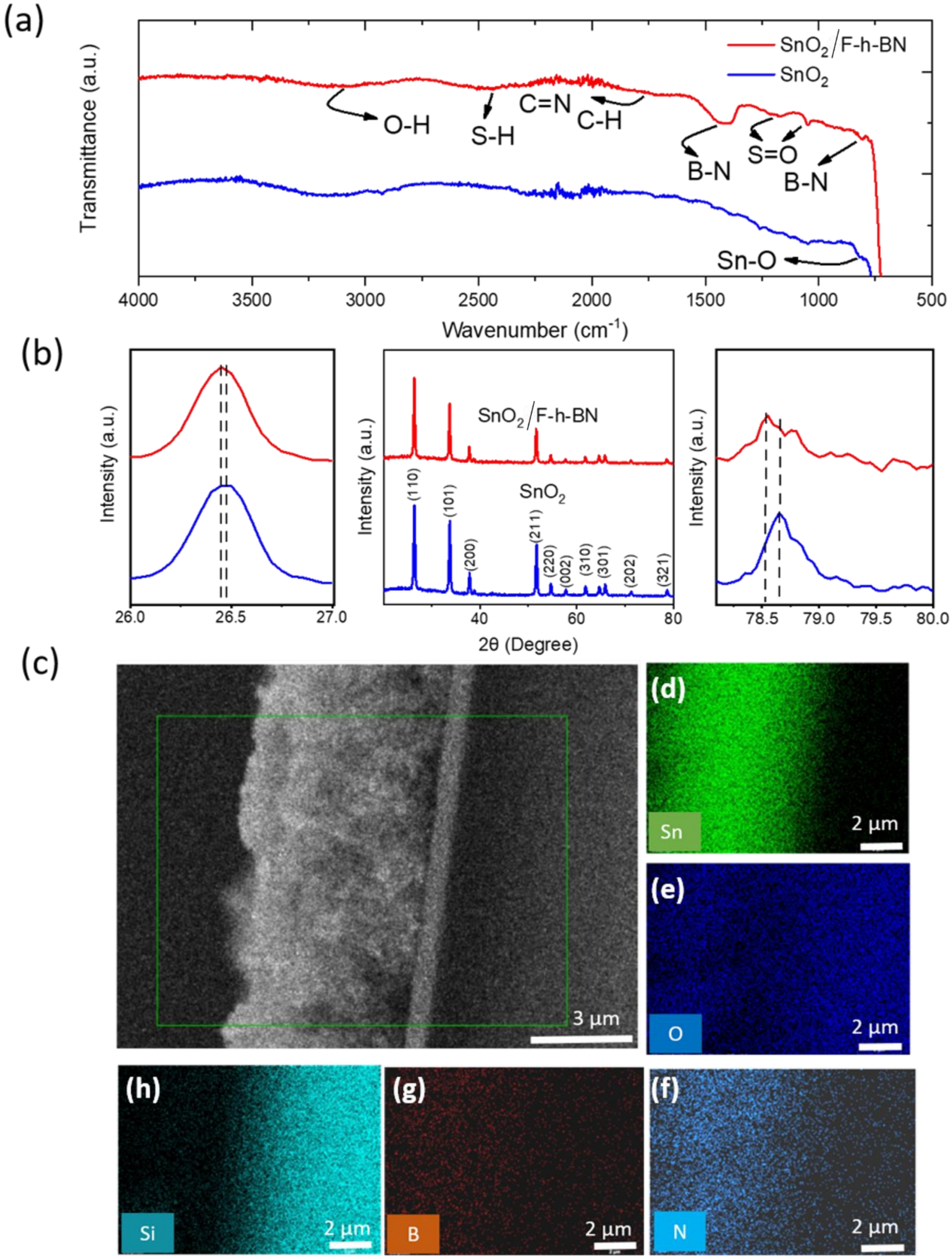

**Figure 3.5 Structural characterization of SnO$_2$ (blue) and SnO$_2$/F-h-BN (red) mesoporous films: (a) FTIR; (b) XRD; (c) EDS elemental mapping of the selected area of SnO$_2$/F-h-BN; (d) Sn; (e) O; (f) N; (g) B; (h) Si.**

Moreover, XPS was performed to confirm the deposition of F-h-BN on the surface of the $SnO_2$ film. Figure 3.6 (a) shows the surface composition and the full spectra of the composite photoanode. The elemental analysis confirms the presence of Sn, O, B, and N on the surface. The high-resolution spectrum of each element is presented in Figures 3.6 (b)-(e). The Sn $3d_{3/2}$ and $3d_{5/2}$ peaks were located at 386.5 and 494.9 eV, respectively [141]. The O1s peak consists of two peaks located at 530.5 and 531.7 eV that represent $O^{-2}$ and $OH^{-1}$, respectively [141]. The B-N bonding is presented in both the B 1s at 190.2 eV and N 1s at 397.8 eV [142, 143]. There are other types of bonding co-exist due to some structural defects including (a) interstitial defect at 399.1 eV in the form of N-N bonding, (b) substitutional defect with a replacement of oxygen as exists at 191.6 eV and 401.3 eV [144]. Finally, in the survey scan, the presence of S 2p and 3s peaks is related to MSA molecules used for functionalization.

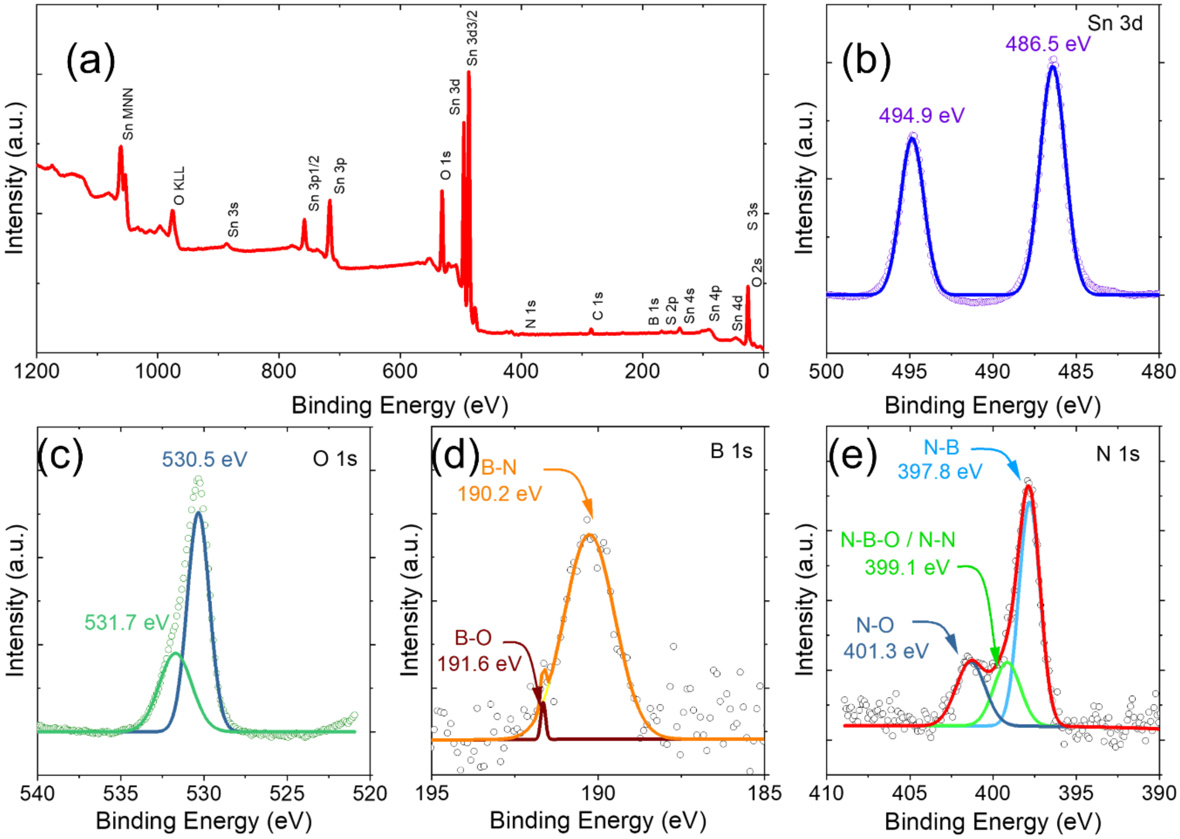

**Figure 3.6 XPS spectra for F-h-BN deposited on $SnO_2$ photoanode: (a) a full survey scan; (b) Sn 3d; (c) O 1s; (d) N 1s; (e) B 1s.**

The optical properties and the electronic band structure of the hybrid structure (i.e., $SnO_2$/F-h-BN) were investigated after the deposition of F-h-BN on the surface of the $SnO_2$ photoanode. The optical bandgap energies were calculated from the UV-Vis absorption spectrum using the Tauc plot. The UV-Vis absorption spectrum is presented in Figure 3.7 (b). The addition of F-h-BN did not affect the absorption spectrum, since the F-h-BN is transparent and has a wide bandgap (5.9 eV) that prevents absorption of photons in the UV-Vis region. However, the calculated bandgap (using equations 2.4, 2.5, and 2.6) shows a slight difference in the optical bandgap, which increases by 0.09 eV with the hybrid structure as compared to the reference $SnO_2$ as shown in Figure 3.7 (a). The positions of the VBM for the two samples were verified by using UPS [Figure 3.7 (d)-(f)]. The valency band offset was detected from the extrapolation of the curve in Figure 3.7 (d) and was 4.04 and 4.06 eV for $SnO_2$ and $SnO_2$/F-h-BN, respectively. Then the work function was calculated from the secondary edge energies as shown in Figure 3.7 (f). The mathematical calculations are illustrated as follows:

- For $SnO_2$, the VBM = 4.04 + (21.22 – 17.12) = 8.14 eV
- For $SnO_2$/F-h-BN, the VBM = 4.06 + (21.22 – 16.74) = 8.54 eV.

To obtain the CBM, the optical bandgap obtained from the UV-Vis was added to the VBM, and the final bandgap position is shown in Figure 3.7 (c).

- For $SnO_2$, the VBM = -8.14 + 3.80 = - 4.34 eV vs Vacuum
- For $SnO_2$/F-h-BN, the VBM = -8.54 + 3.89 = - 4.65 eV vs Vacuum

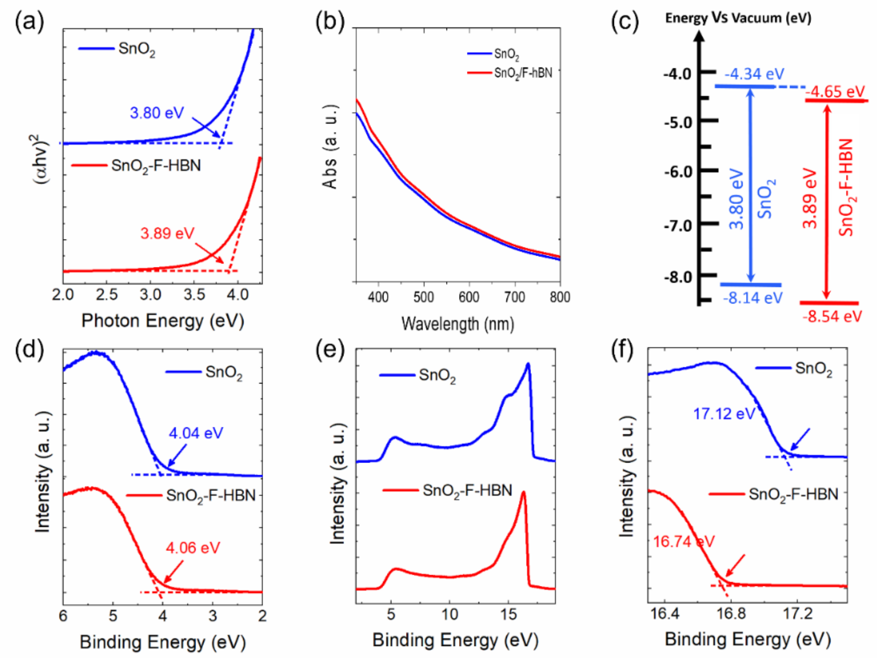

**Figure 3.7 optical and electron properties of $SnO_2$ and $SnO_2$/F-h-BN (a) Tauc plot (b) UV-Vis absorption spectrum (c) electronic bandgap structure (d) valency band offset estimations (e) UPS full spectra (f) secondary edge estimation**

## 3.5 QDs sensitization

Following the deposition of F-h-BN on the surface of $SnO_2$, CdS QDs were sensitized by using the SILAR method to broaden the light-harvesting range and enhance the absorption efficiency. 7 cycles were used for CdS followed by 2 cycles of ZnS for the PEC measurement. Later, the QDs were changed from CdS to CdS/CdSe with 5 cycles of CdS, 3 cycles of CdSe, and 2 cycles of ZnS. EDS, XRD, and XPS were employed to confirm the deposition and the homogenous distribution of the QDs in the hybrid photoanode structure as shown in Figure 3.8.

The cross-sectional image of the photoanode sensitized with CdS/CdSe QDs was analyzed using EDS. The chemical composition was determined through the elemental mapping method [Figure 3.8 (a) – (c)]. The elemental analysis verifies the existence of the following elements in the selected cross-sectional area (green triangle in Figure 3.8 (a)); Sn and O ($SnO_2$ film), Si (FTO), Ti ($TiCl_4$ treatment), Cd, S, Se, and Zn (QDs sensitization). In the mapping images presented in Figure 3.8 (c), the deposition of QDs is confirmed to be homogenously dispersed all over the film thickness of the photoanode. Furthermore, XRD patterns were acquired to confirm the deposition of CdS in the $SnO_2$ film. The peak patterns for the $SnO_2$ and the $SnO_2$/F-h-BN were discussed previously in Figure 3.5 (b). The additional peaks were observed at 44$^o$ which is associated with the (220) plane of CdS [145]. Another two peaks overlapped between the CdS and $SnO_2$ presents at 26.5$^o$ and 52.1$^o$. These XRD peaks correspond to CdS (111) and (311) planes, respectively. Finally, XPS was used to identify the surface chemical composition of the photoanode consisting of hybrid $SnO_2$/F-h-BN, treated with $TiCl_4$, and sensitized with CdS QDs. The XPS survey scan spectrum is presented in Figure 3.8(e) and shows all the elements included in the designed photoanode (i.e., Sn, O, B, N, Ti, Cd, S). The high-resolution peaks are previously presented in Figure 3.6 (b) – (e), while Cd, S, and Ti are presented in Figure 3.8 (f) – (h). The Cd $3d_{3/2}$ and Cd $3d_{5/2}$ peaks are located at 404.8 and 411.5 eV, respectively [Figure 3.8 (f)]. The S peak was characterized by two peaks $2p_{3/2}$ and S $2p_{1/2}$ with energies of 161.2 and 162.1 eV, respectively [Figure 3.8 (g)]. The Ti $2p_{3/2}$ and Ti $2p_{1/2}$ are presented at 458.6 and 464.1 eV, respectively [Figure 3.8 (h)]. From these results, the SILAR method was confirmed to homogenously deposit the QDs inside the photoanode.

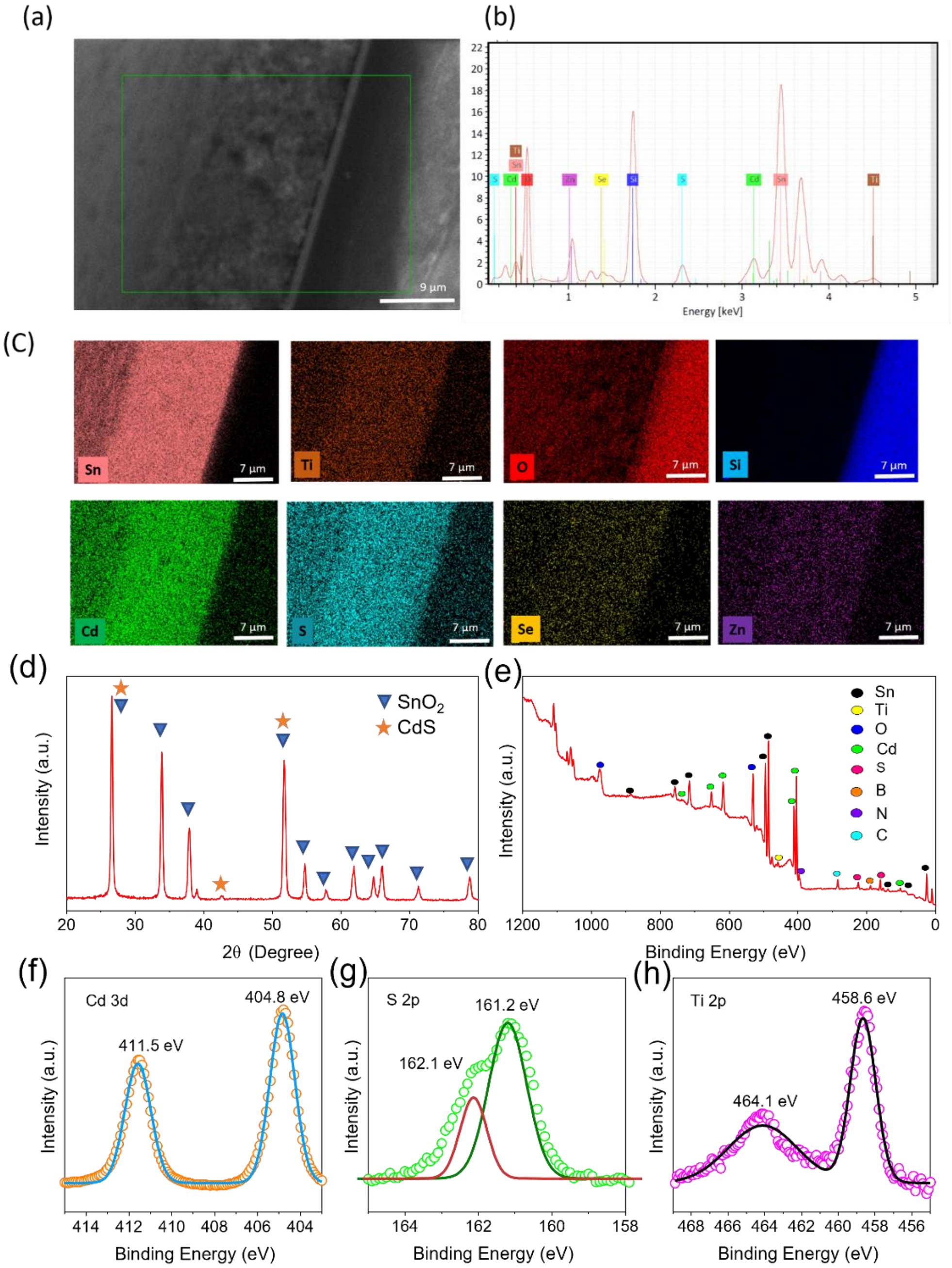

**Figure 3.8 EDS: (a) cross-sectional SEM image of the photoanode; (b) elemental analysis; (c) elemental mapping of Sn, O, Si, Ti, Cd, S, Se, and Zn. (d) XRD patterns. XPS spectra: (e) survey scan; (f) Cd 3d; (g) S 2p; (h) Ti 2p.**

Due to the difference in the electronic band structure of the $SnO_2$ and $SnO_2$/F-h-BN, the carrier injection process from the QDs to the ETL is expected to be different from the $SnO_2$/F-h-BN structure and the reference one. TRPL was used to measure the electron lifetime and the electron transfer rate, which can reflect the charge injection process in each photoanode. In this experiment, colloidal CdSe QDs with 3 nm particle size were deposited through electrophoretic deposition (EPD) rather than the SILAR process. This choice for the colloidal QDs was made due to the experimental condition that utilizes a laser with a specific wavelength (444 nm) and to eliminate any variation in particle size or quantity by using the direct deposition process (i.e., SILAR method). $ZrO_2$ photoanode sensitize with the same QDs was used as a reference sample. The $ZrO_2$ film was deposited on FTO using the same tape casting method used to deposit $SnO_2$. In a typical procedure, the QDs are illuminated with a laser. A photogeneration process occurs and creates electron and hole pairs in the CdSe QDs. Subsequently, the electrons have two possibilities; (a) recombine with the holes in the V.B. or (b) injected into the C.B. of the ETL and then recombine with the holes in the QDs V.B. The injection process of the photogenerated electrons depends on the difference in the C.B. between the QDs and the ETL. For an efficient electron transfer process, the band alignment should be appropriate (i.e., the C.B. of QDs should be higher than the C.B. of the metal oxide). In the case of $ZrO_2$, the C.B. is higher as compared to the CdSe QDs, thus the injection process is forbidden [Figure 3.9 (c)]. That is why $ZrO_2$ was used as a reference sample to calculate the electron transfer rate of the $SnO_2$ and $SnO_2$/F-h-BN photoanodes. The PL decay rates demonstrate the injection process occurs in each of the photoanodes. Faster PL decay reflects a higher injection rate and electron transfer process. The PL decay curves of $ZrO_2$ and $SnO_2$/F-h-BN photoanodes are presented in Figure 3.9 (a). The results confirm a successful injection process in the hybrid $SnO_2$/F-h-BN photoanodes as compared to the $ZrO_2$ with a faster PL decay curve. Additionally, the PL decay rate of the hybrid $SnO_2$/F-h-BN photoanodes is higher compared to the $SnO_2$. In both cases, a successful injection process occurs. However, since the CBM of the hybrid photoanode is lower than the $SnO_2$, then the injection process is faster. The average electron lifetime was calculated using equation 2.7 and the $\tau$ of the $SnO_2$/F-h-BN photoanode is $13.0 \pm 0.8$ ns whereas the $\tau$ of the $SnO_2$ is $52.0 \pm 0.35$ ns. The lifetime difference is attributed to the electronic band structure and the passivation behavior of the F-h-BN to the surface traps that act as recombination sites and hinder the injection process. In addition, the electron transfer rate is calculated using equation 2.8. The $k_{et}$ was $5.5 \pm 0.2 \times 10^{7}$ $S^{-1}$ and $0.3 \pm 0.04 \times 10^{7}$ $S^{-1}$ for $SnO_2$/F-h-BN and $SnO_2$ photoanodes, respectively. These data confirm that the deposition of F-h-BN enhances the charge injection efficiency and improves the electron transfer process.

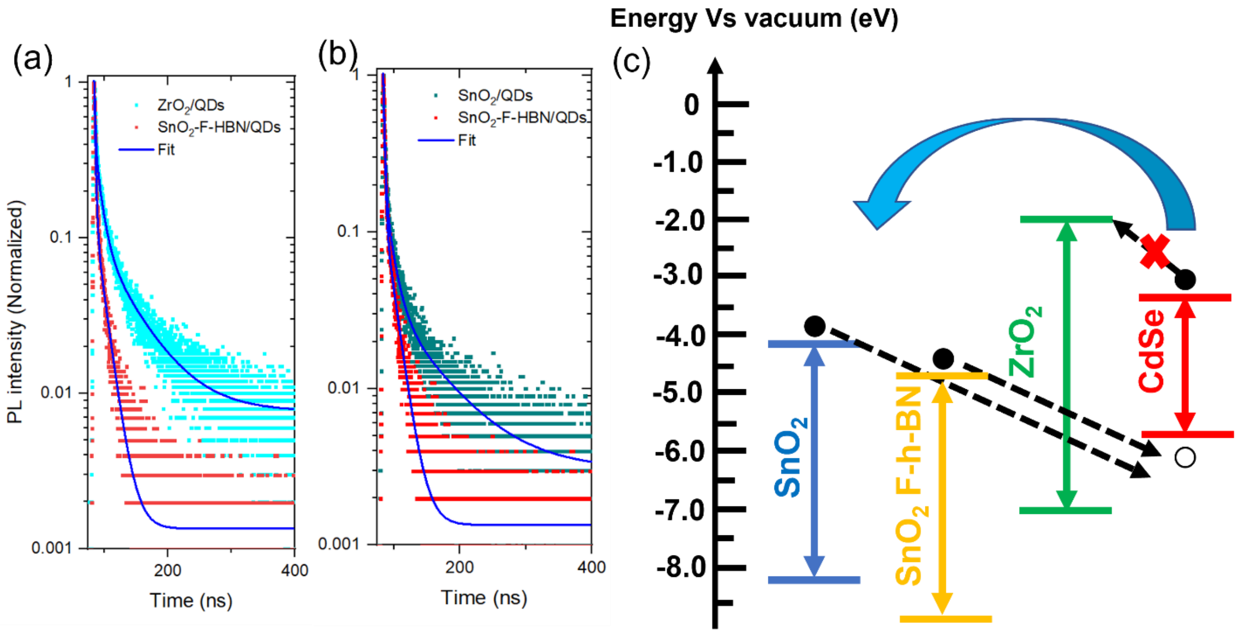

**Figure 3.9 Carrier dynamics of $SnO_2$ and $SnO_2$ with F-h-BN. (a) PL of ZrO2 and $SnO_2$/F-h-BN, (b) PL of $SnO_2$ and $SnO_2$/F-h-BN (c) illustration of the electronic bandgap structure and the injection process**

### 3.6 PEC performance

The PEC device performance was studied with respect to different aspects including (a) the influence of adding different quantities of F-h-BN nanoflakes, (b) the effect of changing the QDs from CdS to CdS/CdSe, (c) the impact of $SnO_2$ layers thickness, and (d) the incorporation effect of MWCNT on the photocurrent density and stability of the PEC devices.

All the LSV measurements were carried out under dark, continuous light, and chopped illumination conditions. The sun simulator was adjusted at 100 mW.cm$^{-2}$ with AM 1.5 filter to simulate the solar spectrum. In the first optimization step, the photocurrent density vs potential was measured for the PEC device based on two layers of $SnO_2$ (with a thickness of ~7 μm) sensitized with 7 cycles of CdS and 2 cycles of ZnS as shown in Figure 3.10 (a). The saturated photocurrent density of the reference device, without F-h-BN, was 2.54 mA cm$^{-2}$ at 1 V vs RHE. Then the spin-coated F-h-BN quantities were varied to find the optimum concentration for the PEC device. The quantity of F-h-BN solutions was altered with 50, 100, and 200 μl, and the obtained saturated photocurrent was 2.88, 4.02, and 3.63 mA cm$^{-2}$ at 1 V vs RHE, respectively [Figure 3.10 (b) – (d)]. The results show that the ideal concentration is 100 μl with a 60% improvement as compared to the reference device without F-h-BN. This improvement was made due to the unique characteristics of the F-h-BN nanoflakes. The energy barrier formed in-between the $SnO_2$ film and the CdS QDs prevent the recombination of the photoinjected electrons with the oxidized species in the electrolyte. Additionally, the shift in the electronic band structure improves the injection rate and enhances the electron transfer efficiency inside the photoanode, which results in higher saturated photocurrent density. Finally, the nanoflakes act as a passivation layer to the $SnO_2$ film that reduces the surface trap sites that eventually contribute to the recombination process inside the photoanode. On the other hand, an increase in the stacking of F-h-BN nanoflakes (i.e., 200 µl) reduces the injection rate of the photogenerated electrons from the QDs to the $SnO_2$ film, since the tunneling effect is inversely proportional to the F-h-BN thickness layer. The OCP measurement and the calculated electron lifetime of the reference device and the optimized one (i.e., with 100 µl of F-h-BN) are presented in Figure 3.10 (e) and (f), respectively. In the OCP measurement, the light was turned on for 30 s then off for 270 s. The measured potential decay was used to calculate the electron lifetime. As shown in Figure 3.10 (f), at any given potential, the lifetime of $SnO_2$/F-h-BN is considerably higher than the reference device. From these results, the F-h-BN nanoflakes confirm the reduction in the recombination rate and improve the photogenerated electron lifetime.

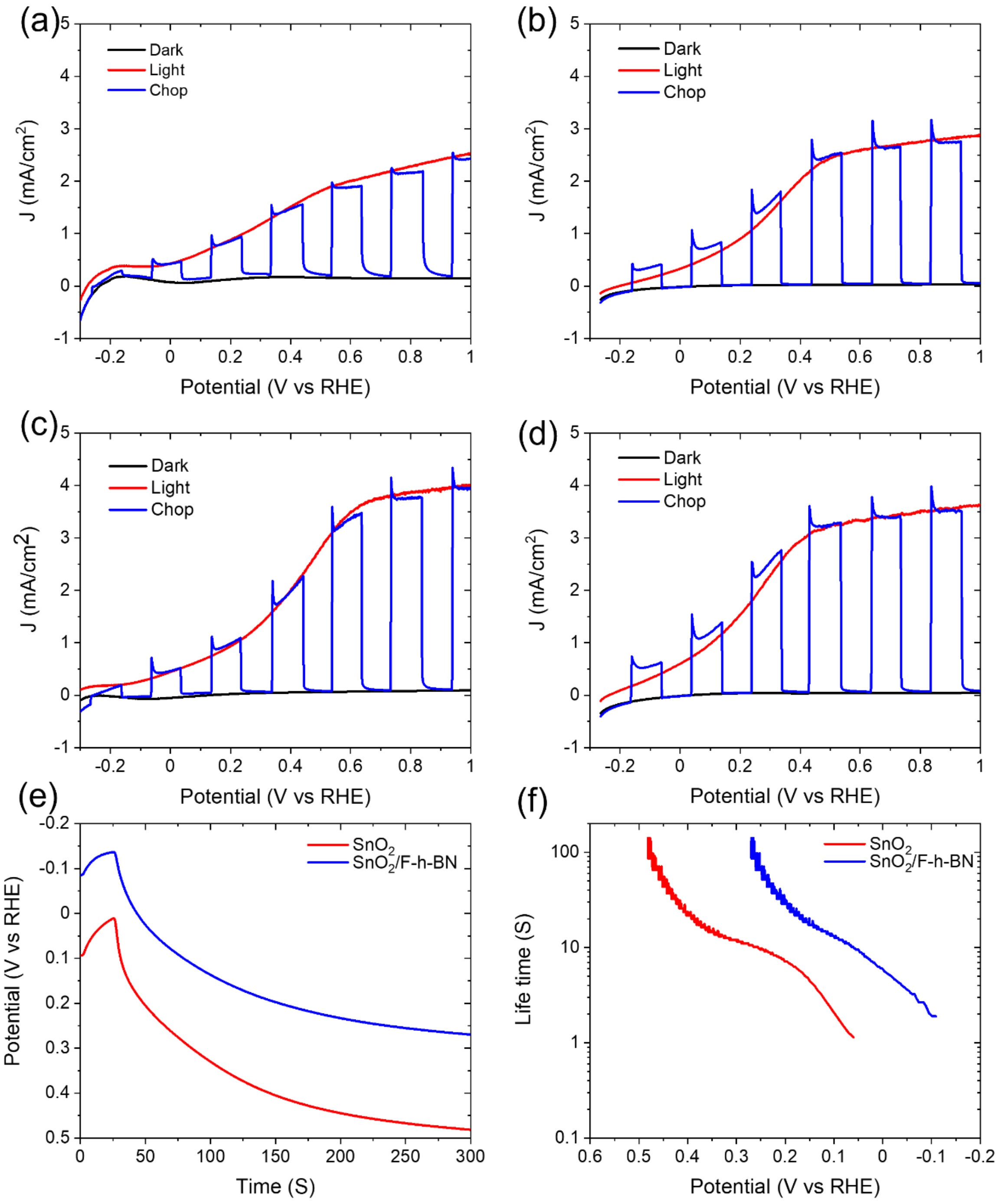

**Figure 3.10 PEC performance under dark, light, and chop conditions for the two-layered $SnO_2$/CdS/ZnS photoanode: (a) without F-h-BN; with (c) 50 μl, (d) 100 μl, (e) 200 μl F-h-BN, respectively. (e) OCP measurement of PEC devices based on the reference photoanode $SnO_2$/F-h-BN/CdS/ZnS photoanodes (e) Electron lifetime calculated from OCP decay.**

Secondly, the saturated photocurrent density and stability were examined by changing the sensitizer QDs from CdS to CdS/CdSe. The purpose is to broaden the light absorption range and enhance absorption efficiency. Two layers of $SnO_2$ film were used and sensitized with 5 cycles of CdS, then 3 cycles of CdSe, and finally 2 cycles of ZnS. LSV, stability, and OCP measurement were performed on the PEC device based on the designed photoanode with and without F-h-BN. Figure 3.11 (a) and (b) show the LSV results for the reference device and the device with the additional F-h-BN, respectively. The saturated photocurrent density of the $SnO_2$/F-h-BN/CdS/CdSe was 6.05 mA cm$^{-2}$, which is 12% higher than the reference device (5.4 mA cm$^{-2}$) at 1 V vs RHE. The stability test was conducted under continuous illumination for 4 h. The measured photocurrent density vs time is presented in Figure 3.11 (c). The F-h-BN significantly enhances the stability with an increase of 13.5% to maintain the initial photocurrent density as compared to the reference device. The percentage change from the initial photocurrent densities, after 4 h of continuous illumination, was 87% and 73.5% for the $SnO_2$/F-h-BN and the $SnO_2$ devices, respectively. Finally, the OCP decay measurement and the calculated electron lifetime are presented in Figure 3.11 (d) and (e). These results reinforce and confirm that the device based on F-h-BN reduces the effect of the recombination process as compared to the reference device.

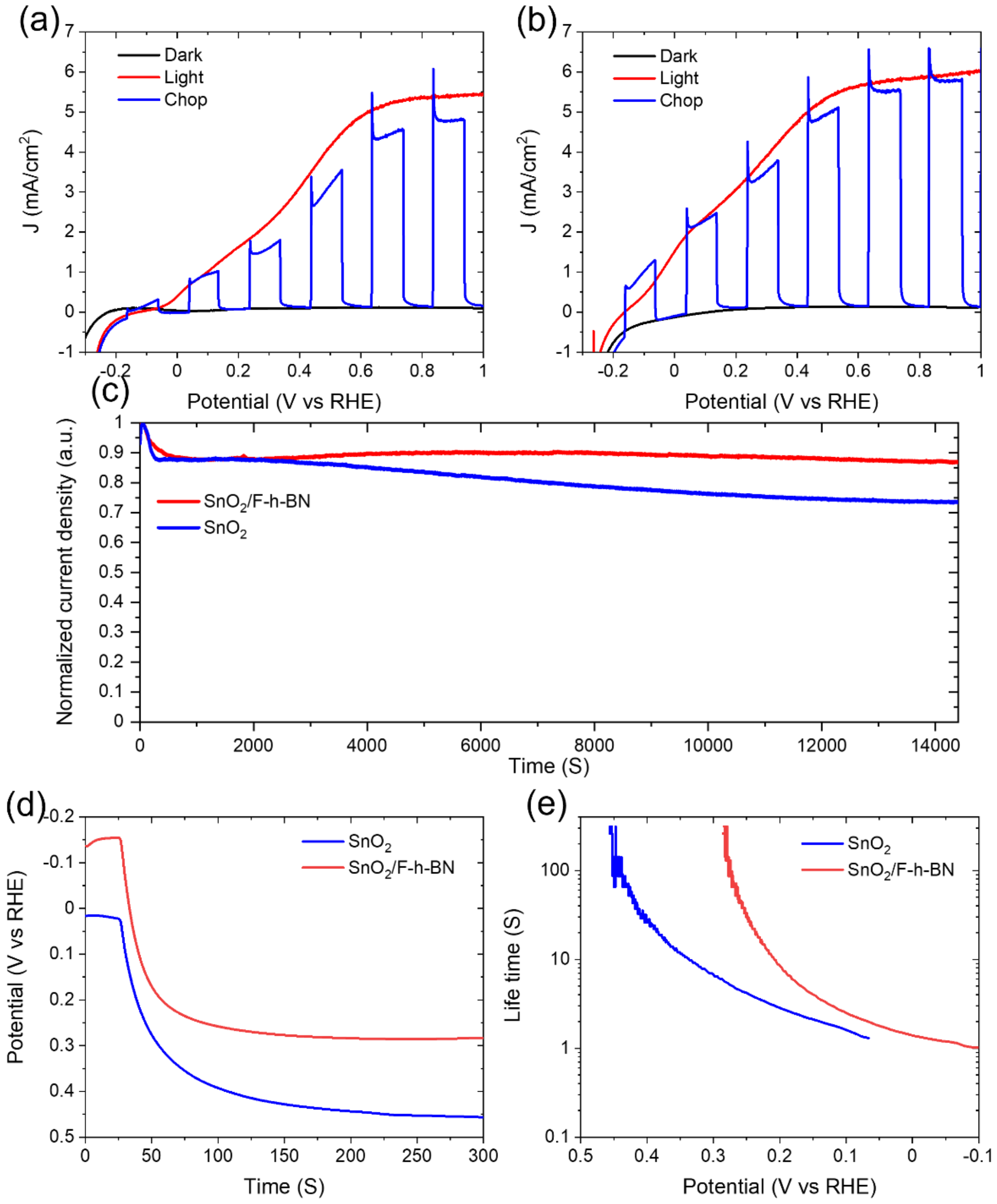

**Figure 3.11 PEC performance under dark, light, and chopped for the two-layered $SnO_2$/CdS-CdSe/ZnS photoanode: (a) without (b) with F-h-BN. (c) Stability test for PEC devices based on SnO2 and SnO2 with F-h-BN sensitized with CdS–CdSe QDs. OCP measurement comparison of PEC devices with and without F-h-BN: (d) open-circuit voltage. (e) Electron lifetime.**

The effect of photoanode thickness variation on the PEC device performance was investigated by changing the $SnO_2$ film thickness by depositing different layers. The thickness of the film was measured using a profilometer. One, two, and three layers were used with an average thickness of ~3, ~7, and ~10 μm, respectively. The LSV and stability measurements were conducted on the devices based on different layers of $SnO_2$ with F-h-BN and sensitized with CdS/CdSe QDs. Figure 3.12 (a) – (c) presents the saturated photocurrent densities for one, two, and three layers, respectively. The highest photocurrent density was achieved while using two layers with 6.05 mA $cm^{-2}$, which is higher than three layers (5.7 mA $cm^{-2}$) and one layer (3.6 mA $cm^{-2}$) at 1 V vs RHE. The improvement in the photocurrent density, from one to two layers, is attributed to an increase in QDs deposition, which increases the light-harvesting and hence the performance, as a more active surface area exists with the larger thickness of $SnO_2$. However, a further increase in photoanode thickness increases the path length of the photogenerated carriers to reach the conductive substrate, which leads to an increase in the recombination probability of the carriers contributing to the redox reaction. This effect will decrease the electron lifetime and hence the photocurrent density. The stability of the PEC devices with different $SnO_2$ layers is shown in Figure 3.12 (d). The normalized photocurrent density for three layers shows a significant improvement in the device stability, maintaining 98% of the initial photocurrent density after 4 h, which is 11% higher than two layers. For the device based on one layer, the stability decreases noticeably after just 2 h. The photocorrosion process that reduces the stability of the PEC device depends on the number of photogenerated holes. These holes oxidize the QDs and degrade the stability of the PEC device. An increase in the thickness (i.e., three layers) of the $SnO_2$ film will absorb more UV photons and reduce the QDs degradation rate. In addition, the porosity of the photoanode increases with the thickness increase, which provides a proper electrolyte penetration. The right contact between the photoanode and electrolyte improves the carrier dynamics at the interface. Consequently, the number of accumulated holes at the interface reduces and thus enhances the stability of the PEC device.

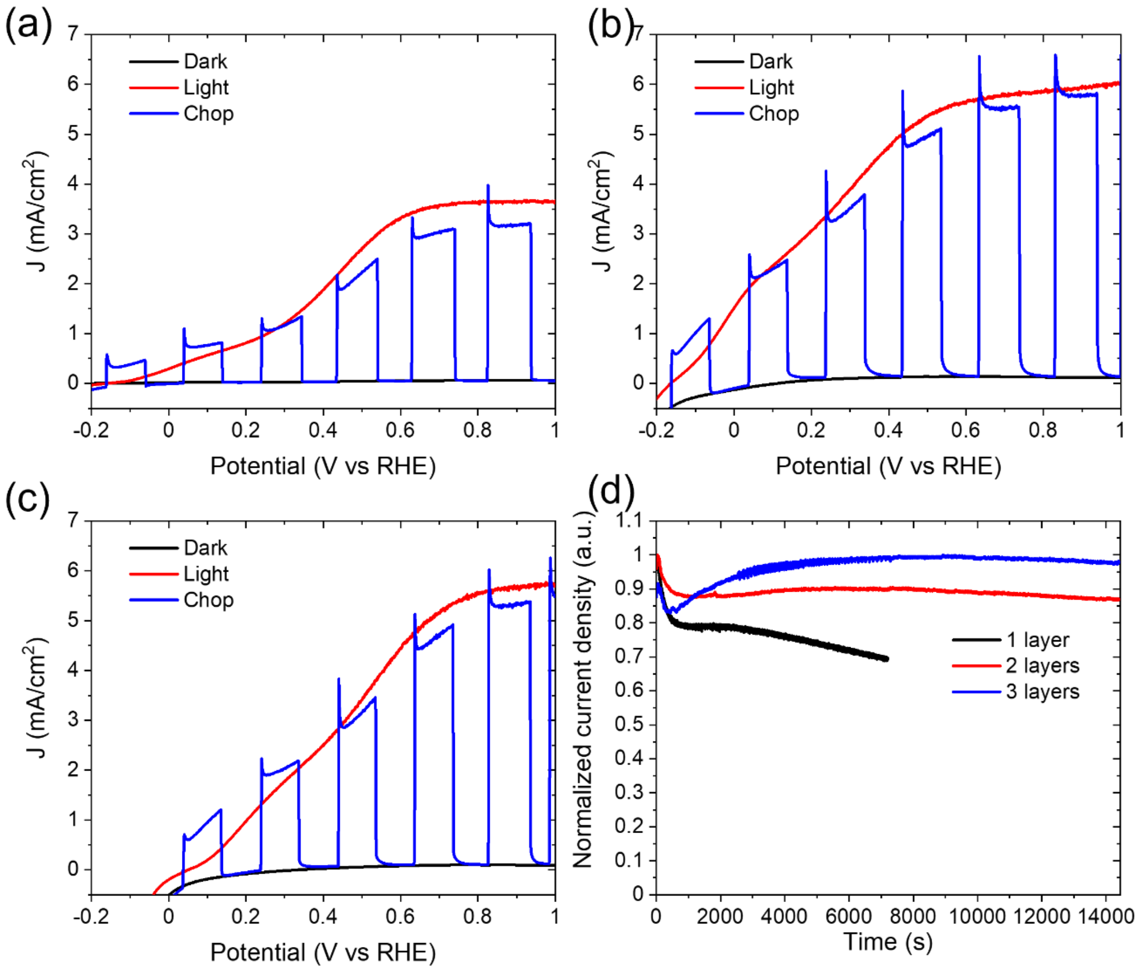

**Figure 3.12 PEC performance under dark, light, and chop for $SnO_2$/F-h-BN/CdS-CdSe/ZnS photoanode with different layers of $SnO_2$: (a) One layer; (b) Two layers; (c) Three layers. (d) Stability performance: Normalized current density vs time (s).**

Finally, MWCNT was incorporated into the three layers of $SnO_2$ film, to take advantage of the high stability and improve the photocurrent density of the PEC device. The mixture was made with manual stirring of 0.015 wt. % of MWNCT with $SnO_2$ paste before the tape casting process. Figure 3.13 (a) and (b) provide the photocurrent density of the device based on three layers of $SnO_2$ with F-h-BN and sensitized with CdS/CdSe QDs with and without MWCNT, respectively. The photocurrent density reaches 6.37 mA $cm^{-2}$ at 1 V vs RHE, which is a 12% increase as compared to the reference device. The improved performance is attributed to enhancing the charge transport properties of the photoanode that provide a directional pathway for the photoinjected electrons. In addition, the electron lifetime calculations show an enhancement with the addition of MWCNT as shown in Figure 3.12 (c) and (d).

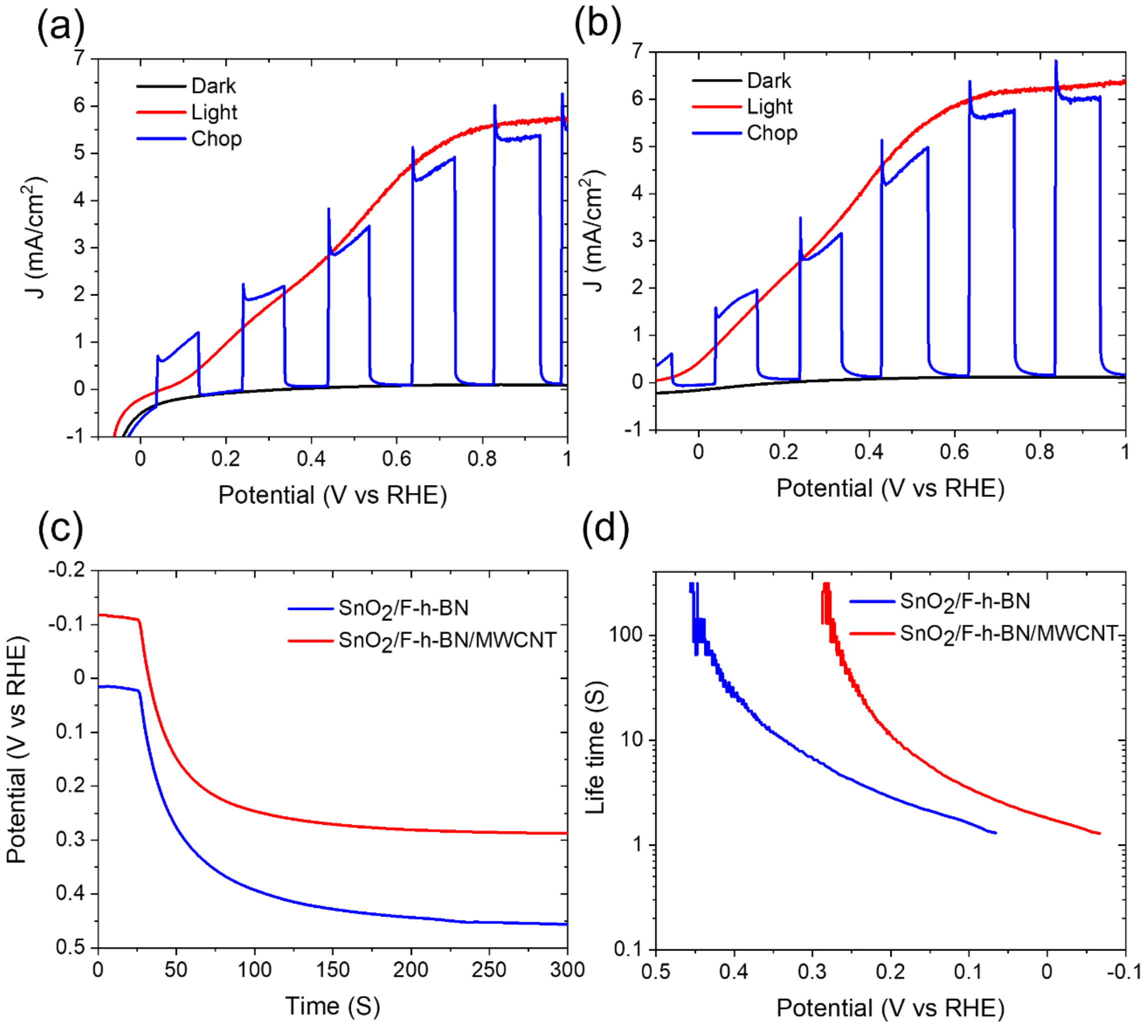

**Figure 3.13 PEC performance under dark, light and chop for three layers $SnO_2$/CdS/CdSe/ZnS photoanode with F-h-BN; (a) without (b) with MWCNTs; (d) Open circuit voltage. (e) Electron lifetime.**

EIS was used to measure the carrier dynamics properties of the PEC device based on $SnO_2$ with and without F-h-BN. The charge transport resistance inside the $SnO_2$ film and charge transfer resistance at the photoanode/electrolyte interface were analyzed, in addition to the space charge and Helmholtz capacitance. The experimental conditions are mentioned in section 2.4.5. The experimental results and the fitted curve using the stimulated electronic circuit are shown in Figure 3.14 (a). The measured data are represented in table 3.2. The results confirm that the addition of F-h-BN nanoflakes enhances the charge transfer resistance and the diffusion resistance at the photoanode/electrolyte interface. This enhancement occurs due to the presence of an energy barrier formed from the deposition of F-h-BN materials and reduces the electron transfer from the photoanode to the electrolyte. Moreover, the charge transport resistance inside the photoanode is reduced with the addition of F-h-BN. This result confirms the passivation behavior of the F-h-

BN that can screen the trap sites and reduce the trapping and de-trapping process that occurs inside the $SnO_2$ film. Moreover, the M-S plot was used to identify the onset potential of different PEC devices. From Figure 3.14 (b) and (c), the onset potential shows a slight shift with the addition of F-h-BN in the case of CdS and CdS/CdSe QDs. This shift confirms the difference in the electronic band structure and complements the results from the UPS measurements. Finally, the IPCE measurements for the PEC device based on $SnO_2$/CdS/CdSe with and without F-h-BN are shown in Figure 3.14 (d). The calculations were made with equation 2.11 and the photocurrent density was obtained at 1 V vs RHE. The comparison over a wide range of wavelengths shows that the addition of F-h-BN improves the conversion efficiency, and the results are consistent with all the PEC and EIS measurements.

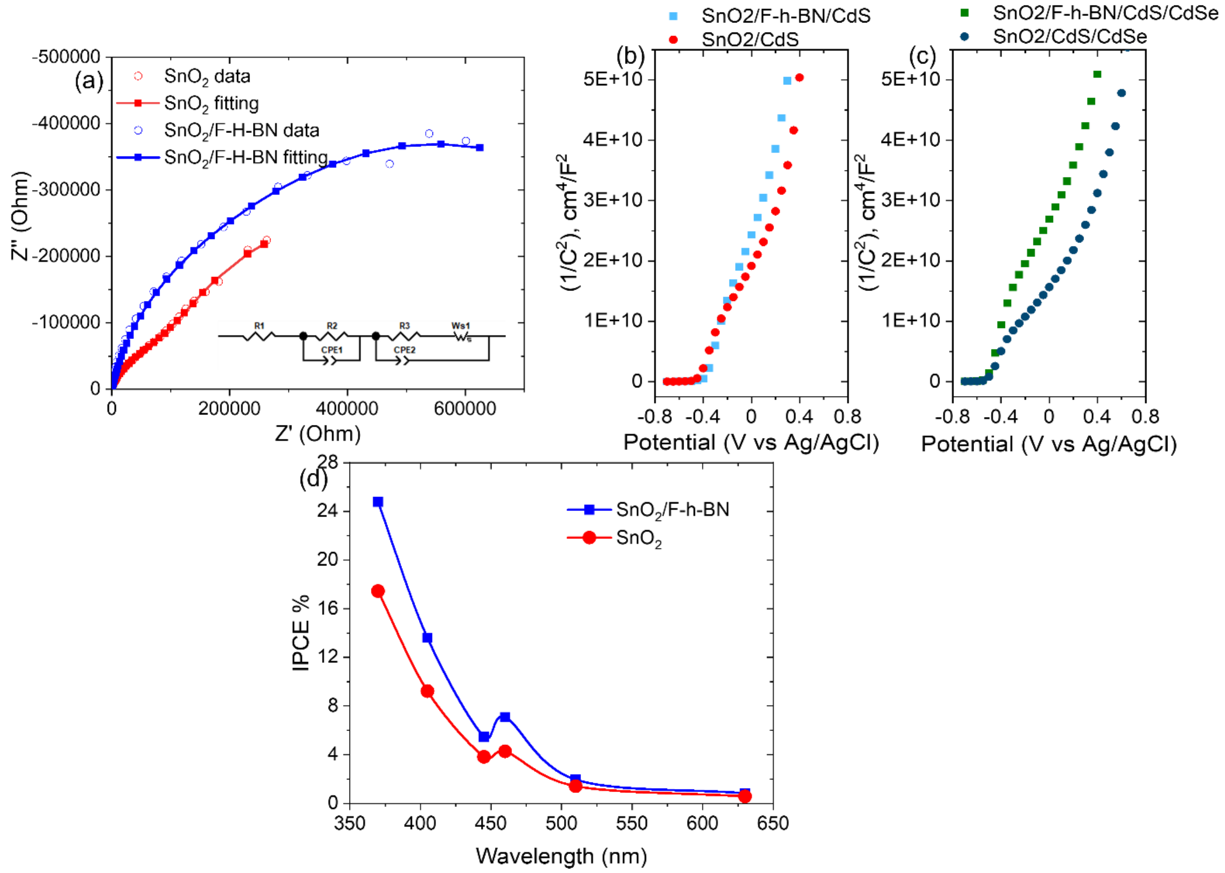

**Figure 3.14 (a) EIS results and the simulated electric circuit used for $SnO_2$ and $SnO_2$/F-h-BN M–S plot for the $SnO_2$ photoanode with and without F-h-BN and sensitized with: (b) CdS QDs; (c) CdS/CdSe QDs. (d) IPCE measurement for PEC device based on $SnO_2$ sensitized with CdS/CdSe QDs with and without F-h-BN.**

**Table 3.2 EIS results for $SnO_2$ and $SnO_2$/F-h-BN**

| Data | $SnO_2$ | $SnO_2$/F-H-BN | Unit |
|---|---|---|---|
| R1 | 15.2 | 12.5 | Ohm |
| R2 | $5.23 \times 10^5$ | $3.00 \times 10^5$ | Ohm |
| R3 | $2.52 \times 10^4$ | $5.40 \times 10^5$ | Ohm |
| C2 | $4.53 \times 10^{-5}$ | $8.19 \times 10^{-6}$ | F |
| C3 | $3.64 \times 10^{-6}$ | $1.75 \times 10^{-5}$ | F |
| Ws1-R | $6.31 \times 10^4$ | $1.42 \times 10^5$ | Ohm |
| Ws1-T | 1.649 | 5.5 | S |
| The constant phase elements used to calculate the capacitance | | | |
| CPE1-T | $3.33 \times 10^{-5}$ | $7.04 \times 10^{-6}$ | Q |
| CPE1-P | 0.90293 | 0.832 | n |
| CPE2-T | $4.03 \times 10^{-6}$ | $1.50 \times 10^{-5}$ | Q |
| CPE2-P | 0.958 | 0.932 | n |

At the end of this chapter, a comparative study on the ETL was made between the $SnO_2$ and $TiO_2$, which is the more common metal oxide semiconductor used for PEC hydrogen generation. The $TiO_2$ photoanode was based on two layers of mixed paste (20-450 nm particle size). The photocurrent density and stability of the devices based on $SnO_2$ and $TiO_2$ sensitized with the same QDs (i.e., CdS/CdSe) with and without F-h-BN are presented in Figure 3.15 (a) and (b). The results confirm that the addition of F-h-BN improves both the saturated photocurrent density and stability as compared to the reference devices. However, the $TiO_2$/F-h-BN shows a higher photocurrent density (8.12 mA $cm^{-2}$) than $SnO_2$/F-h-BN (6.37 mA $cm^{-2}$). On the other hand, the stability of the $TiO_2$/F-h-BN is significantly lower as compared to $SnO_2$/F-h-BN. The reduction in the photocurrent density, in the case of $SnO_2$, is attributed to the increase in carrier recombination between the photoanode and electrolyte. The position of CBM of $SnO_2$ is relatively more negative than the $TiO_2$ and thus its position is near to the redox potential of the electrolyte. The small difference between the C.B. edge of $SnO_2$ and the redox potential led to more recombination between the photoinjected electrons and the oxidized species in the electrolyte. Thus, the photocurrent density is lower in the case of $SnO_2$ as compared to $TiO_2$. On the other hand, the stability of $SnO_2$ is significantly higher than $TiO_2$, since the bandgap of $SnO_2$ is wider (3.8 eV compared to 3.2 eV) and creates less quantity of photogenerated holes that is responsible for the photocorrosion process.

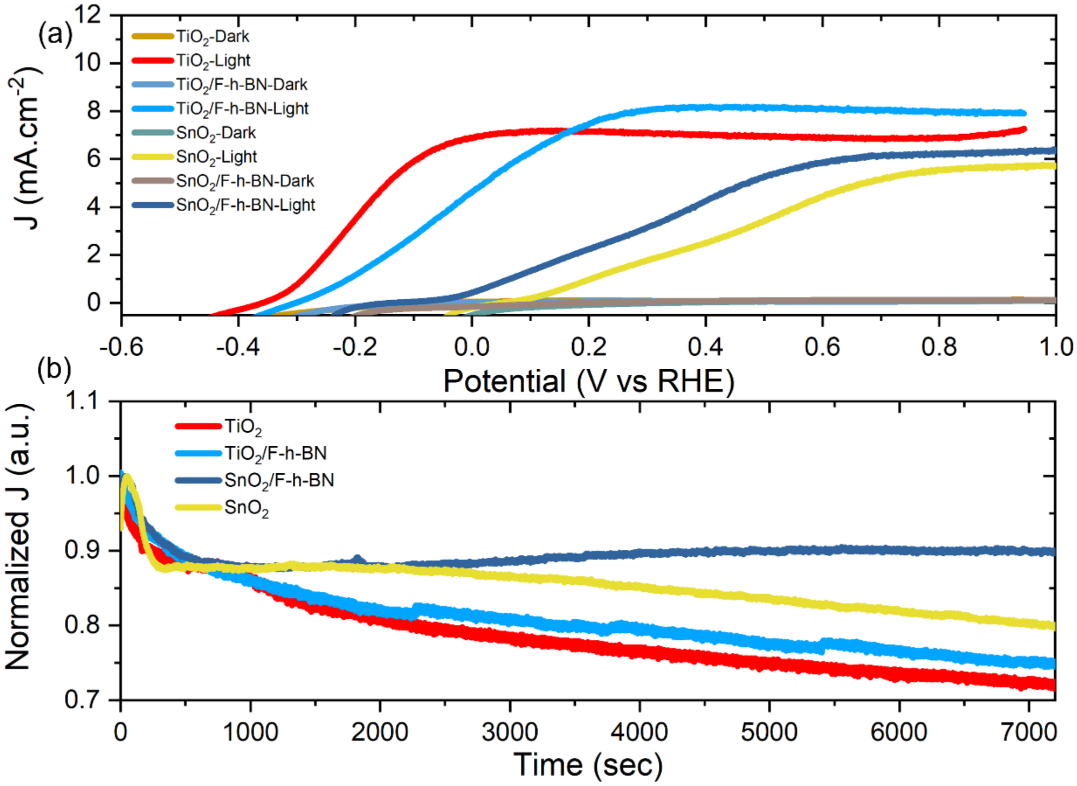

**Figure 3.15 PEC performance comparison between $SnO_2$ and TiO2 sensitized with CdS/CdSe/ZnS with and without F-h-BN photoanode: (a) dark and light performance of the photoanodes. (b) Stability performance of the corresponding PEC devices**

### 3.7 Summary

Briefly, the work in this chapter was about the design of a novel approach to overcome the charge recombination and enhance the PEC device performance. A heterojunction photoanode was fabricated through the incorporation of 2D F-h-BN nanoflakes at the interface between the $SnO_2$ film and QDs. The 2D material was used for passivation of the $SnO_2$ surface, as well as engineering the interface of $SnO_2$/QDs to reduce the charge carrier recombination between the photoanode and oxidized species in the electrolyte. The work proves that the addition of F-h-BN improves the device performance and carrier dynamics by improving the electron injection rate and reducing carrier recombination at the metal oxide/QDs/electrolyte interface. In addition, tailoring the $SnO_2$ film thickness and incorporating MWCNTs were investigated for their effect on carrier dynamics and overall device performance. The work focuses first on the structural analysis of the as designed photoanode. Then a detailed study on the effect of F-h-BN incorporation on the electronic band structure and carrier dynamics. Finally, comprehensive PEC measurements were used to underpin the influence of the design concept on the overall device performance.

# CHAPTER 4: SURFACE ENGINEERING OF HYBRID STRUCTURE PHOTOELECTROCHEMICAL (PEC) DEVICES

## 4.1 Project plan

In this project, $TiO_2$ is used as the electron transport layer (ETL) due to the superior performance obtained in the previous chapter. However, instead of inserting additional low dimensional carbonaceous materials to enhance the transport efficiency (e.g., multiwall carbon nano tubes “MWCNT”, graphene nanoribbons “GNR”, graphene) and reduce the recombination process by adding a passivating material at the surface of the photoanode (e.g., Functionalized hexagonal boron nitride “F-h-BN”), these properties were improved within the ETL layer itself. To simplify the fabrication process, a novel surface engineered hybrid photoanode architecture was designed to improve the charge transport efficiency, the quantum dots (QDs) deposition, and carrier dynamics. The photoanode structure consists of $TiO_2$ nanorods (NRs) combined with $TiO_2$ nanoparticles (NPs). In addition, a surface engineering of the hybrid structure was made through hydrazine treatment to reduce the number of surface traps, and further enhance the performance of the PEC devices. Finally, a theoretical simulation was made by using density function theory (DFT+U) calculations. The simulation describes the mechanism that underpins the significant improvement in the device performance. This work was published in the chemical engineering journal 429, 132425, 2022.

To achieve these objectives, several steps were made including:

1. Optimization of the $TiO_2$ NRs growth duration
2. Adjusting the choice of the $TiO_2$ NPs with different particle sizes.
3. Tuning the concentration of hydrazine treatment

The concept of the photoanode design architecture is shown in Figure 4.1.

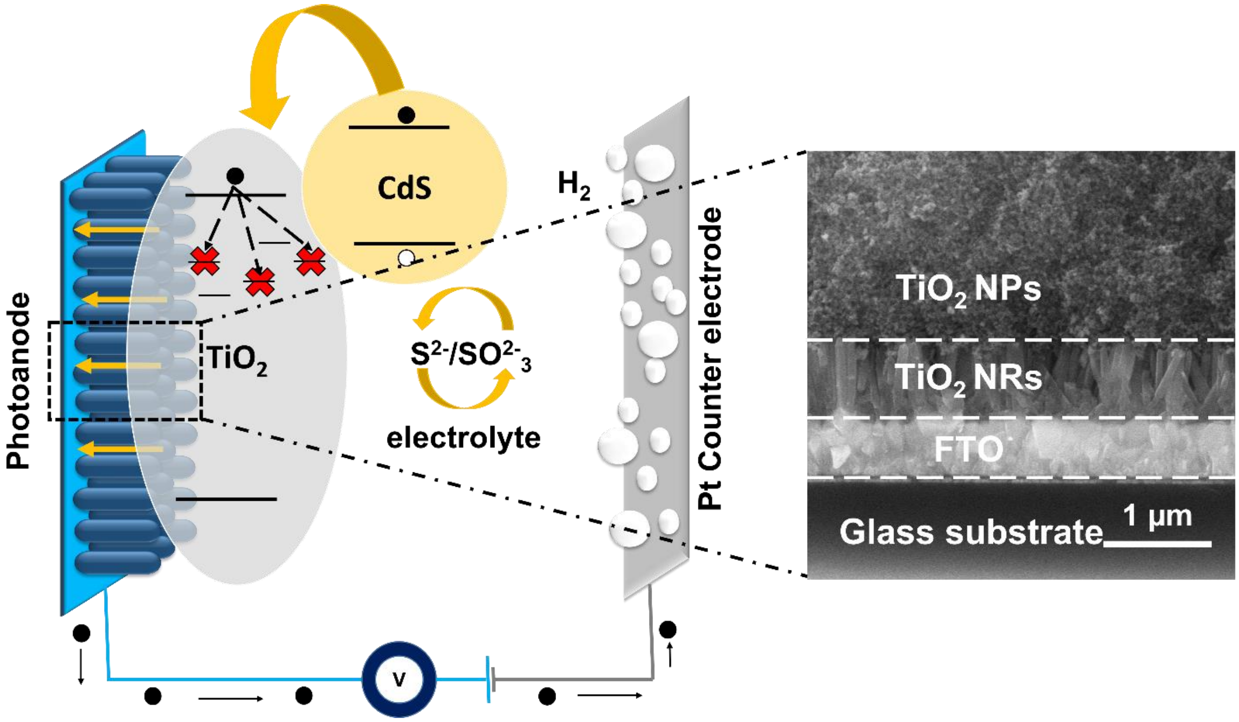

Figure 4.1 Schematic illustration of the photoanode design and SEM image of the actual sample

## 4.2 Growth of $TiO_2$ NRs

$TiO_2$ NRs were grown using the hydrothermal method over FTO coated with $TiO_2$ blocking layer. The $TiO_2$ NRs nucleation and growth depend on several parameters including; (a) growth time, (b) temperature, (c) reactant concentration, and (d) additives used in the mixture [146]. All the parameters were fixed in the hydrothermal process except the growth time. The $TiO_2$ blocking layer provides two important features in the photoanode architecture: (a) prevents the recombination of the photogenerated electrons, with the oxidized species in the electrolyte, after reaching the FTO, and (b) avoids any lattice mismatch between the $TiO_2$ NRs and the FTO substrate. In addition, the $TiO_2$ blocking layer act as a seed layer for the nucleation and growth of the $TiO_2$ NRs. The reaction time varies from 3, 4, and 5 h to investigate the effect of $TiO_2$ NRs length on the PEC device performance. SEM images were used to examine the structure of the $TiO_2$ NRs generated through different growth times. Figure 4.2 (a) – (c) shows the distribution of the $TiO_2$ NRs through a top view with 3, 4, and 5 h, respectively. While the inset images at higher magnification present the morphology of the grown $TiO_2$ NRs. In the case of 3 h [Figure 4.2 (a)], the image shows that incomplete nucleation and growth of the $TiO_2$ NRs were obtained, where insufficient reaction time prevents the homogenous growth and alignments of the $TiO_2$ NRs. In addition, in the inset image, the $TiO_2$ NRs were randomly distributed, and the structure has a circular end with an average diameter of ~41 nm. The average diameter distribution of $TiO_2$ NRs for 3 h growth is presented in Figure 4.2 (d). However, in the case of the 4 and 5 h reaction times, the distribution of the $TiO_2$ NRs was homogenous all over the photoanode. Therefore, sufficient growth time leads to complete nucleation and growth of the $TiO_2$ NRs. From the inset images, the $TiO_2$ NRs show a tubular structure, and the top of the NRs end has a square-like shape. This structure presents the well-crystalline feature of the tetragonal phase of the $TiO_2$ NRs [120]. The $TiO_2$ NRs grown over the FTO were with a diameter of ~79 and ~145 nm for 4 and 5 h, respectively. The $TiO_2$ NRs diameter distribution is presented in Figure 4.1 (e) for 4 h and (f) for 5 h growth time. The surface density of the $TiO_2$ NRs is different in each growth time reaction. It is important to highlight the surface density in $\mu m^{-2}$ as the interface between the $TiO_2$ NRs and NPs considerably affects the performance of the PEC devices. In the case of 3 h, the $TiO_2$ NRs density was difficult to calculate due to the random distribution and orientation of the $TiO_2$ NRs. While for 4 h the surface density was 44 NRs $\mu m^{-2}$ and for 5 h was 24 NRs $\mu m^{-2}$. Cross-sectional SEM images were used to measure the length of different $TiO_2$ NRs growth times. Figure 4.2 (g) – (i) presents the $TiO_2$ NRs thickness for 3, 4, and 5 h, respectively. The average length of the $TiO_2$ NRs is critical as it affects the total photoanode thickness after the deposition of the $TiO_2$ NPs. The average thickness affects the path length of the photogenerated carriers and consequently the PEC device performance. The SEM images show that the average length was 500 nm, 1 μm, and 2 μm for 3, 4, and 5 h reaction times, respectively. These results conclude that there is a linear relationship between the length of the $TiO_2$ NRs and reaction time, where it’s doubled every 1 h. It is worth mentioning that not all $TiO_2$ NRs are grown perpendicular to the surface. Some $TiO_2$ NRs grow off-angle and collide with the neighboring NRs and stop the epitaxial growth. This phenomenon occurs due to the nature of the $TiO_2$ blocking layer seed layer. The blocking layer was deposited on the FTO surface, which has a rough surface, as shown in Figure 4.1. This results in a polycrystalline $TiO_2$ blocking layer surface with high roughness that leads to the misalignment of the $TiO_2$ NRs.

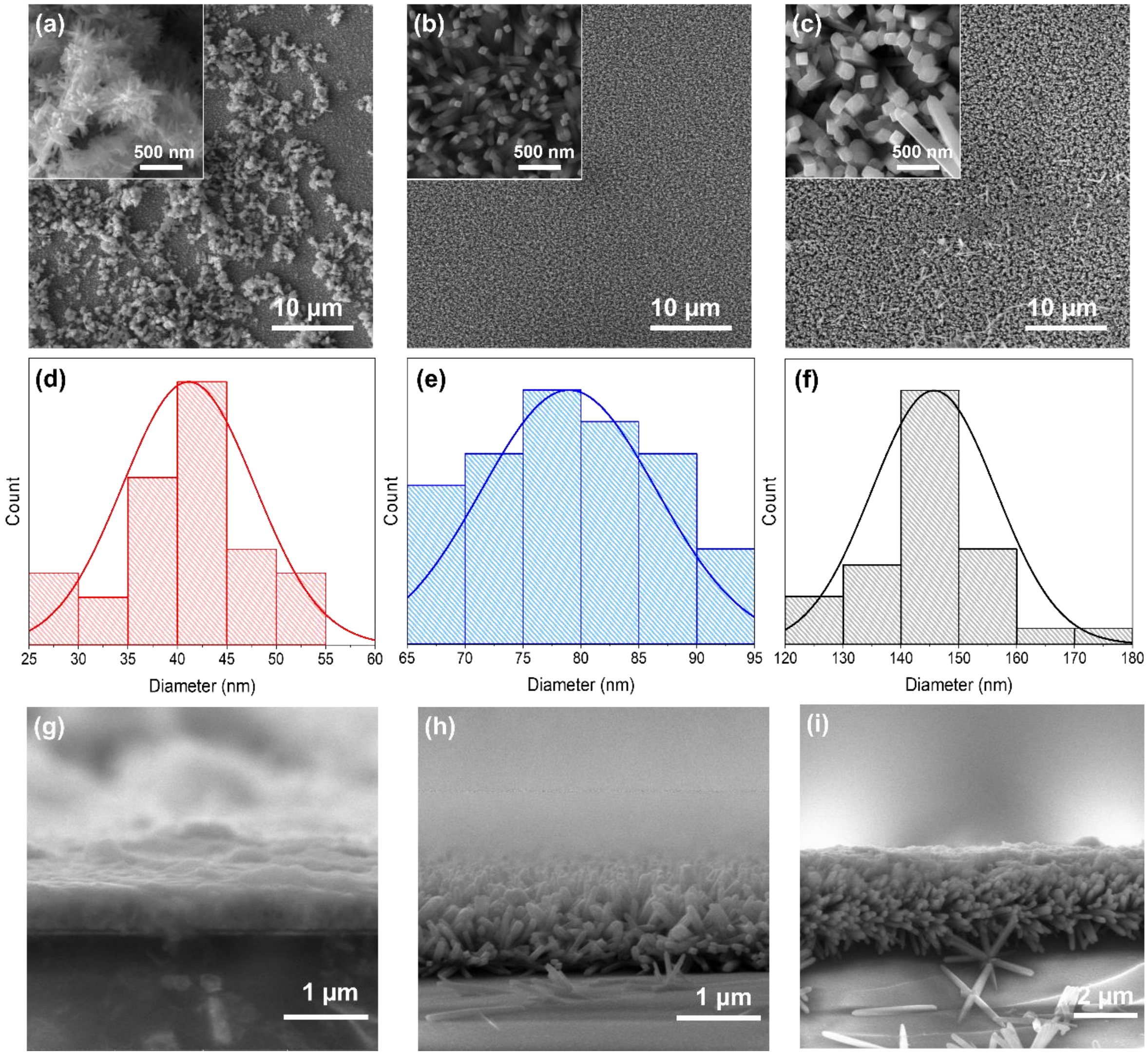

**Figure 4.2 SEM images of the $TiO_2$ NRs obtained at different growth time (a) 3 h (b) 4 h and (c) 5 h. Diameter distribution for: (d) 3 h; (e) 4 h and (f) 5 h. Thickness variation for (g) 3 h; (h) 4 h and (i) 5 h.**

## 4.3 Structural characterization of the photoanode

XRD was utilized to identify the crystal structure of the $TiO_2$ NRs. Figure 4.3 (a) presents the XRD patterns of the $TiO_2$ NRs grown for 4 h over the $TiO_2$ blocking layer on the surface of the FTO sample. From these results, the crystal structure of the $TiO_2$ NRs is the rutile structure (JCPDS No.88–1175). The peak with the highest intensity at 62.9° is associated with the (002), which confirms that the NRs are perpendicular to the surface and grow in the [001] direction. Two different groups of peaks are associated with the $SnO_2$ in the FTO (S peaks) and anatase $TiO_2$ (A peaks) from the blocking layer.

After the growth of $TiO_2$ NRs over the blocking layer surface, two layers of anatase $TiO_2$ mixed paste (20 and 450 nm particle size) were deposited on top of them by using the tape casting method. Later, the sensitization process was made with five cycles of CdS QDs to construct the photoanode. To confirm the homogenous distribution of the QDs all over the as designed photoanode, EDS elemental mapping technique was applied. Figure 4.3 (b) shows the cross-sectional image of the photoanode, and the green rectangle represents the selected area for elemental analysis. The elemental mapping results are shown in Figure 4.3 (c). The images confirm the homogenous distribution of the sensitized CdS QDs within the $TiO_2$ hybrid structure.

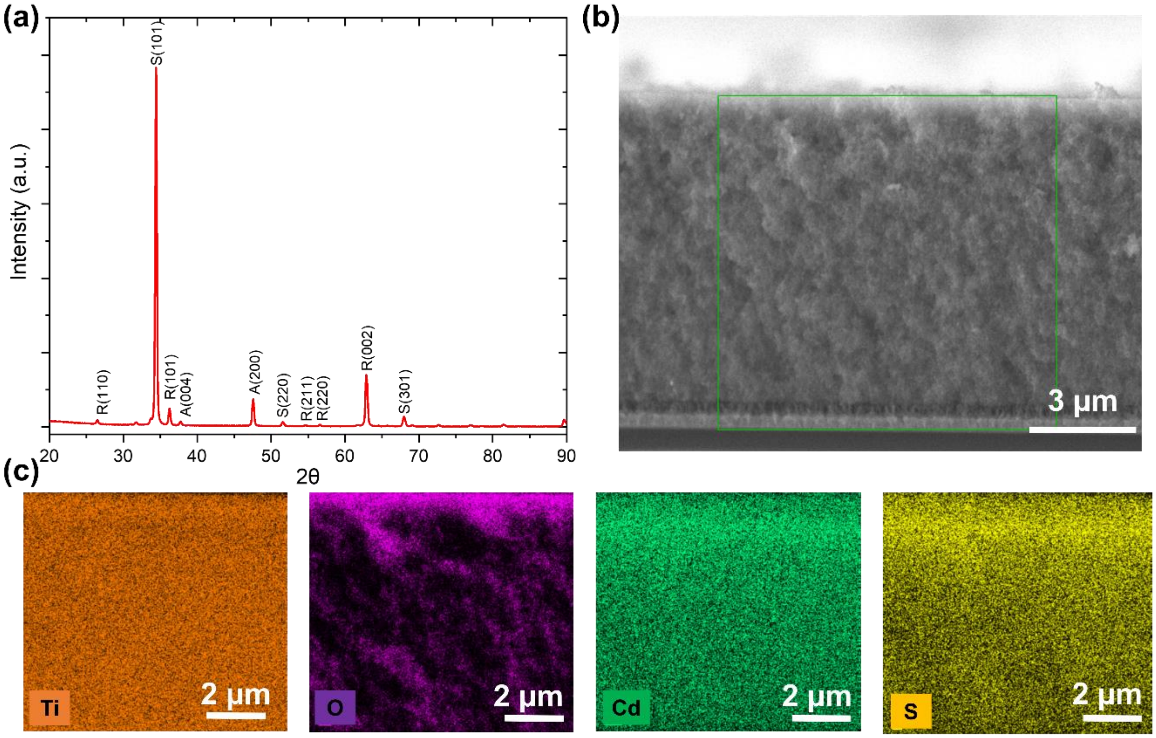

**Figure 4.3 XRD patterns of TiO2 NRs (b) cross-section SEM image of the $TiO_2$ hybrid structure (c) elemental maps of Ti, O, Cd, S.**

## 4.4 Effect of $TiO_2$ NRs length on PEC performance

In the PEC measurements, the photoanodes hybrid structure was based on different x $TiO_2$ NRs (where x represents the growth time 3, 4, and 5) and two layers of $TiO_2$ mixed NPs sensitized by CdS QDs. The photocurrent density and electron lifetime were investigated by using the LSV and OCP methods. In the LSV, the measurements were carried out under dark, continuous light, and chopped illumination. The sun simulator was adjusted at 100 mW $cm^{-2}$ while using AM 1.5 filter to simulate the solar spectrum. Figure 4.4 (a) – (d) shows the photocurrent density vs potential for the reference same (i.e., without NRs), 3 NRs/NPs, 4 NRs/NPs, and 5 NRs/NPs, respectively. The results show that there is a significant improvement in the photocurrent density with the device based on 4 NRs/NPs with 3.33 mA cm$^{-2}$ at 0.8 V vs RHE. This device shows a 113% improvement as compared to the reference device (1.56 mA cm$^{-2}$ at 0.8 V vs RHE). Moreover, the PEC device based on 4 NRs/NPs shows superior performance as compared to 3 and 5 NRs/NPs. This is attributed to the device based on 3 NRs/NPs having an inhomogeneous distribution of the NRs, with insufficient time for complete crystallinity, and its small NRs size. This results in an insignificant improvement in the charge transfer properties of the photoinjected electrons from the QDs to the hybrid photoanode structure. Thus, a negligible difference in the photocurrent density was obtained as compared to the reference device. On the other hand, for the 5 NRs/NPs, the overgrowth reduces the photocurrent density (2.86 mA cm$^{-2}$ at 0.8 V vs RHE) due to several factors: (1) the surface density of the NRs is lower as compared to 4 NRs, which decrease the collection probability of the photogenerated carriers. (2) The NRs size is bigger, which decreases the active surface area for the QDs deposition. (3) The length of the 5 NRs is double the 4 NRs, which increases the overall thickness of the photoanode, and increases the path length of the photoinjected carriers. Consequently, the recombination probability of the photoinjected carriers increases. To confirm these assumptions for the performance of different PEC devices, the OCP decay measurement and electron life calculations were conducted as shown in Figures 4.4 (e) and (f), respectively. The samples were illuminated for 50 s to achieve a stable potential then the light turns off and the decay of the measured potential with time is recorded. The voltage decay in the measurement represents the recombination rate of the photogenerated electrons and thus the electron lifetime calculations are a strong correlation to the recombination of the charge carriers. In the OCP measurements, the potential decay for all hybrid structure photoanode reaches a plateau after the light was switched off, while the reference device continues to decrease with time. These results indicate that the reference device has a higher recombination rate as compared to other hybrid structure photoanodes. In addition, the electron lifetime calculations in Figure 4.4 (f) show that at any given potential, the electron lifetime of 4 NRs/NPs is higher than all other devices, which is aligned with the LSV results. Moreover, the lifetime calculations present a faster decay for the reference device as compared to other hybrid structures. These results conclude that the optimized growth time for the NRs is 4 h, which improves the charge transfer properties and reduces the recombination rate in the PEC device.

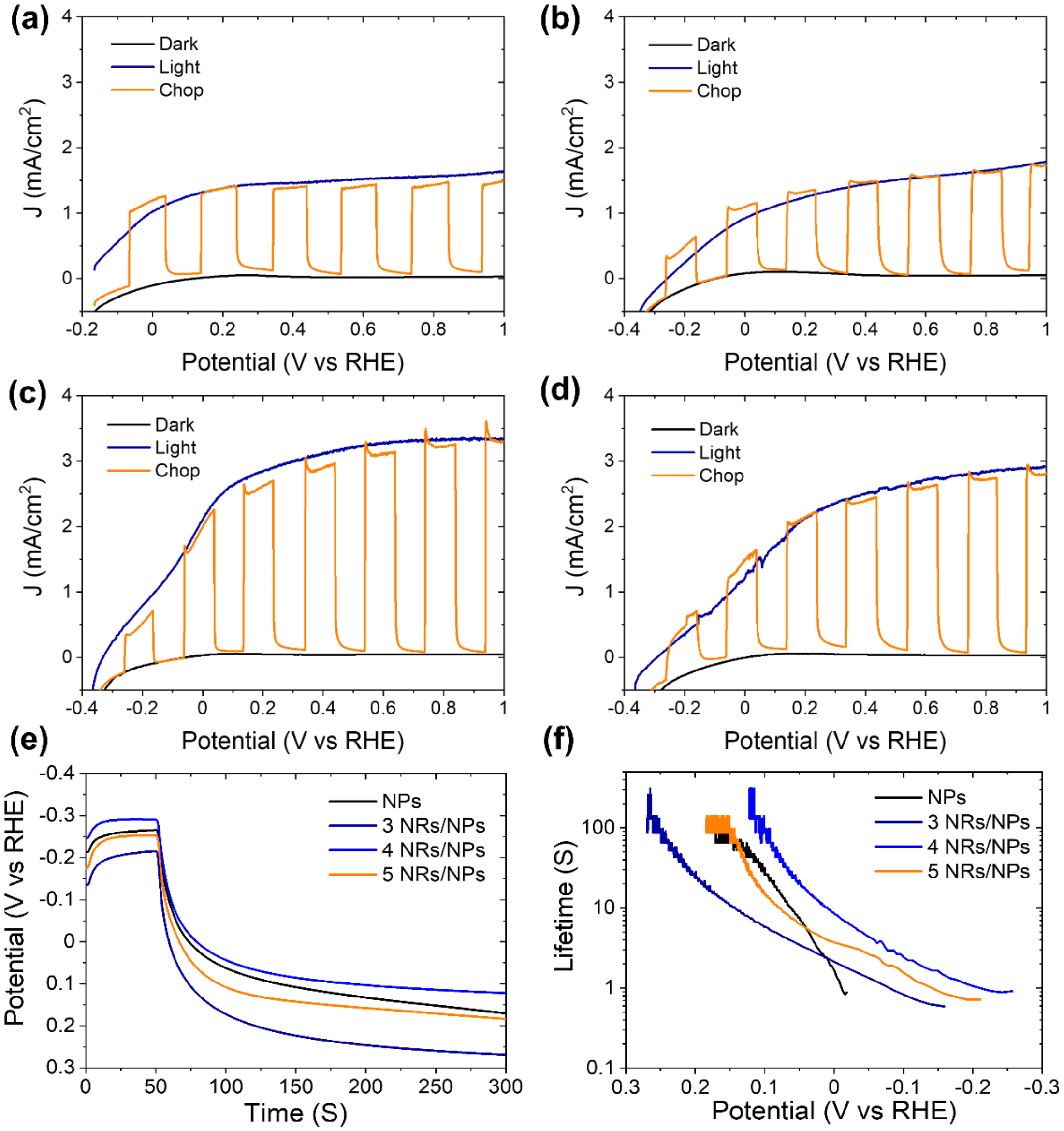

**Figure 4.4 LSV measurement under dark, light, chopped for the photoanode based on (a) reference, (b) 3 NRs/NPs, (c) 4 NRs/NPs, (d) 5 NRs/NPs with CdS QDs. (e) OCP measured and (f) electron lifetime calculations for different hybrid structure photonades.**

## 4.5 Effect of $TiO_2$ NPs size on PEC performance

Further optimization of the hybrid structure was achieved by the selection of the NPs. Two different types of anatase $TiO_2$ paste are commercially available: (a) the mixed paste with 20 and 450 nm particle size with one layer after annealing results in ~7-8 μm thickness, and (b) the transparent paste with 20 nm particle size with the final thickness of the film after annealing in the range of ~5-6 µm. The difference in the film thickness is attributed to the NPs size in the paste.

For the PEC measurements, the $TiO_2$ NRs were fixed with 4 h growth time while the $TiO_2$ NPs were changed into three different configurations: (1) reference sample used in the previous section, with two mixed layers, (2) one transparent layer and one mixed layer, and (3) two transparent layers. The average thickness of each NPs composite structure was measured using a profilometer and the thickness were 15, 13, and 10 µm for two mixed, one transparent and one mixed, and two transparent NPs layers, respectively. Several factors influence the performance of the PEC devices with changing the NPs size and thickness, such as:

1) The QDs loading: The amount of QDs deposited using the SILAR method depends on the available active surface area in the photoanode. As the available active surface area increases, the QDs loading increases. Small size NPs result in a more active surface area. Accordingly, the QDs loading in the transparent paste is considered higher as compared to the mixed one.
2) Overall photoanode thickness: As the final thickness of the ETL film increase, the distance required from the photogenerated electrons to reach the conductive substrate increases. Consequently, a higher chance of charge recombination exists, as the number of defects and trap sites increases. This gives rise to a higher rate of carrier recombination and low collection efficiency of the charge carriers. Therefore, a small thickness from a small NPs size reduces the overall thickness and eventually improves the performance of the PEC device.
3) Carrier dynamics: The carrier dynamics is affected by the interaction between the ETL and the electrolyte. The colloidal NPs provide a porous structure, which increases the electrolyte penetration tendance, and more interactions take place between the exposed ETL area and the electrolyte. The porosity depends on the NPs size, where a large particle size produces larger porosity. Thus, the mixed paste provides higher porosity as compared to the transparent one.
4) Light scattering: The tendency for light scattering depends on the NPs size inside the ETL film. The light scattering influences the average path length of the light, which directly affects the absorption efficiency and the photoexcitation of the sensitized QDs. A larger particle size triggers more light scattering. Consequently, the mixed paste provides more light scattering for the hybrid photoanode.

These factors clarify that there is a clear tradeoff effect that occurs with different NPs. To reach the optimized structure, the performance of the PEC devices was examined. LSV measurements are conducted as shown in Figure 4.5 (a)-(c) for the two mixed, one transparent and one mixed, and two transparent NPs layers, respectively. The PEC device based on two transparent NPs shows the highest photocurrent density with 4.25 mA cm$^{-2}$ at 0.8 V vs RHE, which is 28% higher as compared to the reference device (3.33 mA cm$^{-2}$ at 0.8 V vs RHE). A comparison in the photocurrent density vs potential for the three composite structures under continuous light is presented in Figure 4.5 (d). These results suggest that the optimized hybrid structure consists of NRs with 4 h growth time and NPs with two layers of 20 nm particles size.

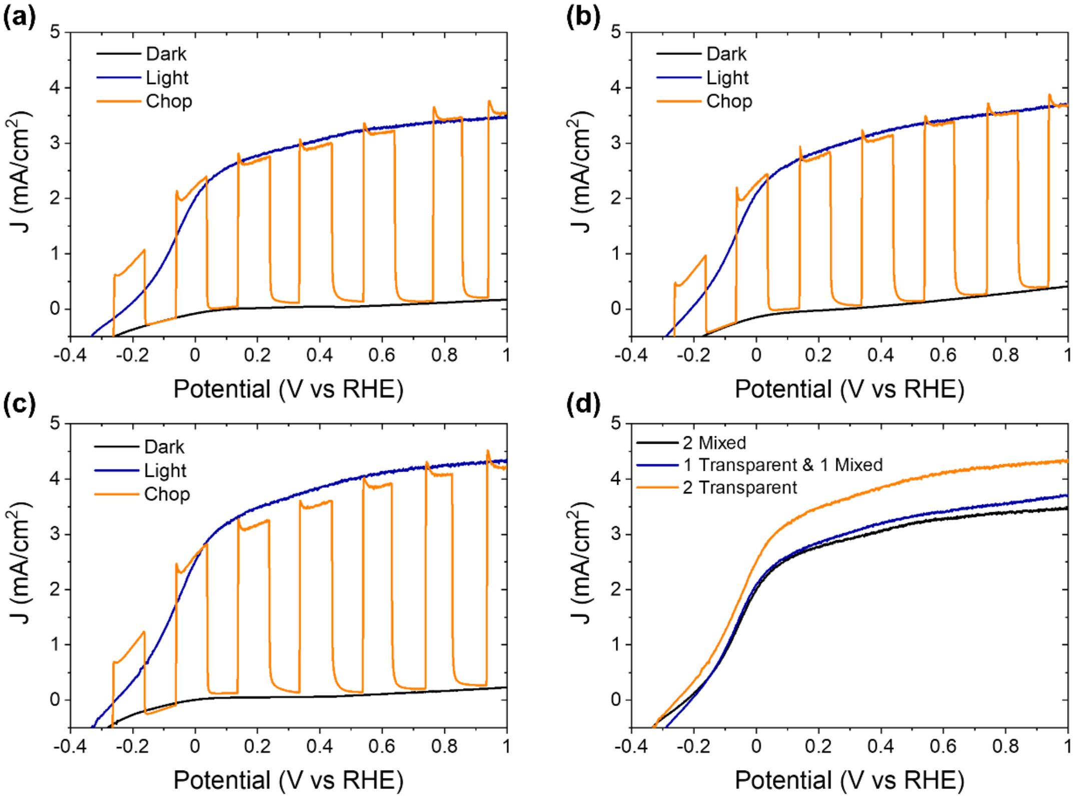

**Figure 4.5 LSV measurement: dark, light, and chopped performance for the hybrid photoanode structure with 4 h $TiO_2$ NRs sensitized with CdS QDs with different TiO2 NPs. (a) 2 mixed. (b) 1 transparent and 1 mixed. (c) 2 transparent. (d) Continuous illumination comparison between the different composite structures.**

## 4.6 Effect of hydrazine treatment on the structural and optical properties of the photoanode

The optimized hybrid structure photoanode was subsequently treated with hydrazine before the sensitization with QDs. The role of this treatment is nitrogen doping, which acts as a trap screener inside the ETL. Reducing the number of traps significantly affects the recombination rate and consequently the PEC device performance. However, transition metal doping and other co-doping heteroatoms form an intermediate bandgap that shifts the absorption of the $TiO_2$ into the visible region [147]. In addition, the intermediate bandgap acts as a source of recombination sites and further increases the recombination rate of the photogenerated charge carriers and reduces the overall device performance [59]. Furthermore, since the main objective of the ETL is to transfer the photoinjected electrons from the QDs to the FTO, therefore competition in light-harvesting between the ETL and the QDs in the visible region is undesirable. Thus, controlling the concentration of the hydrazine treatment and it's structural and optical characterization is crucial to overcome these problems.

The concentration used for the hydrazine treatment varies from 0.25, 0.5, and 1 M. The solution was pre-heated at 70$^{o}$C, before the dipping of the hybrid structure photoanode, and then kept for 30 min. Subsequently, the samples were annealed at 500$^{o}$C for the decomposition of hydrazine into nitrogen (equation 4.1)

$$N_2H_4 + O_2 \rightarrow N_2 + H_2O \ (equation\ 4.1)$$

UV-Vis measurement and the optical bandgap calculations using Tauc plot were conducted for the reference photoanode (i.e., FTO with TiO2 NRs/NPs optimized hybrid structure) and the hydrazine treated photoanode with 0.25 M and 0.5 M, as shown in Figure 4.6 (a). The results confirm that there is no shift in the absorption spectrum with the hydrazine treatment into the visible region. In turn, the existence of an internal bandgap was not achieved in these concentrations of hydrazine treatment. In addition, slight changes in the optical bandgap were achieved with a difference of 0.1 eV for the reference and treated samples.

The chemical compositional analysis on the surface is important to justify the nitrogen doping in the photoanodes. XPS was used to examine the reference and treated samples to identify the existence and nature of nitrogen bonding inside the photoanode. Moreover, the VBM position of the samples was identified, which implies any variation, if exists, in the electronic band structure after the hydrazine treatment. The high-resolution XPS spectra for the N 1s for the reference, 0.25 M, and 0.5 M hydrazine treated samples are presented in Figure 4.6 (a) – (c), respectively. The XPS spectra confirm the successful deposition of nitrogen for the 0.25 M and 0.5 M treated samples with the main peak located at a binding energy of 400 eV. The non-existence of the 396-eV peak confirms that there is no interaction between Ti and N, which is the main contributor to the formation of the internal bandgap [148]. Nevertheless, the 400-eV peak is associated with the molecular chemisorption of γ-$N_2$ bonding in the form of Ti-O-N or N-Ti-O [149]. Furthermore, to confirm that there are no changes in the $TiO_2$ interaction, the Ti 2p and O 1s spectra are presented in Figure 4.6 (f) and (g). The main peaks for the Ti 2p and O 1s were similar for the hydrazine treated samples as compared to the reference one. Finally, the V.B. edge position for the reference and treated samples were acquired in the high-resolution spectra of the V.B. region. The linear extrapolation of the peak to the baseline identifies the V.B. edge position. From Figure 4.6 (e), the results show that the position of the V.B. is the same for all samples with 2.45 eV. Combining the XPS results with the optical bandgap calculations validates that the electronic band structure of the hybrid photoanode is not influenced by the hydrazine treatment.

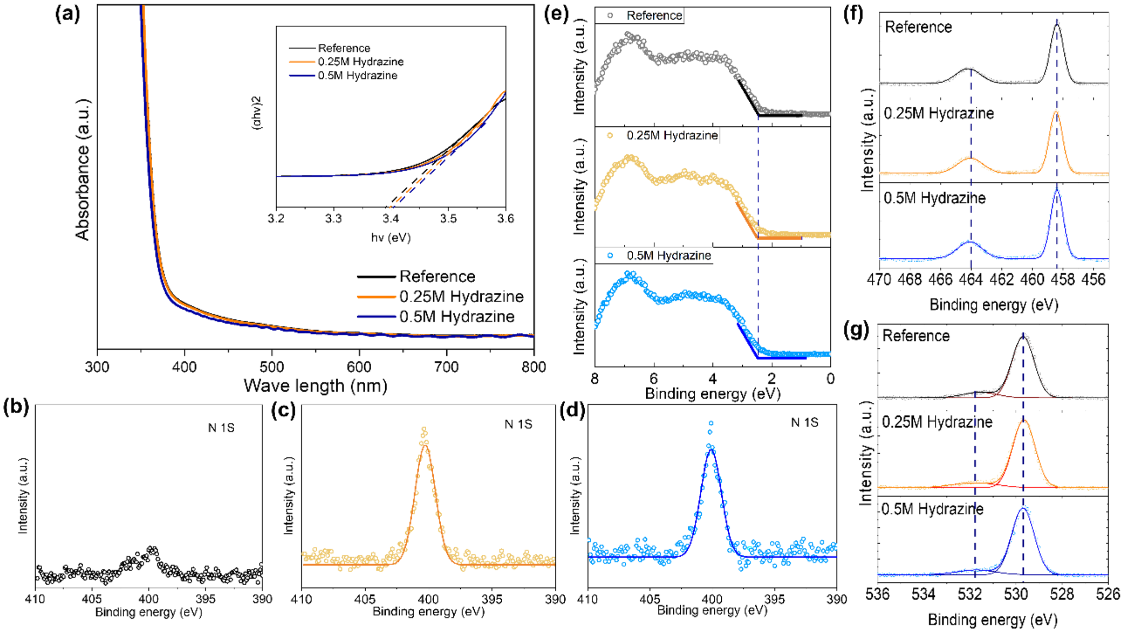

**Figure 4.6 (a) UV–visible absorption spectra and the inset calculated bandgaps for reference and hydrazine treated samples. High-resolution spectra for the N 1S for (b) reference, (c) 0.25 M, and (d) 0.5 M hydrazine treated samples. The valency band (e), Ti 2p (f), and O 1s (g) spectra for reference, 0.25 M, and 0.5 M hydrazine treated samples.**

## 4.7 Effect of Hydrazine treatment on PEC performance

LSV measurement was conducted to investigate the impact of hydrazine treatment on the photocurrent density of the PEC devices based on the optimized TiO2 NRs/NPs hybrid structure sensitized with CdS QDs. The saturated photocurrent density vs potential for the reference, 0.25 M, 0.5 M, and 1 M hydrazine treatment samples are presented in Figure 4.7 (a) – (d), respectively. The photocurrent density of the device based on 0.25 M hydrazine treatment shows a significant improvement with a 28 % increase in the photocurrent density as compared to the reference device, as shown in Figure 4.7 (e). Yet, a higher concentration of hydrazine treatment (i.e., 0.5 M and 1 M) reduces the device's performance as compared to the reference device. The improvement of the photocurrent density is attributed to the trap screening effect of nitrogen doping. On the other hand, a higher concentration of doping may not introduce an intermediate bandgap but can generate more trap sites that act as recombination centers and reduce the PEC device performance. The stability test is conducted for the reference, 0.25 M, and 0.5 M hydrazine treated samples for 2 h under one sun continuous illumination at 0.6 V vs RHE [Figure 4.7 (f)]. The stability test results show that the hydrazine treatment does not affect the long-term stability of the PEC devices. EIS was carried out to study the carrier dynamics of hydrazine treatment samples. The actual and fitting data from the EIS measurement are shown in Figure 4.7 (g), while the equivalent circuit used to stimulate the actual data is presented in Figure 4.7 (h). The measurement was carried out under dark conditions with an applied bias of 0.2 V. The data for each component in the electronic circuit is shown in table 4.1. The 0.25 M hydrazine treatment samples show a reduction in the charge transport resistance ($R_2$) as compared to the reference and 0.5 M treated samples. This reduction indicates that the charge trapping and de-trapping are considerably lower due to the screening of the trap sites inside the hybrid structure photoanode. On the other hand, for the 0.5 M treated sample, the charge transport resistance, as compared to the reference sample, indicates a greater number of surface traps and resistance for charge carrier movement inside the photoanode. In addition, the charge transfer resistance ($R_3$) of the 0.25 M hydrazine treatment samples is higher as compared to the reference and 0.5 M treated samples. Higher charge transport resistance reflects higher recombination resistance between the charge carriers inside the photoanode and oxidized species in the electrolyte. From these data, the device based on 0.25 M hydrazine treatment reduces the overall non-radiative carrier recombination inside the photoanode and at the photoanode/electrolyte interface, which yields better device performance. This conclusion is consistent with the *j-v* performance of the corresponding PEC devices.

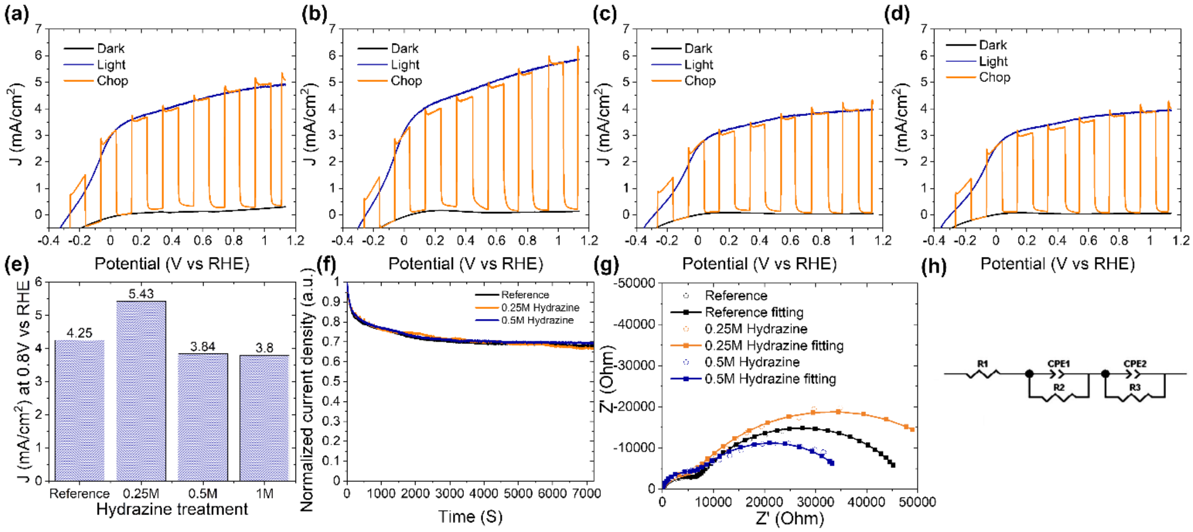

**Figure 4.7 PEC performance under dark, light, and chop for hybrid $TiO_2$/CdS QDs with (a) reference, (b) 0.25 M, (c) 0.5 M, and (d) 1 M hydrazine treatment. (e) photocurrent density comparison at 0.8 V vs RHE. (f) Stability test. (e) EIS actual and fitted results (h) the equivalent circuit used for simulation**

**Table 4.1 EIS measurement for $TiO_2$ with different hydrazine treatments**

| Electronic component | Reference | 0.25M hydrazine | 0.5M hydrazine |
|---|---|---|---|
| $R_1$ (ohm) | 13.72 | 12.84 | 13.87 |
| $R_2$ (ohm) | $5.09 \times 10^3$ | $4.83 \times 10^3$ | $5.9 \times 10^3$ |
| $C_{SC}$ (F) | $9.81 \times 10^{-6}$ | $1.11 \times 10^{-5}$ | $9.01 \times 10^{-6}$ |
| $R_3$ (Ohm) | $3.79 \times 10^4$ | $4.68 \times 10^4$ | $2.93 \times 10^4$ |
| $C_H$ (F) | $3.96 \times 10^{-4}$ | $1.57 \times 10^{-4}$ | $1.04 \times 10^{-4}$ |

After the optimization of the $TiO_2$ NRs, NPs, and the hydrazine treatment concentration. The PEC device performance was enhanced by changing the sensitized QDs from CdS to CdS/CdSe. In the LSV measurement, the photocurrent density of the device based on CdS/CdSe QDs shows a significant improvement with a saturated photocurrent density of 8.12 mA $cm^{-2}$ at 0.8 V vs RHE [Figure 4.8 (b)], which is a 50% increase as compared to the device based on only CdS QDs (5.43 mA $cm^{-2}$ at 0.8 V vs RHE) [Figure 4.8 (a)]. Moreover, the long-term stability shows 13% improvement, which maintains 80% of the initial photocurrent density after 2 h of continuous one sun illumination for the device based on CdS/CdSe QDs, as compared to CdS QDs with only 67% stability [Figure 4.8 (c)]. The enhancement in both the photocurrent density and stability is attributed to the increase in light-harvesting efficiency through widening the absorption range and improved carrier dynamics. In particular, the proper band alignment of the QDs with the hybrid

$TiO_2$, as shown in Figure 4.8 (d), enhances the photo injection process and the hole transport properties at the photoanode/electrolyte interface. The improvement in the injection process enhances the photocurrent density, while the faster hole transport properties increase the long-term stability of the PEC device. To evaluate the practical $H_2$ generation for the final optimized device based on CdS/CdSe QDs, GC measurements were conducted. Figure 4.8 (e) presents the $H_2$ evolution rate with 49.5 $\mu mol\ h^{-1}$ and an average FE of 80.5%. Finally, IPCE measurements were conducted the identify the effect of hydrazine treatment (0.25 M) on the best performing device (i.e., Hybrid $TiO_2$ with CdS/CdSe QDs). The comparison in the IPCE measurements is shown in Figure 4.8 (f). The calculations of the IPCE were made by the photocurrent density obtained at the potential 0.8 V vs RHE. The IPCE curve indicates that the hydrazine treatment improves the conversion efficiency over the 350-800 nm spectrum range.

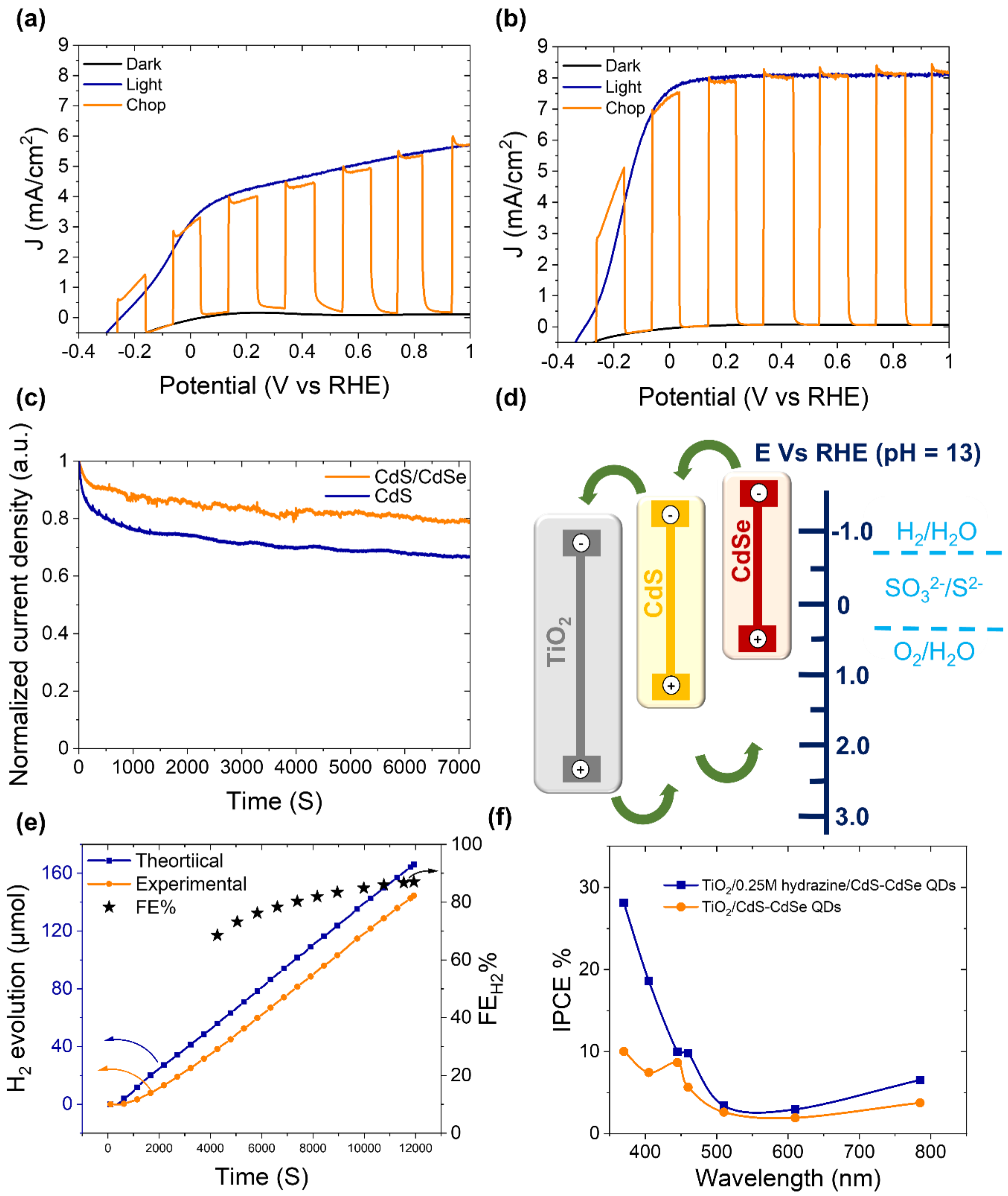

**Figure 4.8** PEC performance under dark, light, and chop for hybrid $TiO_2$ treated with 0.25 M hydrazine with (a) CdS QDs, (b) CdS/CdSe QDs. (c) The stability test (d) A schematic representation for the PEC device based on CdS/CdSe QDs. (e) $H_2$ evolution and FE of 0.25 M hydrazine treated hybrid $TiO_2$ sensitized by CdS/CdSe QDs. (f) IPCE calculations

## 4.8 Computational model and methods

The computational study was made to understand the mechanism of hydrazine treatment. The simulations investigate the interaction of $N_2H_4$, $N_2$, and N at the surface and interstitial sites of $TiO_2$. The anatase (101) surface of $TiO_2$ was used in this study with two interstitial N atoms to analyze the effect of increased hydrazine concentration. In addition, four adsorption sites on the surface of $TiO_2$ and two interstitial N-doped supercells were prepared by embedding one and two N atoms into the interspace. The calculations were made to (a) estimate the relative incorporation stability of the $N_2H_4$, $N_2$, and N with the adsorbed and doped species into the host lattice; (b) investigate and calculate the adsorption and defect formation energies of all forms of hydrazine interaction on the four unique sites of $TiO_2$ anatase (101) surface (i.e., five-fold coordinated Ti (Ti5c), six-fold coordinated Ti (Ti6c), two-fold coordinated O (O2c), and three-fold coordinated O (O3c); (c) Calculate the electronic properties of the pristine $TiO_2$ anatase (101) surface, as well as doped $TiO_2$ anatase (101) surface with chemically adsorbed $N_2$, chemically adsorbed N, and interstitially doped N [Figure 4.9]. All these results cover the mechanism of hydrazine treatment and its effect on the electronic band structure, which can be correlated to the overall PEC device performance.

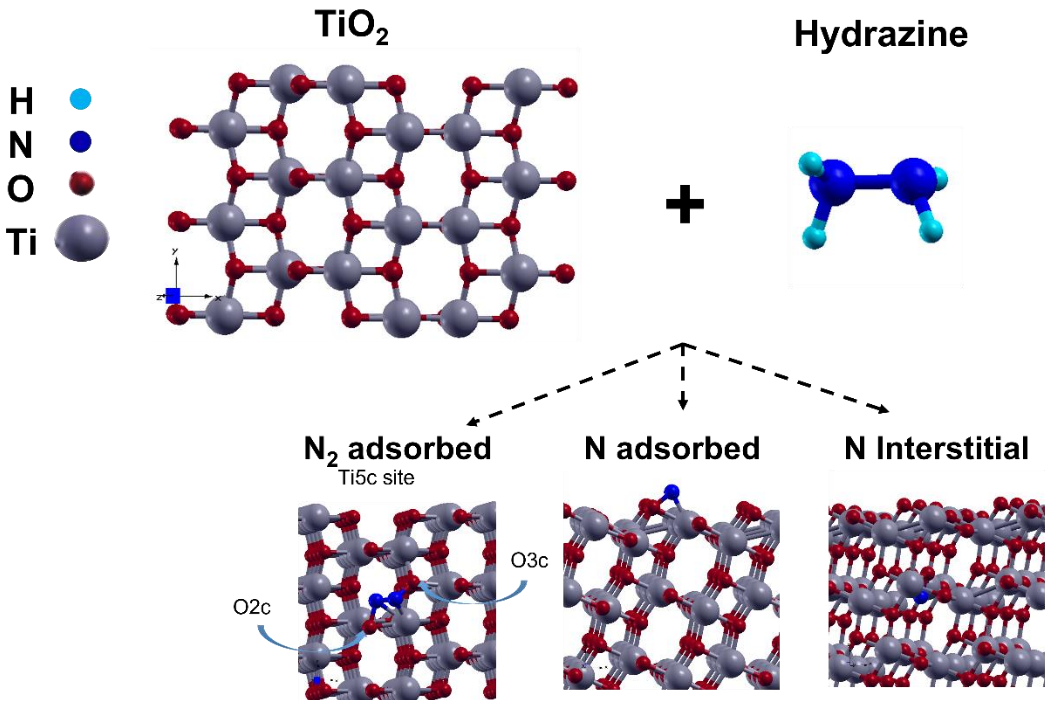

**Figure 4.9 most stable structure of hydrazine treatment on TiO2 anatase (101) plane**

According to the theoretical calculations, the existence of N can be either in the interstitial site or adsorbed on the surface. It mainly depends on the adsorption and defect formation energies.

The adsorption energy was calculated from the following equation:

[$\delta H_{ads} = E_{tot} - E_{bare} - E_{ad}$]

where $E_{tot}$ ($E_{bare}$) is the energy of the surface with (without) adsorbate and $E_{ad}$ is the energy of the isolated adsorbate species calculated in the same supercell.

The interstitial N-doped was also calculated from the defect formation energy using the following equation: [$E_f = E_{tot} - E_{bare} - m\mu_N$]

Where $E_{tot}$ ($E_{bare}$) is the energy of the surface with (without) interstitial N atoms; $\mu_N$ represents the chemical potentials of the N; $m$ is the number of doped nitrogen atoms.

Afterward, the calculations were performed on different configuration sites to check the stability of the adsorbates or dopants nitrogen. The results show that nitrogen doping through the hydrazine treatment results in two isolated N 2p states localized at the top of the VBM and the bottom of the CBM. The interaction between the anatase surface and the nitrogen dopant forms a mid-gap state at different locations depending on the type of interaction between them. From the DFT+U calculations the mid-gap states exists in three locations: (a) 1.0 eV below CBM for the adsorbed $N_2$ [Figure 4.10 (b)]; (b) 0.55 eV very close to the CBM for the adsorbed N atoms [Figure 4.10 (c)]; and (c) 1.8 eV below CBM for the interstitial N [Figure 4.10 (d)]. The density of states of the anatase surface indicates that with the increase in the number of interstitial N atoms (e.g., 2 interstitial atoms), the number of mid-gap states close to the CBM also increases, which can increase the recombination centers significantly [Figure 4.10 (e)]. That is why we conclude that the anatase surface with adsorbed or interstitially doped N (which occurs with 0.5 M and 1 M hydrazine treatment) can result in the creation of recombination centers, thereby reducing the performance of the $TiO_2$/QDs PEC devices.

To conclude the computational study, the anatase surface with the coordination of adsorbed or interstitially doped N results in the creation of recombination centers. These centers act as a trap site for the photogenerated carriers and reduce the performance of the $TiO_2$/QDs system, which can be related to the case of 0.5 and 1 M hydrazine treatment samples. On the other hand, the $N_2$-adsorbed surface appears to have the lowest possibility of developing recombination centers without participating in light-harvesting and competing with the QDs. Thus, the $N_2$-adsorbed surface, with 0.25 M concentration, could be accountable for the enhanced PEC performance of hydrazine-treated $TiO_2$.

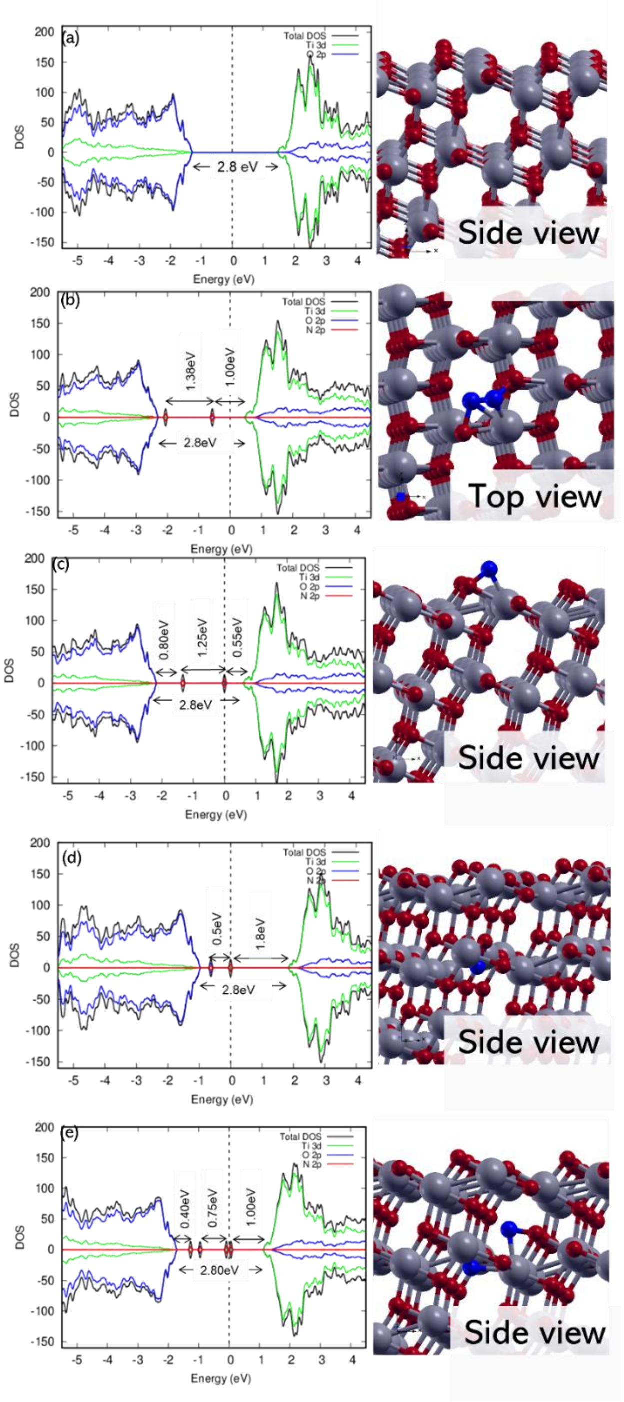

**Figure 4.10** DOS on p and d orbitals of (101) anatase plane with (a) no defects, (b) adsorbed $N_2$, (c) adsorbed N, (d) one Interstitial N atom, and (e) with two interstitial N atoms

## 4.9 Summary

In this chapter, the work is focused on the fabrication of a hybrid structure photoanode that can enhance the charge transport properties and overcome the charge recombination within the photoanode, without additional nanostructured materials, to improve the PEC device performance. The hybrid photoanode consists of 1D NRs and NPs and the optimization process was conducted on each part to reach the optimum performance. The NRs were used to provide a directional pathway for the photoinjected electrons and improve the carrier dynamics. While the NPs provide the proper porosity and surface area for the QDs deposition and electrolyte penetration. After the optimization of the photoanode structure, the hybrid photoanode was treated with hydrazine to reduce the surface traps and further boost the PEC performance. The role of surface engineering via nitrogen doping is to suppress non-radiative carrier recombination inside $TiO_2$ by screening the trap sites in the electronic band structure. Finally, DFT+U calculations were used to underpin the enhancement in the device performance by studying the effect of nitrogen doping on the electronic band structure of the hybrid $TiO_2$ photoanode. This work provides a systematic approach to optimizing the photoanode structure, as well as reducing the undesirable carrier recombination through a simple solution-based hydrazine treatment method.

# CHAPTER 5: P-N HETEROJUNCTION IN QUANTUM DOTS (QDS) BASED PHOTOELECTROCHEMICAL (PEC) DEVICES

## 5.1 Project plan

In this chapter, the PEC device architecture was further simplified. The methods used for fabrication were made through simple low-cost solution-based processes at an ambient condition that makes it easy for commercialization. Compared to the previous chapter, instead of optimizing the $TiO_2$ nanorods (NRs) and $TiO_2$ nanoparticles (NPs) for better carrier dynamics, the $TiO_2$ nanotubes (NTs) were used to combine all the desired properties altogether. The $TiO_2$ NTs were utilized as a template for the QDs deposition [150]. In addition, the $TiO_2$ NTs exhibit a directional pathway characteristic for the photogenerated carrier [151]. Apart from these features, the electrochemical anodization process used to grow the self-organized $TiO_2$ NTs is simple and cost-effective compared to the several steps employed in the fabrication of the photoanode (i.e., chemical bath deposition for the $TiO_2$ blocking layer, tape casting for the $TiO_2$ NPs, and hydrothermal process for the $TiO_2$ NRs) [152]. This can help in reducing the overall cost of the device and makes it scalable and fit for commercialization. Moreover, as a replacement for implementing strategies to overcome the carrier recombination (i.e., functionalized hexagonal boron nitride “F-h-BN” and hydrazine treatment), a nanoscale p-n heterojunction is designed to improve the surface potential that can enhance the charge separation process at the photoanode/electrolyte interface for better device performance. Finally, the effect of $TiO_2$ NTs length on the photogenerated current density and stability were examined. The design concept of the photoanode is illustrated in Figure 5.1. This work was published in Chemical Engineering Journal, 446, 137312, 2022.

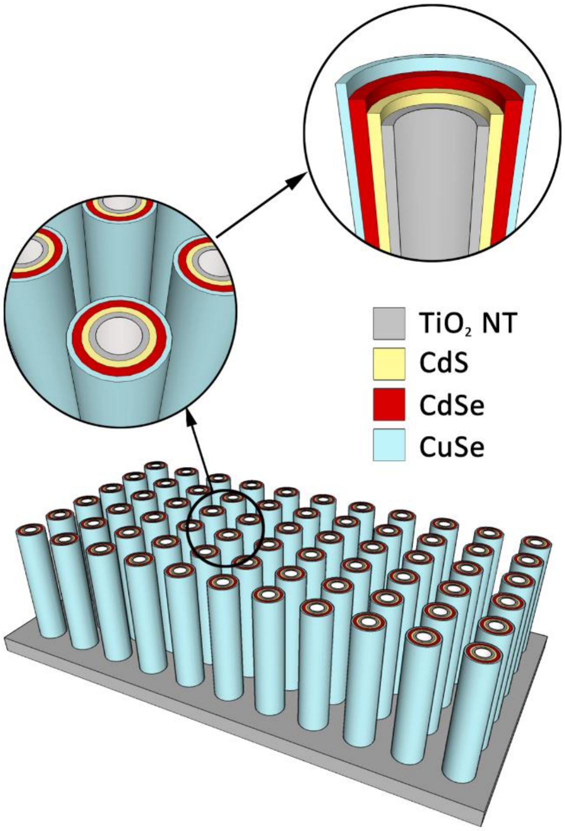

**Figure 5.1 Schematic illustration of the structure of the designed photoanode**

## 5.2 Structural characterization of the $TiO_2$ NTs

The anodization process was made on Ti foil that is used as a working electrode, pt as the cathode, and the electrolyte solution consists of 97 vol. % ethylene glycol and 3 vol. % DI water with 0.5 wt. % ammonium fluoride. The applied potential was 50 V made for 30 and 60 min to investigate the effect of $TiO_2$ NTs length on the PEC device performance. After the anodization process, IPA was used for washing in an ultrasonication bath, and a nitrogen stream was used for drying. Finally, the as-prepared $TiO_2$ NTs were annealed at $500^oC$ for 1 h for complete crystallization. Figure 5.2 (a) and (b) present the $TiO_2$ NTs before the annealing process. From these images, the anodization process can be confirmed to provide well-aligned $TiO_2$ NTs. The controlled morphology of the $TiO_2$ NTs has the desired porosity with a high specific surface area. These properties provide a good template for high QDs deposition and proper electrolyte penetration that can affect both the light absorption efficiency and carrier dynamics at the photoanode/electrolyte interface. Moreover, the $TiO_2$ NTs themselves have 1D morphology that provides the direct pathway characteristics for the photogenerated carriers that enhances the charge transport properties. Figure 5.2 (c) and (d) show the $TiO_2$ NTs after the annealing process. The importance of the annealing is to achieve a complete crystalline structure with a low number of defects that can act as trap sites and reduce the overall PEC device performance. The SEM images confirm that there is an insignificant difference in the $TiO_2$ NTs morphology before and after annealing. XRD was used to confirm the complete crystallization of $TiO_2$ NTs. The XRD patterns for the Ti substrate, $TiO_2$ NTs amorphous, and crystalline structure after annealing are shown in Figure 5.2 (e). The additional peaks presented for the crystalline $TiO_2$ NTs at 2θ with $25.2^o$ and $48^o$ are associated with the diffraction pattern of the $TiO_2$ anatase crystalline phase (JCPDS*:* 01-071-1167). Moreover, the peak at $37.8^o$ is associated with the (004) plane, which confirms the $TiO_2$ NTs grown in a direction perpendicular to the surface of the substrate [153]. High-resolution images were acquired by TEM to investigate the morphology of the annealed $TiO_2$ NTs. Figure 5.2 (f) shows that the average length of the $TiO_2$ NTs is equal to ~1 μm. This is related to the 30 min anodization time. Figure 5.2 (g) shows the inner diameter consists of ~ 58 nm diameter, with an average wall thickness of ~27 nm. Finally, the atomic resolution image [Figure 5.2 (h)] shows that the lattice spacing of the $TiO_2$ NTs is ~3.52 Å, which relates to the (101) plane that is associated with the tetragonal anatase phase of $TiO_2$ [154].

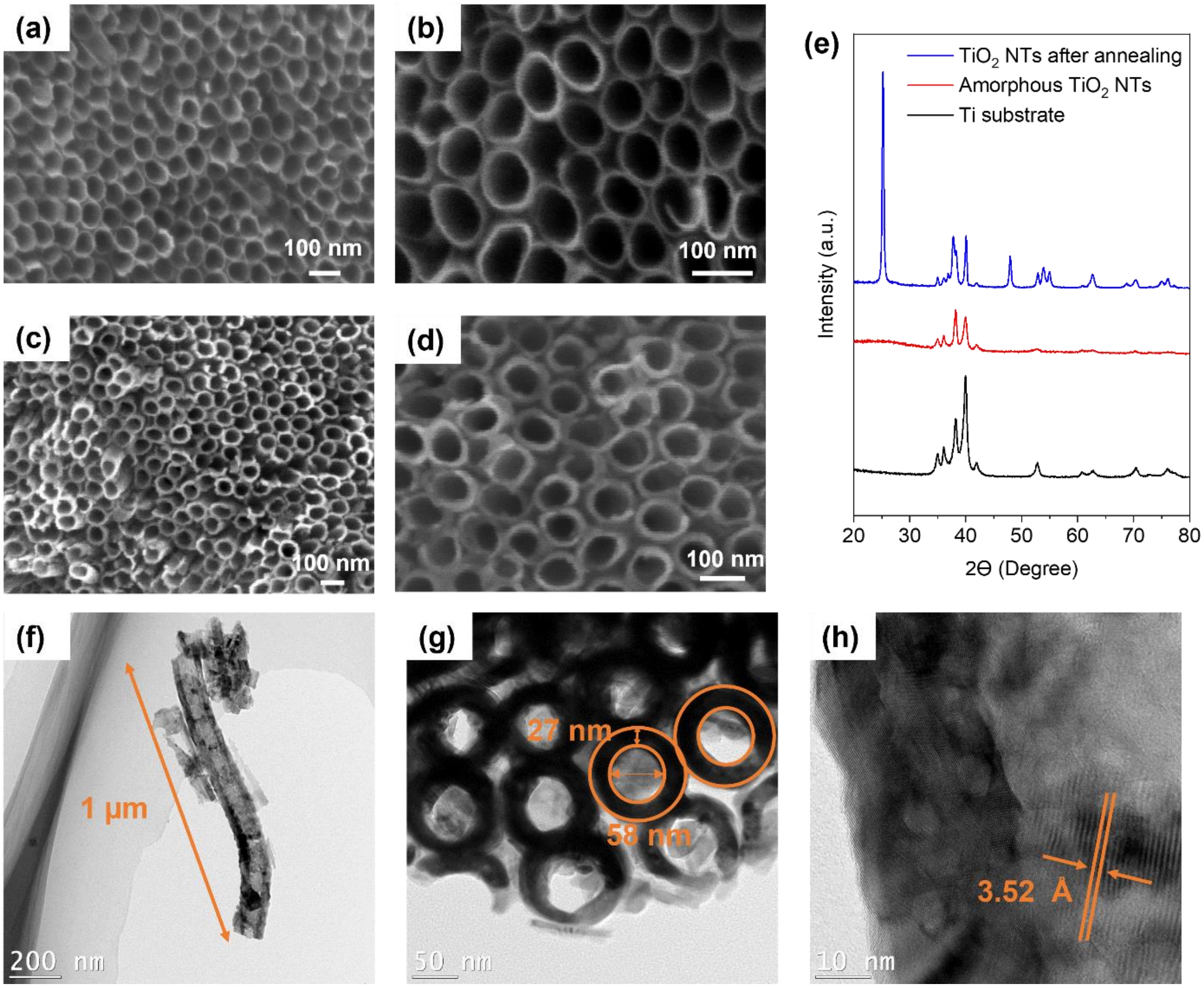

**Figure 5.2 Structural characterization of $TiO_2$ NTs: SEM images: (a) - (b) before annealing; (c) - (d) after annealing. (e) XRD pattern for Ti substrate, amorphous $TiO_2$ NTs, and crystalline $TiO_2$ NTs. TEM images: (f) single $TiO_2$ NTs; (g) Top view of the $TiO_2$ NTs array; (h) high-resolution TEM showing the atomic resolution and interplanar spacing.**

XPS was used to investigate the surface chemical composition of the $TiO_2$ NTs before and after annealing [Figure 5.3]. The survey scan spectra for the $TiO_2$ NTs sample before and after annealing are presented in Figure 5.3 (a) and (b), respectively. The presence of F 1s (684.3 and 687.9 eV) and N 1s (400 eV) peaks are related to the ammonium fluoride used in the electrolyte solution for the anodization process and the high-resolution peaks are shown in Figure 5.3 (g) and (h). The annealing process eliminates the presence of F 1s and N 1s peaks due to the oxidation of these elements as shown in Figure 5.3 (b). The Ti 2p high-resolution peaks are presented in Figure 5.3 (c) before annealing and 5.3 (d) after annealing. There is a small shift in the binding energies of the $Ti^{4+}$ $2p_{3/2}$ and $Ti^{4+}$ $2p_{1/2}$ peaks, which is related to the changes in chemical bonding due to the thermal oxidation from the annealing process [155]. Likewise, there is a slight shift in the oxygen O 1S content before [Figure 5.3 (e)] and after [Figure 5.3 (f)] annealing [156]. The spectra show that the concentration of $OH^{-1}$ (531.7 eV) has decreased as compared to $O^{-2}$ (529.9 eV) after the annealing in an oxygen atmosphere, while keeping the same peak position.

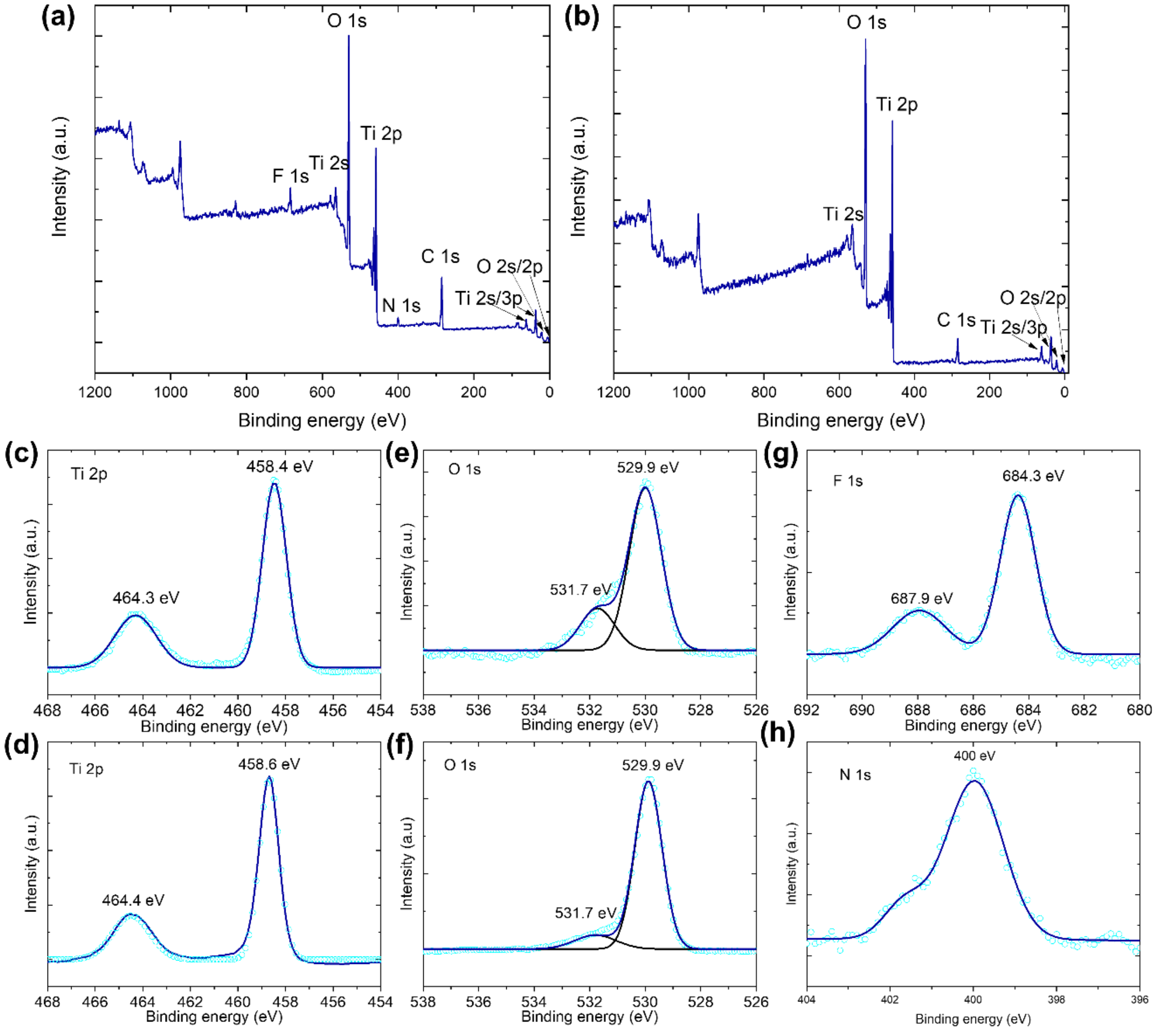

**Figure 5.3 XPS spectra acquired for the Ti NTs before and after annealing: survey scan (a) and (b), Ti 2p (c) and (d), and O 1s (e) and (f), respectively. F 1s (g) and N 1s (h) before annealing**

## 5.3 p-n heterojunction formation and characterization

The p-n heterojunction was created inside the crystalline $TiO_2$ NTs by depositing CdS/CdSe QDs (n-type semiconductor) and CuSe (p-type semiconductor) through the SILAR method. Briefly, after the three SILAR cycles of the CdSe, the $Se^{2-}$ was deposited on the photoanode, then immediately immersed in the Cu-based solution for 5, 10, 15, and 20 s. The CuSe layer was grown after the CdS/CdSe QDs sensitization and before the ZnS passivation layer. The role of the CdS/CdSe QDs to broaden the absorption range of the photoanode was confirmed by using UV-Vis as shown in Figure 5.4 (a). The results show that the QDs were able to capture the light in the visible region. This confirms the photoactivity of the QDs in the visible region. However, the deposition of CuSe, to form a p-n heterojunction with the QDs, has an insignificant effect on the absorption range. Figure 5.4 (b) and (c) show the SEM images for the $TiO_2$ NTs before and after sensitization with CdS/CdSe QDs. The $TiO_2$ NTs before sensitization show a smooth wall structure of the NTs, while after sensitization, the QDs were obviously deposited on the $TiO_2$ NTs walls, which leads to changing the surface texture into a rough one. The inset image shows the actual visual inspection of the samples. The inset images visually confirm the deposition of the CdS/CdSe QDs. The color of the $TiO_2$ NTs changes from light grey into dark red due to the sensitization process. Moreover, EDS was used to confirm the presence and distribution of the elements used for the QDs deposition with the CuSe coating layer. Figure 5.4 (d) presents the elemental analysis of the as designed photoanode. The cross-sectional image of the photoanode and the elemental mapping, which present the elemental distribution, are presented in Figures (e) to (l). From these images, all elements that contributed to the formation of the photoanode are homogenously distributed: Ti and O ($TiO_2$ NTs), Cd – S – Se – Zn (CdS/CdSe/ZnS QDs), and Cu (CuSe coating layer).

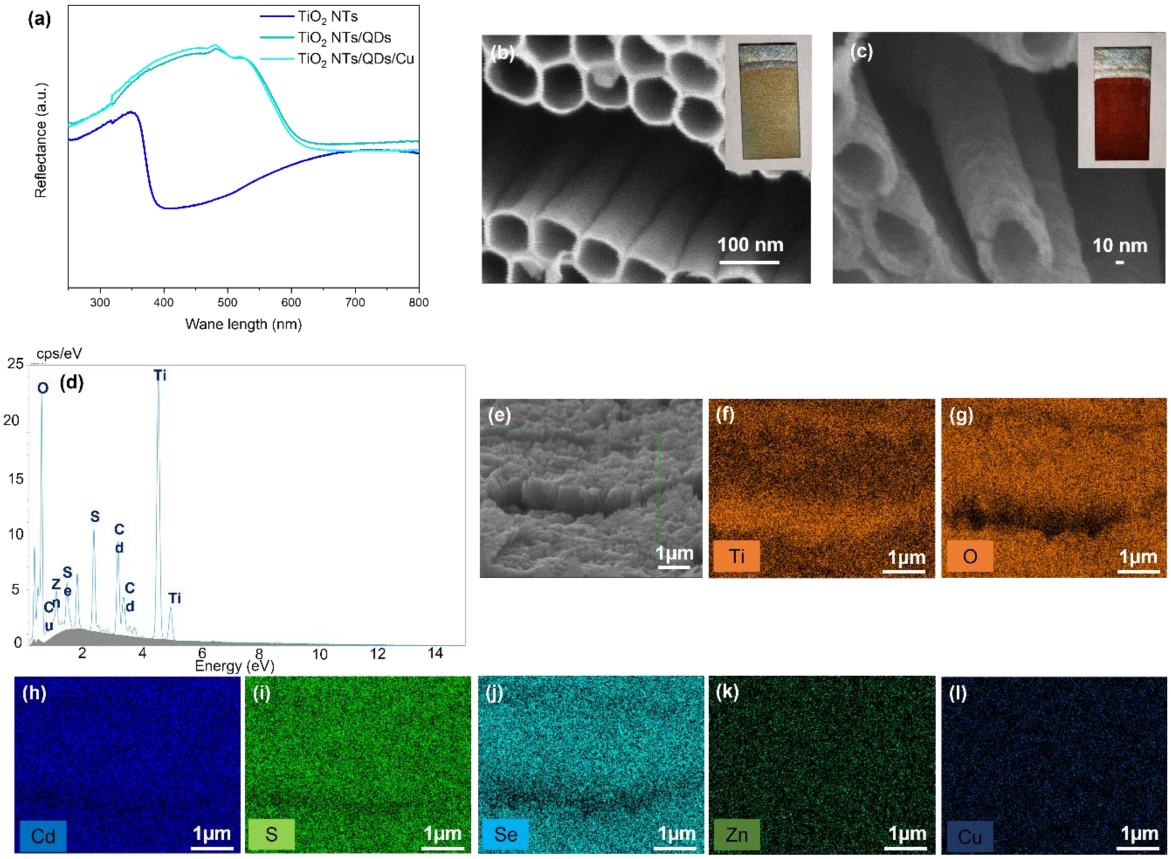

**Figure 5.4 (a) UV-Vis reflectance spectrum of $TiO_2$ NTs with QDs and CuSe deposition. SEM images of the $TiO_2$ NTs (b) before; (c) after QDs deposition. (d) EDS elemental map spectrum (e) EDS selected area for mapping; elemental distribution of (f) Ti; (g) O; (h) Cd; (i) S; (j) Se; (k) Zn; (l) Cu.**

XPS was used to analyze the surface composition and the bonding nature that occurs inside the $TiO_2$/CdS-CdSe/CuSe/ZnS photoanode. Figure 5.5 (a) shows the XPS survey spectrum, which confirms the presence of all elements that participated in the photoanode-designed structure (i.e., Ti, O, Cd, S, Se, Zn, and Cu). The high-resolution spectrum of Ti 2p [Figure 5.5 (b)] and O 1s [Figure 5.5 (c)] were matched before the sensitization. The Cd 3d deposition was confirmed with the Cd $3d_{3/2}$ and Cd $3d_{5/2}$ characterization peak at 405 and 411.7 eV, respectively [Figure 5.5 (d)]. The S 2p consists of one peak that can be fitted into two characterization peaks that represent S $2p_{3/2}$ and S $2p_{1/2}$ at 161.2 and 162.4 eV, respectively [Figure 5.5 (e)]. Likewise, the Se $3d_{5/2}$ peak was fitted into two characterization peaks at 53.8 and 54.4 eV [Figure 5.5 (f)]. The Zn 2p has two separate characterization peaks Zn $2p_{1/2}$ and $2p_{3/2}$ that are positioned at 1021.9 and 1045 eV, respectively [Figure 5.5 (g)]. Finally, the bonding nature of Cu 2p is important in understanding the final structure that exists in the formation of the p-n heterojunction. The peak position at 932.4 and 952.1 eV reflects the characterization peaks Cu $2p_{3/2}$ and $2p_{1/2}$, respectively. Those binding energies are associated with the oxidation state of Cu (I) [157, 158]. Accordingly, when Cu (I) is combined with the Se $3d_{5/2}$ binding energy of 53.8 eV, then the final structure is confirmed to CuSe [159, 160].

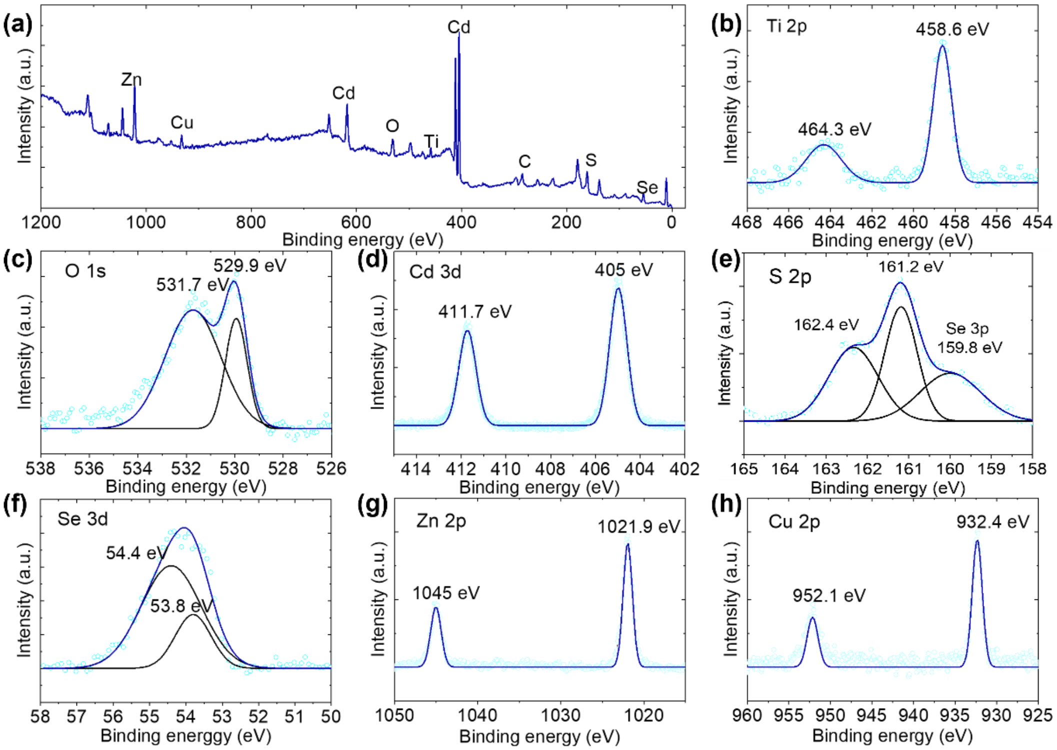

**Figure 5.5 XPS spectra acquired for $TiO_2$ NTs/CdS/CdSe/CuSe/ZnS photoanode: (a) full survey scan; (b) Ti 2p; (c) O 1s; (d) Cd 3d; (e) S 2p; (f) Se 3d; (g) Zn 2p; and (h) Cu 2p**

KPFM was used to investigate the p-n heterojunction formation effect on the surface potential of the photoanode. The difference in work function was measured for the photoanode with and without the CuSe coating layer in dark and light conditions. Figure 5.6 (a) shows the AFM topography images used for the reference sample (i.e., without CuSe) using tapping mode. Figure 5.6 (b) presents the contrast while varying the lighting condition to stimulate the dark and light effect on the surface potential of the different photoanodes. The same procedure was used for the photoanode with the CuSe coating layer in Figure 5.6 (c) and (d). The line scan results from the KPFM measurement are presented in Figure 5.6 (e) for the reference and CuSe samples. The difference in the surface potential measurement under light and dark conditions is ~35 mV for the reference sample, while ~52.7 mV for the CuSe based photoanode. The higher difference in surface potential confirms that the deposition of the CuSe coating layer enhances the surface potential under light condition. In turn, the charge separation and injection process are better in the case of the p-n heterojunction as compared to the reference sample. It is worth mentioning the surface potential in the KPFM measurement is not very stable due to the charging effect that occurs at the surface [161]. To stimulate the results, the band diagram of the n-type semiconductor and the formation effect of the p-n heterojunction is presented in Figure 5.6 (f). The splitting of the quasi-Fermi level is higher in the case of p-n heterojunction (with CuSe coating layer) as compared to the reference sample (with only QDs). This effect occurs due to the presence of two majority carriers: electrons from the QDs (n-type semiconductor) and holes from the CuSe (p-type semiconductor). Upon illumination, both carriers contribute to the splitting of the Fermi level, which results in higher photovoltage that can be represented as surface potential in the KPFM measurement [162]. Finally, a schematic diagram of the carrier dynamics of the designed structure of the photoanode is presented in Figure 5.6 (g). The proper engineering of the band alignment anticipates accelerating the charge injection and separation process inside the photoanode. In addition, the carrier dynamics at the photoanode/electrolyte interface is estimated to increase, due to the high surface potential, which can reflect a higher PEC device performance.

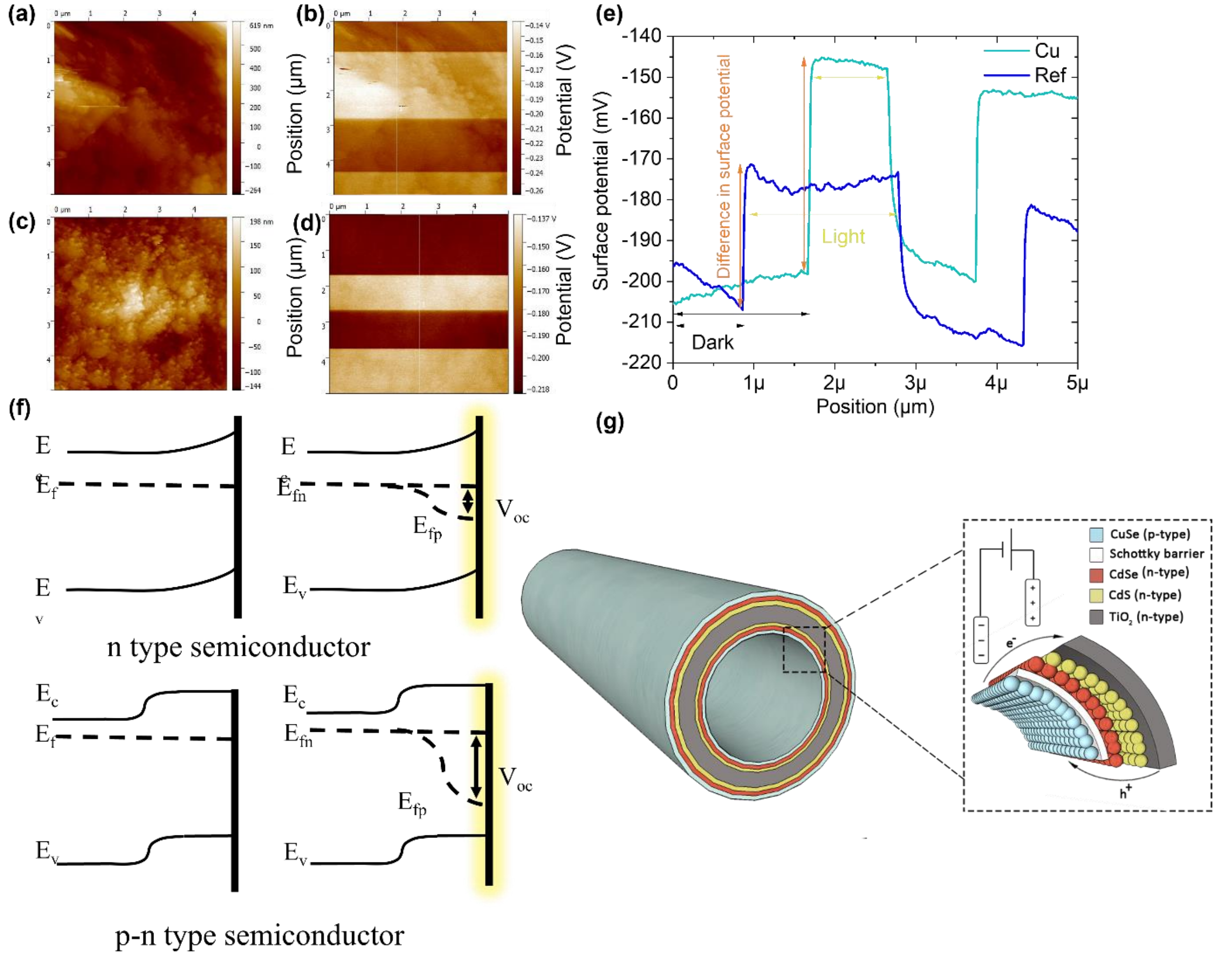

**Figure 5.6 AFM topography images under normal condition and chopped illumination: (a)-(b) $TiO_2$ NTs/QDs; (c)-(d) $TiO_2$ NTs/QDs/CuSe, respectively. (e) KPFM surface potential line scan. (f) Band diagram representation of the $TiO_2$ NTs/QDs (n-type) and $TiO_2$ NTs/QDs/CuSe (p-n type) under dark and light. (g) A schematic representation of the effect of the p-n heterojunction in PEC device carrier dynamics**

## 5.4 PEC performance

A series of photoanodes were fabricated to highlight the effect of each operational efficiency (i.e., LHE, charge transport efficiency, and interfacial charge transport efficiency) on the performance of the PEC devices. (1) The LHE was examined by comparing the $TiO_2$ NTs photoanode with and without the sensitization of CdS/CdSe QDs. (2) The charge transport efficiency was studied by changing the ETL morphology from $TiO_2$ NTs to NPs with the same thickness (~1 μm) and sensitized with the same QDs. (3) The interfacial charge transport efficiency was investigated by creating the p-n heterojunction with different CuSe deposition times. Finally, the influence of the $TiO_2$ NTs thickness (i.e., changing the thickness from 1 to 2 μm) was evaluated with respect to the PEC device performance.

The $TiO_2$ NPs film was prepared using the spin coating technique on the Ti foil substrate used to grow the $TiO_2$ NTs. The NPs film thickness was measured with SEM to make sure that it matches the thickness of the NTs. LSV experiment was used to measure the photocurrent density vs potential for different PEC devices. The measurements were carried out under dark, light, and chopped illumination (AM 1.5, 100 mW cm$^{-2}$). Figure 5.7 (a) present the photocurrent density vs potential under light condition for the devices based on $TiO_2$ NTs, $TiO_2$ NTs/QDs, and $TiO_2$ NPs/QDs. At 0.5 V vs RHE, the photocurrent density of the device based on $TiO_2$ NTs/QDs was 4.18 mA cm$^{-2}$, which is significantly higher as compared to the PEC devices based on $TiO_2$ NPs/QDs (0.45 mA cm$^{-2}$) and $TiO_2$ NTs (0.08 mA cm$^{-2}$). These results highlight two main contributors to the performance of the PEC devices: (1) the LHE, through increasing the photoactivity of the PEC device via increasing the light-harvesting range that reaches the visible region, and (2) the charge transport efficiency, with changing the morphology into 1D that provides a directional pathway and reducing the carrier recombination rate for the photogenerated carriers. The LSV measurement for the reference (i.e., $TiO_2$ NTs) and $TiO_2$ NTs/QDs PEC devices are presented in Figures 5.7 (b) and (c), respectively. The photovoltage of different PEC devices and the calculated electron lifetime can be estimated through the OCP measurement, as shown in Figure 5.7 (d). The measurement was carried out under light for 50 s then the light was off for 250 s. The difference in the measured potential under light and dark can reflect the amount of photovoltage each device can produce. The decay rate of the measured potential in the OCP represents the tendency of the photogenerated carriers to recombine either with the oxidized species in the electrolyte or the trap sites inside the photoanode itself. Faster decay corresponds to a higher recombination rate and vice-versa. In Figure 5.7 (d), the decay rate of the device based on $TiO_2$ NPs/QDs is significantly faster than the device based on $TiO_2$ NTs/QDs or $TiO_2$ NTs, which reflects that more recombination events occur on the device based on NPs as compared to NTs. In addition, the electron lifetime can also be calculated through the first derivative of the potential decay with respect to time. The results presented in Figure 5.7 (e) show that at any given potential the PEC device based on $TiO_2$ NTs/QDs has the highest electron lifetime as compared to other devices. These results conclude that the carrier recombination that occurs during the device operation in the case of NTs is considerably lower as compared to the NPs, which is determined by both the LSV and OCP measurements, as shown in Figure 5.7 (f). It is worth mentioning that the photovoltage of the device based on NPs/QDs is slightly higher than NTs/QDs. This occurs due to the availability of higher surface area in the case of NPs, which in turn deposit a higher amount of QDs and generate more charge carriers. In addition, the porosity of the NPs film is also higher, which increases the penetration depth of the electrolyte and its interaction with the photoanode surfaces.

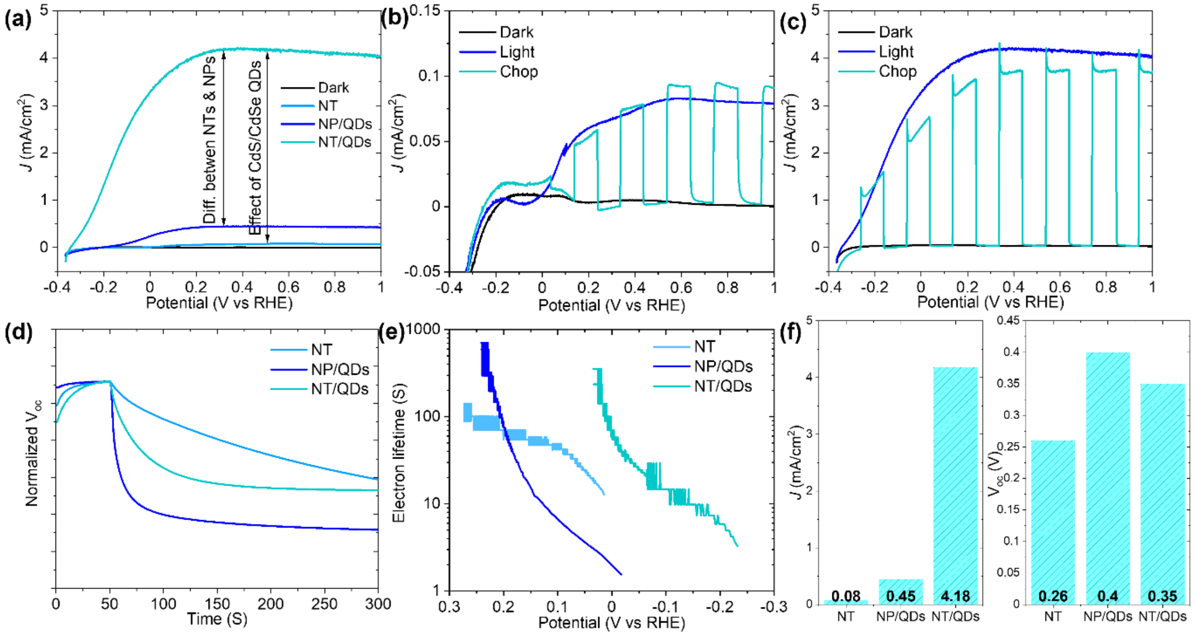

**Figure 5.7 (a) LSV measurement for the devices based on $TiO_2$ NTs, $TiO_2$ NPs/QDs, and $TiO_2$ NTs/QDs photoanodes under light conditions. PEC performance under dark, light, and chopped for (b) $TiO_2$ NTs and (c) $TiO_2$ NTs/QDs. (d) Normalize OCP measurement. (e) Electron lifetime calculation. (f) Saturated photocurrent density at 0.5V vs. RHE and photovoltage.**

The charge separation and injection process depend mainly on the surface potential, which directly affects the PEC device performance. Various growth of the CuSe layer was designed by immersing the photoanodes in the Cu $(NO_3)_2.3H_2O$ solution, after the third cycle of Se in the SILAR process, for different times (5, 10, 15, and 20 s). The created p-n heterojunction generates an electric field that enhances the surface potential, as determined by the KPFM results. The effect of varying the CuSe deposition duration on the photocurrent density, under light conditions, in the LSV measurement is presented in Figure 5.8 (c). The photocurrent density tends to enhance with increasing the immersion time from 0 to 15 s and then decrease with further immersion for 20 s. The photocurrent density vs potential for the reference device (i.e., without CuSe deposition) and the optimized device (i.e., with 15 s CuSe deposition), are presented in Figures 5.8 (a) and (b), respectively. There is an improvement of 13% in the photocurrent density based on the optimized device with 4.72 mA cm$^{-2}$ as compared to the reference device with 4.18 mA cm$^{-2}$ at 0.5 V vs RHE. The improvement in the photocurrent density is attributed to the enhancement in the surface potential and thus the injection and separation processes. However, a further increase In the immersion time reduces the photocurrent density due to higher recombination between the photogenerated electrons (from the QDs “n-type”) and photogenerated holes (from the CuSe “p-type”). The surface potential also influences the PEC device stability, as it affects the carrier dynamics at the photoanode/electrolyte interface. A chopped illumination for 300 s was conducted on the reference and optimized device at 0.4 V vs RHE, as shown in Figure 5.8 (d), to examine the device's stability. The optimized device maintains 95.94% of the initial photocurrent density, while the reference device maintains only 89.44%. The device stability is attributed to the rate of photocorrosion process that occurs to the QDs on the surface of the photoanode. The accumulation of holes at the interface and its slow transfer rate to the electrolyte affect the hole scavenger process and reduce the stability of the PEC devices. In turn, the optimized device with high surface potential enhances the carrier separation, which involves a higher rate of hole transfer to the electrolyte, and consequently prevents the accumulation of holes and the oxidation process that results in better PEC device stability. To confirm the results obtained in the chopped illumination stability test, long-term stability test was investigated under continuous light illumination for 2 h at 0.4 V vs RHE, as shown in Figure 5.8 (e). The results show that the long-term stability is aligned with the short chopped one with an improvement in device stability with the addition of the CuSe layer. The reference device maintains 62.5% of the initial photocurrent density, while the device based on 15 s CuSe maintains 66% after 2 h of continuous light illumination under one sun. The OCP decay measurement and the calculated electron lifetime are presented in Figure 5.8 (f). The results show that there is a higher decay in the case of 15 s CuSe as compared to the reference device, which indicates a lower electron lifetime as compared to the reference device. It is worth mentioning that these results are conducted in an open circuit condition. The p-n heterojunction enhances the charge separation and injection process in the normal operational condition (i.e., closed circuit). However, in an OCP measurement, the charges are generated and separated but not collected due to the open circuit condition. This led to the accumulation of photogenerated electrons and holes in the bulk of the photoanode. Once the light was turned off, the high number of photogenerated holes in the CuSe based device increase the recombination rate, and thus a faster decay of the measured potential is achieved as compared to the reference device.

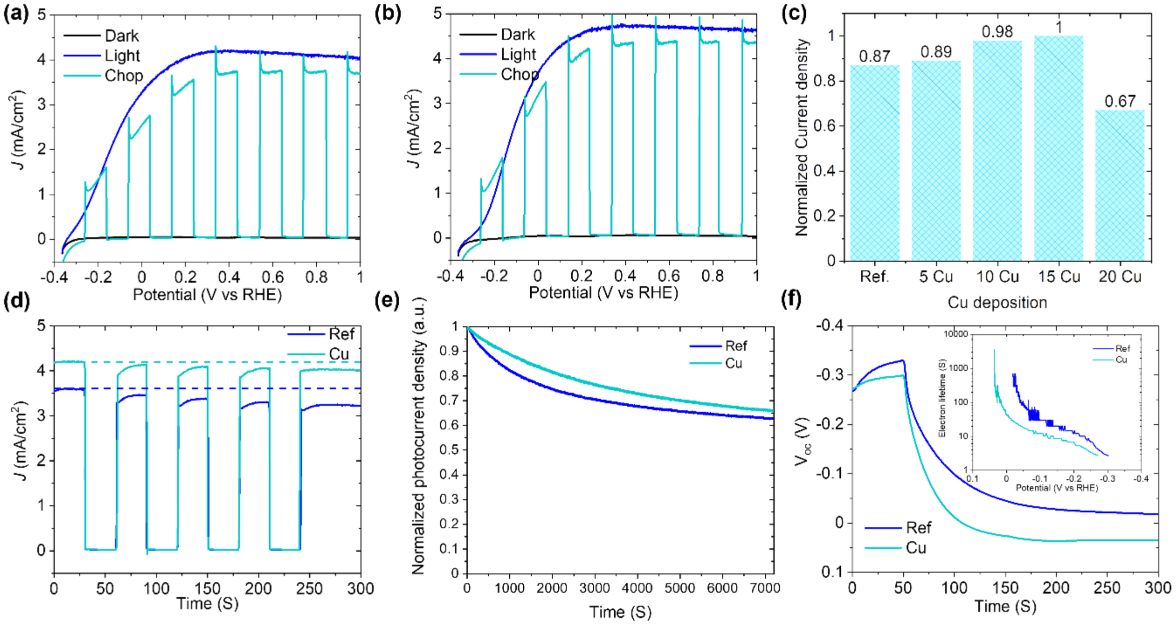

**Figure 5.8 PEC performance under dark, light, and chopped; (a) TiO2 NTs/QDs (reference); (b) TiO2 NTs/QDs/15 CuSe (optimized). (c) Normalized photocurrent density of photoanodes with x S CuSe deposition time. (d) Chopped illumination stability test. (e) long-term stability test (f) OCP decay measurement and inset Electron lifetime calculation.**

The $TiO_2$ NTs length variation was studied on the performance of the PEC devices based on $TiO_2$ NTs/QDs with and without the optimized CuSe coating layer. The photocurrent density for the PEC devices at 0.5 V vs RHE is presented in Figure 5.9 (a). The results show that the increase in length (i.e., from 1 to 2 μm) of the $TiO_2$ NTs reduces the photocurrent density for both devices as follows: $TiO_2$ NTs/QDs by 11% (from 4.18 to 3.72 mA cm$^{-2}$) and $TiO_2$ NTs/QDs/Cu with 14% (from 4.72 and 4.05 mA cm$^{-2}$). The LSV measurement for the long $TiO_2$ NTs/QDs with and without CuSe is shown in Figure 5.9 (b) and (c), respectively. The degradation in the photocurrent density is associated with longer $TiO_2$ NTs due to the increase in the distance for the photogenerated carriers to reach the conductive substrate. A longer pathway for the photogenerated electrons increases the probability of carrier recombination, which reduces the photocurrent density of the PEC devices. On the other hand, longer $TiO_2$ NTs improve the stability of the PEC devices, as shown in the results of Figure 5.9 (d). The stability test was conducted on the longer $TiO_2$ NTs, as presented in Figure 5.9 (e), with the same condition as applied for the shorter $TiO_2$ NTs in Figure 5.8 (d). The total thickness of the photoanode has a dual effect. As previously discussed, when the thickness increases the path length of the photogenerated carriers increases, which reduces the photocurrent density of the device due to the recombination events and trap sites. In contrast, the active surface area increases, which increases the amount of the QDs deposited inside the photoanode. The additional quantity of QDs accompanied by more electrolyte penetration inside the photoanode improves the carrier dynamics at the photoanode/electrolyte interface. This improvement in carrier dynamics positively impacts the hole scavenger process resulting in higher operational stability for both PEC devices. Figure 5.9 (f) presents the OCP decay measurement, and the inset image shows the electron lifetime calculations for the longer device based on $TiO_2$ NTs/QDs with and without CuSe. The results are consistent with the shorter $TiO_2$ NTs, although a lower effect of CuSe on the electron lifetime coexists. The lower impact on the electron lifetime is related to the proportional difference between the small number of photogenerated holes by CuSe as compared to a large number of photogenerated electrons by QDs in the longer device.

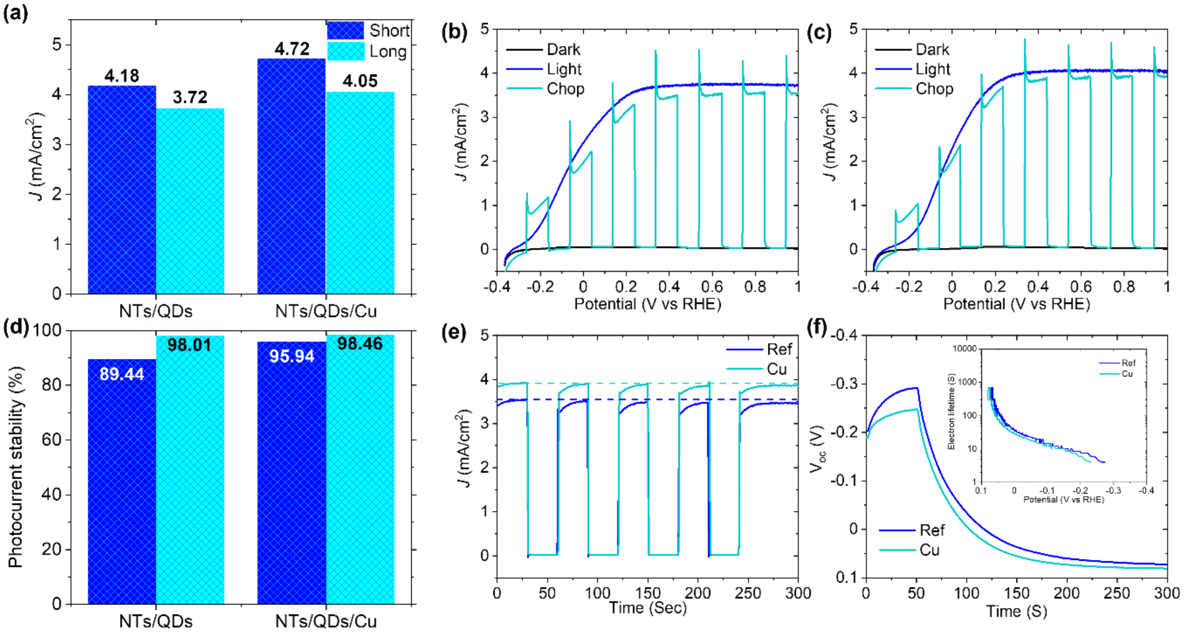

**Figure 5.9 (a) Photocurrent density comparison for short and long $TiO_2$ NTs. PEC performance under dark, light, and chopped for $TiO_2$ long NTs/QDs (b) with and (c) without Cu. (d) Photocurrent stability comparison between short and long $TiO_2$ NTs. (e) Stability test chopped illumination. (f) OCP decay measurement and the inset image is the electron lifetime calculation.**

## 5.5 Summary

In summary, this chapter provides simple low-cost solution-based fabrication processes that can be used to design photoanodes for PEC $H_2$ generation. Ti substrate was used to grow self-organized $TiO_2$ NTs that are used as a template for the sensitization of CdS/CdSe QDs via the SILAR method. In addition, the deployment of nanoscale p-n heterojunction at the surface of the photoanode was performed with a fast and simple approach. The process requires only dipping the photoanode in Cu-based solution for 15 s after the deposition of the CdS/CdSe QDs. The deposition of CuSe (p-type semiconductor) enhances the surface potential and the PEC device performance. The surface potential was investigated through KPFM measurements, under dark and light conditions, to confirm the improvement effect occurs due to the deposition of the CuSe layer. The employment of one-dimensional NTs and p-n heterojunction at the surface of the photoanode offer better carrier dynamics. Overall, this work provides a pathway to optimize the photoanode structure to further improve the solar-driven PEC performance and other emerging optoelectronic devices in a cost-effective way that can be easily scalable into the industrial sector.

# CHAPTER 6: CONCLUSION AND PERSPECTIVE

In this thesis, the photoelectrochemical (PEC) devices were fabricated, and the improvement of their performance were made through different strategies. The main goal of each strategy is either to enhance the generation and collection of the photogenerated carriers or to reduce the non-radiative carrier recombination during the device operation. The idea for each project was designed to improve one or more operational efficiencies (i.e., light harvesting efficiency (LHE), charge transport, and interfacial charge transfer efficiencies) simultaneously in a simple and cost-effective way. The conclusion for each of the presented works is as follows:

In chapter 3, the design and fabrication of a heterojunction photoanode based on $SnO_2$/ two-dimensional Functionalized hexagonal boron nitride (2D F-h-BN) nanoflakes were used in the PEC device for $H_2$ generation. The objective of this project is to passivate the $SnO_2$ surface with 2D F-h-BN nanoflakes and to reduce the non-radiative carrier recombination at the $SnO_2$/quantum dots (QDs) interface. The effect of the 2D nanoflakes was investigated on the PEC device performance and carrier dynamics. The results show that a PEC device based on $SnO_2$/F-h-BN/CdS QDs exhibits a 60% improvement in the saturated photocurrent density (at 1.0 V vs RHE) compared to the control device, due to improved electron injection and reduced non-radiative carrier recombination at the $SnO_2$/QDs/electrolyte interface. In addition, the stability of the device based on $SnO_2$/2D F-h-BN/CdS-CdSe QDs was enhanced by 13.5% as compared to the reference device without 2D F-h-BN, after 4 h of one sun continuous illumination (A.M. 1.5 100 mW $cm^{-2}$). Moreover, tailoring the $SnO_2$ film thickness and incorporating multiwall carbon nanotubes (MWCNTs) were explored to study their effect on carrier dynamics and further improve overall device performance. The results from the thickness variation express that the ideal performance was achieved with two mesoporous layers of $SnO_2$. However, the highest stability was achieved with three layers that maintain 98% of the initial value of photocurrent density after 4 h of continuous illumination. The highest saturated photocurrent density value reached 6.35 mA $cm^{-2}$ (at 1.0 V vs RHE), after thickness optimization of the $SnO_2$ film, by incorporation 0.015 wt. % of MWCNTs, and CdS/CdSe QDs deposition. The carrier dynamics and electron band structure were studied to underpin the reasons behind the PEC device improvement. The employment of 2D F-h-BN nanoflakes acts as an energy barrier at the photoanode/electrolyte interface, and results in fewer non-radiative carrier recombination events. Furthermore, it negatively shifts the conduction band (C.B.) of $SnO_2$ that improves the injection rate of the photogenerated carriers from the QDs to the electron transport layer (ETL). Finally, a comparison between the $SnO_2$ and $TiO_2$ on the photocurrent density and stability was made to reach the optimal ETL material that will continue in this thesis work. The results show that with $TiO_2$ a higher photocurrent density was obtained, while $SnO_2$ exhibited higher long-term stability of the PEC device.

In chapter 4, a novel surface engineered hybrid photoanode architecture was reported that combines one dimensional nanorods (1D NRs) and nanoparticles (NPs) to improve the charge transport properties and reduce the non-radiative carrier recombination. As proof of concept, a PEC device based on the optimized $TiO_2$ NRs/NPs hybrid structured photoanode sensitized with CdS QDs yields a saturated photocurrent density of 4.25 mA $cm^{-2}$ (at 0.8 V vs RHE), which is 172% higher than that of the reference device (with only NPs), due to the enhancement in charge transport efficiency and prolonged electron lifetime. The optimized $TiO_2$ NRs/NPs hybrid structured photoanode was then treated with hydrazine to engineer the surface traps to further enhance the performance of PEC devices. The hydrazine treated device yields an additional 17% increase in the saturated photocurrent density, reaching 5.43 mA $cm^{-2}$ with CdS QDs, and 8.12 mA $cm^{-2}$ with CdS/CdSe QDs (at 0.8 V vs RHE), while maintaining 79% of its initial photocurrent density value, after 2 h of continuous one sun illumination. The role of surface engineering via nitrogen doping is to suppress non-radiative carrier recombination inside $TiO_2$ by screening the trap sites in the electronic band structure. Density function theory (DFT+U) was used in the theoretical calculations to describe the mechanism that characterizes this significant improvement. The calculations verify that the surface engineering through hydrazine treatment creates band states far below the conduction band minimum (CBM) that act as a trap sites screener, which reduces the non-radiative carrier recombination probability of the photogenerated carriers and enhances the overall device performance. The work in this study reduces the undesirable non-radiative carrier recombination of PEC devices through morphological optimization and surface engineering of the hybrid $TiO_2$ photoanodes.

In chapter 5, an engineered photoanode that covers all three main factors to enhance the charge generation and collection of the PEC device was constructed. This engineered photoanode consists of self-organized $TiO_2$ nanotubes (NTs) arrays sensitized by CdS/CdSe QDs and treated with a Cu-based solution to create a p-n heterojunction. The PEC devices based on QDs sensitized $TiO_2$ NTs yield a photocurrent density of 4.18 mA.$cm^{-2}$ at 0.5 V vs RHE, which is 7 times higher than the device based on $TiO_2$/QDs NPs (i.e., 0.45 mA.cm-2). These results highlight the LHE effect of QDs sensitizations and carrier transport by employing the $TiO_2$ NTs instead of NPs. The CdS/CdSe QDs offer broader light-harvesting and $TiO_2$ NTs provide a directional pathway of the photogenerated carriers towards the backend of the photoanode, and eventually improve the PEC performance due to increasing the charge transfer efficiency and reduced carrier recombination. Afterward, for better carrier kinetics at the photoanode/electrolyte interface, a p-n heterojunction was formed by depositing a p-type CuSe coating over the $TiO_2$ NTs/QDs photoanodes. The p-n heterojunction improves the separation/injection rate of the photogenerated charge carrier. The resulting PEC device shows a 13 % improvement in the saturated photocurrent density, reaching 4.72 $mA.cm^{-2}$ at 0.5 V vs RHE. The enhancement in photogenerated carrier separation/injection via a p-n heterojunction was confirmed by conductive KPFM measurements. The results show that the photoanode with p-n heterojunction has a higher surface potential and better separation/injection of charge carriers than the control photoanode. In addition, we demonstrate that PEC devices with longer $TiO_2$ NTs offer better long-term stability as compared to the shorter NTs.

The work in this thesis offers simple yet cost-effective and efficient strategies to enhance the performance of QDs based PEC hydrogen generation and potentially other optoelectronic devices (i.e., solar cells and photodetectors). The study does not only present strategies to enhance the device performance, but also provides a detailed understanding of the carrier dynamics and recombination processes within the PEC devices. Ultimately, it opens a new pathway to implement several effective strategies simultaneously and offers a simple and scalable method for the design and optimization of the photoanodes to enhance the performance of solar-driven PEC devices.

# REFERENCES

1. Smil, V., *Energy: A Beginner's Guide*. 2017: Oneworld Publications.
2. Atkins, P., *The laws of thermodynamics: A very short introduction*. 2010: OUP Oxford.
3. Smil, V., *Fossil Fuels, Primary Electricity, and Renewables.* 2017.
4. Berner, R.A., *The long-term carbon cycle, fossil fuels and atmospheric composition.* Nature, 2003. **426**(6964): p. 323-326.
5. bp. *Statistical Review of the World Energy 70th edition*. 2021; Available from: https://www.bp.com/content/dam/bp/business-sites/en/global/corporate/pdfs/energy-economics/statistical-review/bp-stats-review-2021-full-report.pdf.
6. data, O.W.i. *Energy production and consumption*. 2021; Available from: https://ourworldindata.org/energy-production-consumption.
7. Smil, V., *Energy and Civilization: A History*. 2017: MIT Press.
8. Program, U.N.D. *Human Development Indices and Indicators*. 2018; Available from: http://hdr.undp.org/sites/default/files/2018_human_development_statistical_update.pdf.
9. development, C.f.g. *Electricity Consumption and Development Indicators*. 2016; Available from: https://www.cgdev.org/media/electricity-consumption-and-development-indicators.
10. IEA. *Data and statistics*. 2014; Available from: https://www.iea.org/data-and-statistics.
11. data, O.W. *Access to electricity*. 2019; Available from: https://ourworldindata.org/energy-access#access-to-electricity.
12. NASA. *New Night Lights Maps Open Up Possible Real-Time Applications*. 2017; Available from: https://www.nasa.gov/feature/goddard/2017/new-night-lights-maps-open-up-possible-real-time-applications.
13. Whiting, K., L.G. Carmona, and T. Sousa, *A review of the use of exergy to evaluate the sustainability of fossil fuels and non-fuel mineral depletion.* Renewable and Sustainable Energy Reviews, 2017. **76**: p. 202-211.
14. Höök, M. and X. Tang, *Depletion of fossil fuels and anthropogenic climate change—A review*. Energy policy, 2013. **52**: p. 797-809.
15. Edenhofer, O., *Climate change 2014: mitigation of climate change*. Vol. 3. 2015: Cambridge University Press.
16. Houghton, J., *Global warming.* Reports on progress in physics, 2005. **68**(6): p. 1343.
17. Casper, J.K., *Fossil fuels and pollution: the future of air quality*. 2010: Infobase Publishing.
18. Bereiter, B., et al., *Revision of the EPICA Dome C CO2 record from 800 to 600 kyr before present.* Geophysical Research Letters, 2015. **42**(2): p. 542-549.
19. Change, T.I.P.o.C.; Available from: https://www.ipcc.ch/.
20. Nations, U. *The Paris Agreement*. 2015; Available from: https://www.un.org/en/climatechange/paris-agreement.
21. NASA. *The relentless rise of carbon dioxide*. Available from: https://climate.nasa.gov/climate_resources/24/graphic-the-relentless-rise-of-carbon-dioxide/.
22. Dincer, I., *Renewable energy and sustainable development: a crucial review.* Renewable and sustainable energy reviews, 2000. **4**(2): p. 157-175.
23. Hellier, C., *Cataclysmic Variable Stars-how and why they vary*. 2001: Springer Science & Business Media.
24. Landscheidt, T., *Solar Activity: A Dominant Factor in Climatic Dynamics.* Energy & Environment, 1998. **9**(6): p. 683-720.

25. Kalogirou, S.A., *Solar energy engineering: processes and systems*. 2013: Academic Press.
26. Lewis, N.S. and D.G. Nocera, *Powering the planet: Chemical challenges in solar energy utilization.* Proceedings of the National Academy of Sciences, 2006. **103**(43): p. 15729-15735.
27. Dresselhaus, M. and I. Thomas, *Alternative energy technologies.* Nature, 2001. **414**(6861): p. 332-337.
28. Gielen, D., et al., *The role of renewable energy in the global energy transformation.* Energy Strategy Reviews, 2019. **24**: p. 38-50.
29. Tyagi, V., et al., *Progress in solar PV technology: Research and achievement.* Renewable and sustainable energy reviews, 2013. **20**: p. 443-461.
30. Timilsina, G.R., L. Kurdgelashvili, and P.A. Narbel, *Solar energy: Markets, economics and policies.* Renewable and sustainable energy reviews, 2012. **16**(1): p. 449-465.
31. Lewis, N.S., *Research opportunities to advance solar energy utilization.* Science, 2016. **351**(6271).
32. Montoya, J.H., et al., *Materials for solar fuels and chemicals.* Nature materials, 2017. **16**(1): p. 70-81.
33. Schlapbach, L. and A. Züttel, *Hydrogen-storage materials for mobile applications.* Materials for sustainable energy: a collection of peer-reviewed research and review articles from nature publishing group, 2011: p. 265-270.
34. Mohamad, N.A.R.C., F.M. Mota, and D.H. Kim, *Photocatalytic and Photoelectrochemical Overall Water Splitting.* Solar-to-Chemical Conversion: Photocatalytic and Photoelectrochemical Processes, 2021.
35. Saraswat, S.K., D.D. Rodene, and R.B. Gupta, *Recent advancements in semiconductor materials for photoelectrochemical water splitting for hydrogen production using visible light.* Renewable and Sustainable Energy Reviews, 2018. **89**: p. 228-248.
36. Kim, J.H., et al., *Toward practical solar hydrogen production–an artificial photosynthetic leaf-to-farm challenge.* Chemical Society Reviews, 2019. **48**(7): p. 1908-1971.
37. Walter, M.G., et al., *Solar water splitting cells.* Chemical reviews, 2010. **110**(11): p. 6446-6473.
38. Qi, J., W. Zhang, and R. Cao, *Solar-to-hydrogen energy conversion based on water splitting.* Advanced Energy Materials, 2018. **8**(5): p. 1701620.
39. Hisatomi, T., J. Kubota, and K. Domen, *Recent advances in semiconductors for photocatalytic and photoelectrochemical water splitting.* Chemical Society Reviews, 2014. **43**(22): p. 7520-7535.
40. Sivula, K., *Metal oxide photoelectrodes for solar fuel production, surface traps, and catalysis.* The Journal of Physical Chemistry Letters, 2013. **4**(10): p. 1624-1633.
41. Guijarro, N., M.S. Prévot, and K. Sivula, *Surface modification of semiconductor photoelectrodes.* Physical Chemistry Chemical Physics, 2015. **17**(24): p. 15655-15674.
42. Yang, W., et al., *Strategies for enhancing the photocurrent, photovoltage, and stability of photoelectrodes for photoelectrochemical water splitting.* Chemical Society Reviews, 2019. **48**(19): p. 4979-5015.
43. Grätzel, M., *Photoelectrochemical cells*, in *Materials For Sustainable Energy: A Collection of Peer-Reviewed Research and Review Articles from Nature Publishing Group*. 2011, World Scientific. p. 26-32.
44. Chen, Z., H.N. Dinh, and E. Miller, *Photoelectrochemical water splitting*. Vol. 344. 2013: Springer.

45. Fujishima, A. and K. Honda, *Electrochemical photolysis of water at a semiconductor electrode.* nature, 1972. **238**(5358): p. 37-38.
46. Tanaka, Y. and K. Matsuo, *Non-thermal effects of near-infrared irradiation on melanoma*, in *Breakthroughs in Melanoma Research*. 2011, Citeseer.
47. Green, M.A., *Third generation photovoltaics: solar cells for 2020 and beyond.* Physica E: Low-dimensional Systems and Nanostructures, 2002. **14**(1-2): p. 65-70.
48. Conibeer, G., *Third-generation photovoltaics.* Materials today, 2007. **10**(11): p. 42-50.
49. Shockley, W. and H.J. Queisser, *Detailed balance limit of efficiency of p-n junction solar cells.* Journal of applied physics, 1961. **32**(3): p. 510-519.
50. Jager, K., et al., *Solar Energy Fundamentals, Technology and Systems. Delf University of Technology*. 2014.
51. Bisquert, J., *The physics of solar cells: perovskites, organics, and photovoltaic fundamentals*. 2017: CRC press.
52. Habas, S.E., et al., *Low-cost inorganic solar cells: from ink to printed device.* Chemical reviews, 2010. **110**(11): p. 6571-6594.
53. Chopra, K., P. Paulson, and V. Dutta, *Thin-film solar cells: an overview.* Progress in Photovoltaics: Research and applications, 2004. **12**(2-3): p. 69-92.
54. Kuang, Y., et al., *Elongated nanostructures for radial junction solar cells.* Reports on Progress in Physics, 2013. **76**(10): p. 106502.
55. Umebayashi, T., et al., *Analysis of electronic structures of 3d transition metal-doped TiO2 based on band calculations.* Journal of Physics and Chemistry of Solids, 2002. **63**(10): p. 1909-1920.
56. Wilke, K. and H. Breuer, *The influence of transition metal doping on the physical and photocatalytic properties of titania.* Journal of Photochemistry and Photobiology A: Chemistry, 1999. **121**(1): p. 49-53.
57. Dashora, A., et al., *Formation of an intermediate band in the energy gap of TiO2 by Cu–N-codoping: First principles study and experimental evidence.* Solar energy materials and solar cells, 2014. **125**: p. 120-126.
58. Wang, Y., et al., *First-principles study on transition metal-doped anatase TiO 2.* Nanoscale research letters, 2014. **9**(1): p. 1-8.
59. Torres, G.R., et al., *Photoelectrochemical study of nitrogen-doped titanium dioxide for water oxidation.* The Journal of Physical Chemistry B, 2004. **108**(19): p. 5995-6003.
60. Semonin, O.E., et al., *Peak external photocurrent quantum efficiency exceeding 100% via MEG in a quantum dot solar cell.* Science, 2011. **334**(6062): p. 1530-1533.
61. Tisdale, W.A., et al., *Hot-electron transfer from semiconductor nanocrystals.* Science, 2010. **328**(5985): p. 1543-1547.
62. Zhao, H. and F. Rosei, *Colloidal quantum dots for solar technologies.* Chem, 2017. **3**(2): p. 229-258.
63. O'Regan, B. and M. Grätzel, *A low-cost, high-efficiency solar cell based on dye-sensitized colloidal TiO2 films.* Nature, 1991. **353**(6346): p. 737-740.
64. Jin, L., et al., *Quantum Dots-Based Photoelectrochemical Hydrogen Evolution from Water Splitting.* Advanced Energy Materials, 2021. **11**(12): p. 2003233.
65. Jin, L., et al., *Near-infrared colloidal quantum dots for efficient and durable photoelectrochemical solar-driven hydrogen production.* Advanced Science, 2016. **3**(3): p. 1500345.

66. Selopal, G.S., et al., *Core/shell quantum dots solar cells.* Advanced Functional Materials, 2020. **30**(13): p. 1908762.
67. Tong, X., et al., *Near-Infrared, Heavy Metal-Free Colloidal "Giant" Core/Shell Quantum Dots.* Advanced Energy Materials, 2018. **8**(2): p. 1701432.
68. Klimov, V.I., et al., *Quantization of multiparticle Auger rates in semiconductor quantum dots.* Science, 2000. **287**(5455): p. 1011-1013.
69. Xia, C., et al., *Size-dependent band-gap and molar absorption coefficients of colloidal CuInS2 quantum dots.* ACS nano, 2018. **12**(8): p. 8350-8361.
70. Becker, M.A., et al., *How does a SILAR CdSe film grow? Tuning the deposition steps to suppress interfacial charge recombination in solar cells.* The journal of physical chemistry letters, 2014. **5**(9): p. 1575-1582.
71. Li, W. and X. Zhong, *Capping ligand-induced self-assembly for quantum dot sensitized solar cells.* The journal of physical chemistry letters, 2015. **6**(5): p. 796-806.
72. Watson, D.F., *Linker-assisted assembly and interfacial electron-transfer reactivity of quantum dot− substrate architectures.* The Journal of Physical Chemistry Letters, 2010. **1**(15): p. 2299-2309.
73. Pan, Z., et al., *Quantum dot-sensitized solar cells.* Chemical Society Reviews, 2018. **47**(20): p. 7659-7702.
74. Ning, W., et al., *Long Electron–Hole Diffusion Length in High-Quality Lead-Free Double Perovskite Films.* Advanced Materials, 2018. **30**(20): p. 1706246.
75. Chuang, C.-H.M., et al., *Improved performance and stability in quantum dot solar cells through band alignment engineering.* Nature materials, 2014. **13**(8): p. 796-801.
76. Ye, M., et al., *Recent advances in quantum dot-sensitized solar cells: insights into photoanodes, sensitizers, electrolytes and counter electrodes.* Sustainable Energy & Fuels, 2017. **1**(6): p. 1217-1231.
77. Xu, J., et al., *Surface engineering of ZnO nanostructures for semiconductor-sensitized solar cells.* Advanced Materials, 2014. **26**(31): p. 5337-5367.
78. Tian, J. and G. Cao, *Control of nanostructures and interfaces of metal oxide semiconductors for quantum-dots-sensitized solar cells.* The journal of physical chemistry letters, 2015. **6**(10): p. 1859-1869.
79. Liu, Z., et al., *PEC electrode of ZnO nanorods sensitized by CdS with different size and its photoelectric properties.* International journal of hydrogen energy, 2013. **38**(25): p. 10226-10234.
80. Wolcott, A., et al., *Photoelectrochemical water splitting using dense and aligned TiO2 nanorod arrays.* Small, 2009. **5**(1): p. 104-111.
81. Yalavarthi, R., et al., *Radiative and non-radiative recombination pathways in mixed-phase TiO2 nanotubes for PEC water-splitting.* Catalysts, 2019. **9**(2): p. 204.
82. Roza, L., et al., *Direct growth of oriented ZnO nanotubes by self-selective etching at lower temperature for photo-electrochemical (PEC) solar cell application.* Journal of alloys and compounds, 2015. **618**: p. 153-158.
83. Yang, X., et al., *Nitrogen-doped ZnO nanowire arrays for photoelectrochemical water splitting.* Nano letters, 2009. **9**(6): p. 2331-2336.
84. Pu, Y.-C., et al., *Surface passivation of TiO2 nanowires using a facile precursor-treatment approach for photoelectrochemical water oxidation.* The Journal of Physical Chemistry C, 2014. **118**(27): p. 15086-15094.

85. Seol, M., et al., *Novel nanowire array based highly efficient quantum dot sensitized solar cell.* Chemical Communications, 2010. **46**(30): p. 5521-5523.
86. Feng, H.-L., et al., *Three-dimensional hyperbranched TiO 2/ZnO heterostructured arrays for efficient quantum dot-sensitized solar cells.* Journal of Materials Chemistry A, 2015. **3**(28): p. 14826-14832.
87. Mohammadnezhad, M., et al., *Towards long-term thermal stability of dye-sensitized solar cells using multiwalled carbon nanotubes.* ChemPlusChem, 2018. **83**(7): p. 682-690.
88. Basu, K., et al., *Hybrid graphene/metal oxide anodes for efficient and stable dye sensitized solar cell.* Electrochimica Acta, 2020. **349**: p. 136409.
89. Akilimali, R., et al., *Graphene nanoribbon-TiO2-quantum dots hybrid photoanode to boost the performance of photoelectrochemical for hydrogen generation.* Catalysis Today, 2020. **340**: p. 161-169.
90. Layek, A., B. Manna, and A. Chowdhury, *Carrier recombination dynamics through defect states of ZnO nanocrystals: From nanoparticles to nanorods.* Chemical Physics Letters, 2012. **539**: p. 133-138.
91. Lu, L., et al., *Mn-doped TiO2 thin films with significantly improved optical and electrical properties.* Journal of Physics D: Applied Physics, 2012. **45**(48): p. 485102.
92. Shinde, V., et al., *Mn doped and undoped ZnO films: A comparative structural, optical and electrical properties study.* Materials Chemistry and Physics, 2006. **96**(2-3): p. 326-330.
93. Tamirat, A.G., et al., *Using hematite for photoelectrochemical water splitting: a review of current progress and challenges.* Nanoscale Horizons, 2016. **1**(4): p. 243-267.
94. Kim, J.H. and J.S. Lee, *Solar Water Splitting: Elaborately Modified BiVO4 Photoanodes for Solar Water Splitting (Adv. Mater. 20/2019).* Advanced Materials, 2019. **31**(20): p. 1970146.
95. Zhang, J.Z., *Metal oxide nanomaterials for solar hydrogen generation from photoelectrochemical water splitting.* MRS bulletin, 2011. **36**(1): p. 48-55.
96. Lokman, M.Q., et al., *Enhancing photocurrent performance based on photoanode thickness and surface plasmon resonance using Ag-TiO2 Nanocomposites in dye-sensitized solar cells.* Materials, 2019. **12**(13): p. 2111.
97. Kaneko, H., T. Minegishi, and K. Domen, *Recent progress in the surface modification of photoelectrodes toward efficient and stable overall water splitting.* Chemistry–A European Journal, 2018. **24**(22): p. 5697-5706.
98. Cao, J., et al., *Efficient, hysteresis-free, and stable perovskite solar cells with ZnO as electron-transport layer: effect of surface passivation.* Advanced Materials, 2018. **30**(11): p. 1705596.
99. Lakshmi, J., et al., *Effect of calcination atmosphere on photoluminescence properties of nanocrystalline ZrO2 thin films prepared by sol–gel dip coating method.* Physica B: Condensed Matter, 2011. **406**(15-16): p. 3050-3055.
100. Richards, B., J. Cotter, and C. Honsberg, *Enhancing the surface passivation of TiO 2 coated silicon wafers.* Applied physics letters, 2002. **80**(7): p. 1123-1125.
101. Garud, S., et al., *Surface passivation of CIGS solar cells using gallium oxide.* physica status solidi (a), 2018. **215**(7): p. 1700826.
102. Brennan, T.P., et al., *TiO2 conduction band modulation with In2O3 recombination barrier layers in solid-state dye-sensitized solar cells.* The Journal of Physical Chemistry C, 2013. **117**(46): p. 24138-24149.

103. O'Regan, B.C., et al., *Influence of the TiCl4 treatment on nanocrystalline TiO2 films in dye-sensitized solar cells. 2. Charge density, band edge shifts, and quantification of recombination losses at short circuit.* The Journal of Physical Chemistry C, 2007. **111**(37): p. 14001-14010.
104. Gao, J., et al., *Ultrathin Al2O3 passivation layer-wrapped Ag@ TiO2 nanorods by atomic layer deposition for enhanced photoelectrochemical performance.* Applied Surface Science, 2020. **499**: p. 143971.
105. Dean, C.R., et al., *Boron nitride substrates for high-quality graphene electronics.* Nature nanotechnology, 2010. **5**(10): p. 722-726.
106. Zhang, K., et al., *Two dimensional hexagonal boron nitride (2D-hBN): synthesis, properties and applications.* Journal of Materials Chemistry C, 2017. **5**(46): p. 11992-12022.
107. Shanmugam, M., et al., *2D layered insulator hexagonal boron nitride enabled surface passivation in dye sensitized solar cells.* Nanoscale, 2013. **5**(22): p. 11275-11282.
108. Britnell, L., et al., *Electron tunneling through ultrathin boron nitride crystalline barriers.* Nano letters, 2012. **12**(3): p. 1707-1710.
109. Cao, S., et al., *Band alignment engineering for improved performance and stability of ZnFe2O4 modified CdS/ZnO nanostructured photoanode for PEC water splitting.* Nano Energy, 2016. **24**: p. 25-31.
110. Ikram, A., et al., *Improved charge transportation at PbS QDs/TiO 2 interface for efficient PEC hydrogen generation.* Physical Chemistry Chemical Physics, 2016. **18**(23): p. 15815-15821.
111. Fu, Y., et al., *Phase-Modulated Band Alignment in CdS Nanorod/SnSx Nanosheet Hierarchical Heterojunctions toward Efficient Water Splitting.* Advanced Functional Materials, 2018. **28**(16): p. 1706785.
112. Yoon, J.-S., J.-W. Lee, and Y.-M. Sung, *Enhanced photoelectrochemical properties of Z-scheme ZnO/pn Cu2O PV-PEC cells.* Journal of Alloys and Compounds, 2019. **771**: p. 869-876.
113. Bae, D., et al., *Strategies for stable water splitting via protected photoelectrodes.* Chemical Society Reviews, 2017. **46**(7): p. 1933-1954.
114. Fujii, K., T. Karasawa, and K. Ohkawa, *Hydrogen gas generation by splitting aqueous water using n-type GaN photoelectrode with anodic oxidation.* Japanese journal of applied physics, 2005. **44**(4L): p. L543.
115. Ondersma, J.W. and T.W. Hamann, *Measurements and modeling of recombination from nanoparticle TiO2 electrodes.* Journal of the American Chemical Society, 2011. **133**(21): p. 8264-8271.
116. Mora-Sero, I., et al., *Recombination in quantum dot sensitized solar cells.* Accounts of chemical research, 2009. **42**(11): p. 1848-1857.
117. Selopal, G.S., et al., *Effect of blocking layer to boost photoconversion efficiency in ZnO dye-sensitized solar cells.* ACS Applied Materials & Interfaces, 2014. **6**(14): p. 11236-11244.
118. Kalyanasundaram, K., *Dye-sensitized solar cells*. 2010: CRC press.
119. Basu, K., et al., *Highly stable photoelectrochemical cells for hydrogen production using a SnO 2–TiO 2/quantum dot heterostructured photoanode.* Nanoscale, 2018. **10**(32): p. 15273-15284.

120. Cao, C., et al., *UV sensor based on TiO2 nanorod arrays on FTO thin film.* Sensors and Actuators B: Chemical, 2011. **156**(1): p. 114-119.

121. Chen, C., et al., *Electrochemically reduced graphene oxide on well-aligned titanium dioxide nanotube arrays for betavoltaic enhancement.* ACS applied materials & interfaces, 2016. **8**(37): p. 24638-24644.

122. Griffin, A., et al., *Spectroscopic size and thickness metrics for liquid-exfoliated h-BN.* Chemistry of Materials, 2018. **30**(6): p. 1998-2005.

123. Pan, S., et al., *Engineering the intermediate band states in amorphous Ti 3+-doped TiO 2 for hybrid dye-sensitized solar cell applications.* Journal of Materials Chemistry A, 2015. **3**(21): p. 11437-11443.

124. Klein, A., et al., *Transparent conducting oxides for photovoltaics: Manipulation of fermi level, work function and energy band alignment.* Materials, 2010. **3**(11): p. 4892-4914.

125. Hoshikawa, T., et al., *Impedance analysis for dye-sensitized solar cells with a three-electrode system.* Journal of Electroanalytical Chemistry, 2005. **577**(2): p. 339-348.

126. Choi, M., et al., *Hydrogen-doped brookite TiO2 nanobullets array as a novel photoanode for efficient solar water splitting.* Scientific reports, 2016. **6**(1): p. 1-12.

127. Wielant, J., et al., *Electronic properties of thermally formed thin iron oxide films.* Electrochimica Acta, 2007. **52**(27): p. 7617-7625.

128. Shi, L., et al., *Phase-junction design of MOF-derived TiO2 photoanodes sensitized with quantum dots for efficient hydrogen generation.* Applied Catalysis B: Environmental, 2020. **263**: p. 118317.

129. Tian, H., et al., *Enhanced photovoltaic performance of dye-sensitized solar cells using a highly crystallized mesoporous TiO 2 electrode modified by boron doping.* Journal of Materials Chemistry, 2011. **21**(3): p. 863-868.

130. Sivula, K., F. Le Formal, and M. Grätzel, *Solar water splitting: progress using hematite (α-Fe2O3) photoelectrodes.* ChemSusChem, 2011. **4**(4): p. 432-449.

131. Concina, I., Z.H. Ibupoto, and A. Vomiero, *Semiconducting metal oxide nanostructures for water splitting and photovoltaics.* Advanced Energy Materials, 2017. **7**(23): p. 1700706.

132. Jarzebski, Z. and J. Marton, *Physical properties of SnO2 materials: II. Electrical properties.* Journal of the electrochemical Society, 1976. **123**(9): p. 299C.

133. Hyun, B.-R., et al., *Electron injection from colloidal PbS quantum dots into titanium dioxide nanoparticles.* ACS nano, 2008. **2**(11): p. 2206-2212.

134. Kim, H. and S. Shim, *Temperature-controlled fabrication of SnO2 nanoparticles via thermal heating of Sn powders.* Applied Physics A, 2007. **88**(4): p. 769-773.

135. Reddy, K.M., S.V. Manorama, and A.R. Reddy, *Bandgap studies on anatase titanium dioxide nanoparticles.* Materials Chemistry and Physics, 2003. **78**(1): p. 239-245.

136. Yuan, S., et al., *Synthesis of hexagonal boron nitride graphene-like few layers.* Nanoscale, 2014. **6**(14): p. 7838-7841.

137. Su, S., et al. *Ultra-thin electro-spun PAN nanofiber membrane for high-efficient inhalable PM2. 5 particles filtration*. in *Journal of Nano Research*. 2017. Trans Tech Publ.

138. Kaur, J., et al., *Raman spectra, photoluminescence and ferromagnetism of pure, Co and Fe doped SnO2 nanoparticles.* Ceramics international, 2012. **38**(7): p. 5563-5570.

139. Xi, L., et al., *High surface area SnO2 nanoparticles: Synthesis and gas sensing properties.* Materials Chemistry and Physics, 2008. **108**(2-3): p. 232-236.

140. Matović, B., et al., *Synthesis and characterization of nanocrystaline hexagonal boron nitride powders: XRD and luminescence properties.* Ceramics International, 2016. **42**(15): p. 16655-16658.
141. Lu, F., et al., *Room temperature ionic liquid assisted well-dispersed core-shell tin nanoparticles through cathodic corrosion.* RSC advances, 2013. **3**(41): p. 18791-18793.
142. Lei, W., et al., *Boron carbon nitride nanostructures from salt melts: tunable water-soluble phosphors.* Journal of the American Chemical Society, 2011. **133**(18): p. 7121-7127.
143. Ci, L., et al., *Atomic layers of hybridized boron nitride and graphene domains.* Nature materials, 2010. **9**(5): p. 430-435.
144. Orellana, W. and H. Chacham, *Stability of native defects in hexagonal and cubic boron nitride.* Physical Review B, 2001. **63**(12): p. 125205.
145. Oladeji, I., et al., *Comparative study of CdS thin films deposited by single, continuous, and multiple dip chemical processes.* Thin Solid Films, 2000. **359**(2): p. 154-159.
146. Li, Y., et al., *Hydrothermal growth of well-aligned TiO2 nanorod arrays: Dependence of morphology upon hydrothermal reaction conditions.* Rare metals, 2010. **29**(3): p. 286-291.
147. Lopez-Luke, T., et al., *Nitrogen-doped and CdSe quantum-dot-sensitized nanocrystalline TiO2 films for solar energy conversion applications.* The Journal of Physical Chemistry C, 2008. **112**(4): p. 1282-1292.
148. Asahi, R., et al., *Visible-light photocatalysis in nitrogen-doped titanium oxides.* science, 2001. **293**(5528): p. 269-271.
149. Aba-Guevara, C.G., et al., *Comparison of two synthesis methods on the preparation of Fe, N-Co-doped TiO2 materials for degradation of pharmaceutical compounds under visible light.* Ceramics International, 2017. **43**(6): p. 5068-5079.
150. Pugazhenthiran, N., S. Murugesan, and S. Anandan, *High surface area Ag-TiO2 nanotubes for solar/visible-light photocatalytic degradation of ceftiofur sodium.* Journal of hazardous materials, 2013. **263**: p. 541-549.
151. Wehrenfennig, C., et al., *Fast charge-carrier trapping in TiO2 nanotubes.* The Journal of Physical Chemistry C, 2015. **119**(17): p. 9159-9168.
152. Roy, P., S. Berger, and P. Schmuki, *TiO2 nanotubes: synthesis and applications.* Angewandte Chemie International Edition, 2011. **50**(13): p. 2904-2939.
153. Regonini, D., et al., *Comparison of photoelectrochemical properties of TiO2 Nanotubes and sol-gel.* Electrochimica Acta, 2016. **213**: p. 31-36.
154. Rambabu, Y., M. Jaiswal, and S.C. Roy, *Probing the charge recombination in rGO decorated mixed phase (anatase-rutile) TiO2 multi-leg nanotubes.* AIP Advances, 2016. **6**(11): p. 115010.
155. Hannula, M., et al., *Improved stability of atomic layer deposited amorphous TiO2 photoelectrode coatings by thermally induced oxygen defects.* Chemistry of Materials, 2018. **30**(4): p. 1199-1208.
156. Greczynski, G. and L. Hultman, *X-ray photoelectron spectroscopy: towards reliable binding energy referencing.* Progress in Materials Science, 2020. **107**: p. 100591.
157. Selopal, G.S., et al., *Hierarchical self-assembled Cu2S nanostructures: fast and reproducible spray deposition of effective counter electrodes for high efficiency quantum dot solar cells.* Nano Energy, 2014. **6**: p. 200-210.
158. Zhao, C., et al., *Real-time monitoring of laser powder bed fusion process using high-speed X-ray imaging and diffraction.* Scientific reports, 2017. **7**(1): p. 1-11.

159. Zhang, S.-Y., et al., *Synthesis and characterization of hexagonal CuSe nanotubes by templating against trigonal Se nanotubes.* Crystal growth & design, 2006. **6**(12): p. 2809-2813.
160. Tong, Y., et al., *Selenium, Benzeneselenol, and Selenophene Interaction with Cu (100).* The Journal of Physical Chemistry C, 2016. **120**(38): p. 21486-21495.
161. Opitz, A., et al., *Spatiotemporal structure of intracranial electric fields induced by transcranial electric stimulation in humans and nonhuman primates.* Scientific reports, 2016. **6**(1): p. 1-11.
162. Yoo, H., et al., *Spatial charge separation in asymmetric structure of Au nanoparticle on TiO2 nanotube by light-induced surface potential imaging.* Nano letters, 2014. **14**(8): p. 4413-4417.